

國立臺灣大學理學院天文物理所

碩士論文

Graduate Institute of Astrophysics

College of Science

National Taiwan University

Master Thesis



原恆星 L1157-mm 和 L1448C 的次毫米波觀測

Observation of Class 0 Protostars: L1157-mm and L1448C

吳文正

Wen-Cheng Wu

指導教授：賀曾樸 博士

平野尚美 博士

Advisor: Paul Ho, Ph.D.

Naomi Hirano, Ph.D.

中華民國 102 年 1 月

January, 2013



Observation of Class 0 Protostars: L1157-mm and L1448C

Wu, Wen-Cheng

August 22, 2012



Acknowledgment

I would like to thank Dr. Naomi Hirano who kindly supervises me and let me realize what a good astronomer and scientist are. During the research, Dr. Naomi Hirano always leads me to the right way when I lost. Thanks a lot for training, and thanks so much for discussing and spending a lot of time reviewing my thesis. I would like to thank Dr. Paul Ho who kindly answered me to be my supervisor in NTU, and gave me important advices not only about my research but also about the attitude. I also want to thank Dr. Sheng-Yuan Liu, Dr. Chin-Fei Lee, Dr. Shigehisa Takakuwa, Prof. Wei-Hsin Sun and Prof. Jiun-Huei Protty Wu, who also help me a lot from life to study. Also, I would like to thank Sheng-Feng Yen for helping me to learn how to operate the telescope.

Thanks my friends in ASIAA for helping me, Chun-Hui Yang, Hsi-Wei Yen, Yen-Yu Lai, Liang-Yao Wang, Shi-Shin Chang, Po-Sheng Huang, Fei-Fan Chen, I-Non Chiu, Chih-Chiang Hsieh, Pei-Ying Hsieh, Chun-Fan Liu, Ai-Lai Sun and Mayzi Lin. I would also like to thanks my dear friend in ESOE, Yi-SO, Yu-Chieh, Yu-Yang, Bin, Tien-Chu, Chu-Hsuan Chen, Yu-Chun Wang. Also, thanks Chu-Hsuan Wen for encouraging me all the time. Finally, thanks my parents for supporting me, no matter what I want to do. Without all of you, I would not go that far.

Thank you very much!

Si nullos amicos habes, habes vitam tyranni; si invenies amicum verum, vita tua erit beata.

-Cicero-

摘要



我們利用次毫米波陣列 (SMA) 觀測兩個低質量第零類原恆星: L1157-mm 和 L1448C 的分子譜線及塵埃連續輻射訊號。觀測的角解析度約為 $3'' \sim 5''$ ，相當於 $650 \sim 1500 \text{ AU}$ 。 ^{12}CO (2-1)、 ^{13}CO (2-1)、 C^{18}O (2-1)、CS (7-6) 和 H_2CO ($5_{1,5}-4_{1,4}$) 是在兩個原恆星都偵測到的分子譜線。低速的 ^{12}CO (2-1) 譜線顯示靠近原恆星處的噴流瓣呈 V 型，其張角約為 $30^\circ \sim 40^\circ$ 。低速噴流的型態和運動學特徵可以用大張角原恆星風的模型解釋 (Wide Opening-Angle Wind)。除了 V 型噴流瓣，較準直且極高速的噴流現象 (EHV) 也在 L1448C 原恆星處發現，另外 SiO (8-7) 和 SO (5_6-4_5) 兩個譜線也偵測到極高速噴流。SiO 和 SO 的出現顯示在柱狀噴流中有震波 (Shock) 的存在，也代表此處是噴流內部交互作用發生的介面。而 L1157 的噴流中， ^{12}CO 譜線在南邊噴流瓣的東側和北邊噴流瓣的西側強度(Intensity)較強。這代表了 L1157 最近的質量噴發是沿著西北-東南的方向。這個近期質量噴發現象的位置角可以用噴發軸的進動模型 (Precession model) 來解釋 (進動角度 15°)。

C^{18}O (2-1)、CS (7-6) 和 H_2CO ($5_{1,5}-4_{1,4}$) 譜線較為緻密且圍繞在原恆星附近。在 L1157 和 L1448C 周圍的緻密氣體雲受到噴流的影響相當大。L1448C 的這三個譜線都有延著噴流方向的延展結構，其速度梯度趨勢也與 ^{12}CO 相同。L1157 的 C^{18}O 譜線也有相同於噴流的速度梯度，然而 CS 和 H_2CO 譜線則出現相反的速度梯度。L1157 周圍緻密氣體雲特殊的速度結構可解釋為靠近原恆星的氣體雲有一大張角的空腔 (cavity)。我們的結果也支持了噴流會對原恆星週遭物理環境產生極大的影響。另外，兩個原恆星的 C^{18}O 譜線也有延著垂直於噴流方向的速度梯度，代表原恆星週遭氣體雲可能也在旋轉。

關鍵字: 恆星形成 - Class 0 原恆星 - L1157-mm - L1448C - 分子譜線 - 無線電干涉儀



Abstract

We present molecular lines and continuum images of two low-mass class 0 protostars, L1157mm and L1448C obtained by the Submillimeter Array (SMA). The angular resolution was $3'' \sim 5''$, which corresponds to $650 \sim 1500$ AU. The $^{12}\text{CO}(2-1)$, $^{13}\text{CO}(2-1)$, $\text{C}^{18}\text{O}(2-1)$, CS (7-6) and H_2CO ($5_{1,5}-4_{1,4}$) lines were detected in both sources. The ^{12}CO emission with low velocity ($\delta V \leq \pm 6$ km s $^{-1}$ in L1157, and $\leq \pm 20$ km s $^{-1}$ in L1448C) show that the outflow lobes near the protostars have a V-shaped structure with an opening angle of $30^\circ \sim 40^\circ$. The morphologies and kinematics of the low velocity shells are reproduced by the model of wide-opening angle wind. In addition to the V-shaped lobes, a narrow jet with extremely high velocity (EHV) was observed in the L1448C outflow. The EHV jet in the L1448C outflow was also traced by the SiO (8-7) and SO (5_6-4_5) lines. The appearance of this EHV jet in SiO and SO suggests that there are shocks in the jet beam, representing the internal working surfaces. In the L1157 outflow, the ^{12}CO intensity is significantly enhanced in the eastern wall of the southern lobe and the western wall of the northern lobe. This suggests that the recent mass ejection of the L1157 outflow is in the NW-SE direction. The position angle of this recent ejection event can be explained by the precession model with a precession angle of 15° .

The $\text{C}^{18}\text{O}(2-1)$, CS (7-6) and H_2CO ($5_{1,5}-4_{1,4}$) emission show compact structures around the central stars. These dense gas envelopes around L1157-mm and L1448C are strongly affected by the outflow. In L1448C, these lines show elongated structures along the outflow axis, and velocity gradients with the same sense of ^{12}CO outflow. In L1157, the C^{18}O shows the same velocity gradient as the outflow, while the CS and H_2CO exhibit the opposite velocity gradient. The kinematic structure of the L1157 envelope is explained if the envelope had cavities with wide opening angles at their bases. Our results support the idea that the outflows play key roles in changing the physical condition of circumstellar envelopes. On the other hand, the C^{18}O shows a velocity gradient that is perpendicular to the outflow axis in both

sources, suggesting that the envelopes around the protostars are rotating. The estimated specific angular momenta are $2.17 \times 10^{-4} \text{ km s}^{-1} \text{ pc}$ and $5.5 \times 10^{-3} \text{ km s}^{-1} \text{ pc}$ for L1157 and L1448C, respectively.

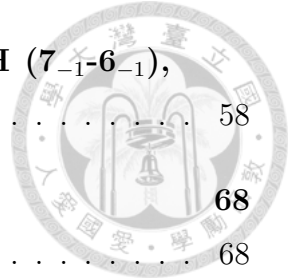
Keywords – stars: formation - stars: circumstellar matters - ISM: individual objects (L1157-mm) - ISM: individual objects (L1448C) - ISM: jets and outflow - ISM: molecules - submillimeter - radio continuum



Contents

| | |
|--|-----------|
| Acknowledgment | i |
| Abstract (Chinese) | ii |
| Abstract | iii |
| List of figures | vi |
| List of Tables | ix |
| 1 Introduction | 1 |
| 1.1 Evolutionary Stages of YSOs: A scenario of protostellar evolution | 2 |
| 1.2 Sources | 6 |
| 1.2.1 L1157-mm | 6 |
| 1.2.2 L1448C | 7 |
| 2 Observations and Data Reduction | 9 |
| 3 Results | 16 |
| 3.1 L1157 | 16 |
| 3.1.1 230 GHz and 345 GHz Continuum emissions | 16 |
| 3.1.2 ^{12}CO (2-1) Molecular Line | 23 |
| 3.1.3 ^{13}CO (2-1) Molecular Line | 27 |
| 3.1.4 Physical parameters of ^{12}CO (2-1) emission | 29 |
| 3.1.5 C^{18}O (2-1), C^{17}O (3-2) and H^{13}CO^+ (4-3) Molecular Line | 31 |
| 3.1.6 CS (7-6) and H_2CO ($5_{1,5} - 4_{1,4}$) Molecular Lines | 35 |
| 3.2 L1448C | 37 |
| 3.2.1 230 GHz and 345 GHz Continuum emissions | 37 |
| 3.2.2 Outflow: ^{12}CO (2-1), SO (5_6-4_5), SiO (8-7) | 43 |

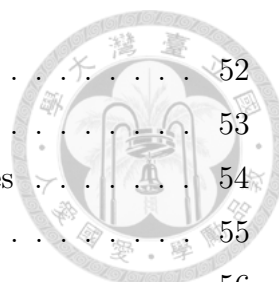
| | | |
|----------|--|-----------|
| 3.2.3 | Envelope: ^{13}CO (2-1), C^{18}O (2-1), CH_3OH (7 ₋₁ -6 ₋₁), CS (7-6), H_2CO (5 _{1,5} - 4 _{1,4}) | 58 |
| 4 | Discussion | 68 |
| 4.1 | Outflow | 68 |
| 4.1.1 | Low Velocity ^{12}CO Outflow Shells in L1157 and L1448C | 68 |
| 4.1.2 | High Velocity Components in L1157 and L1448C | 71 |
| 4.2 | Envelope | 75 |
| 4.2.1 | Kinematics | 75 |
| 4.2.2 | Specific Angular Momentum in L1157 and L1448C . . . | 80 |
| 4.2.3 | Origin of Absorption Dips in the C^{18}O , CS and H_2CO lines in L1448C | 82 |
| 5 | Summary | 84 |
| | Bibliography | 86 |





List of Figures

| | | |
|------|--|----|
| 1.1 | Schematic diagram of the evolutionary sequence | 5 |
| 1.2 | IRAC grey-scale image of L1157 overlaid with the CO 2-1 emission | 7 |
| 1.3 | IRAC image of L1448 and CO map of the L1448 outflow | 8 |
| 3.1 | 1.3 mm and 0.85 mm continuum map of L1157 | 18 |
| 3.2 | Visibility amplitude versus uv distance plot | 19 |
| 3.3 | Spectral energy distributions of L1157 | 21 |
| 3.4 | Total integrated intensity map of ^{12}CO (2-1) | 24 |
| 3.5 | P-V diagram of the ^{12}CO (2-1) emission along the outflow axis in L1157 | 25 |
| 3.6 | moment 0 map (contours) of the HV(from -4 to -12(blue); 8 to 16(red) km s $^{-1}$) component of ^{12}CO emission | 26 |
| 3.7 | The moment 0 of ^{13}CO (2-1) emission | 27 |
| 3.8 | Moment 0 maps of ^{13}CO (2-1) at three different velocity ranges | 28 |
| 3.9 | Moment 0 maps of C^{18}O , C^{17}O and H^{13}CO^+ lines | 32 |
| 3.10 | Moment 1 map of the C^{18}O (2-1) | 33 |
| 3.11 | P-V diagram of the C^{18}O (2-1) emission along the minor axis(PA=65 $^\circ$) in L1157 | 34 |
| 3.12 | Moment 0 maps of CS and H_2CO lines | 35 |
| 3.13 | P-V diagram of the CS (7-6) emission along the outflow axis | 36 |
| 3.14 | 1.3 mm and 0.85 mm continuum map of L1448C | 39 |
| 3.15 | Visibility amplitude versus uv distance plot for the 0.85 mm continuum emission | 40 |
| 3.16 | Spectral energy distributions of L1448C | 42 |
| 3.17 | Scheme of velocity ranges of ^{12}CO (2-1), SiO (8-7) and SO (5_6-4_5) emission | 43 |
| 3.18 | The spectra of the ^{12}CO (2-1), SiO (7-8) and SO (5_6-4_5) line emissions | 46 |
| 3.19 | moment 0 maps of ^{12}CO (2-1)(contours) | 47 |
| 3.20 | P-V diagram of the ^{12}CO (2-1) emission along the jet axes | 48 |



| | | |
|------|--|----|
| 3.21 | Moment 0 map of SiO (8-7) | 52 |
| 3.22 | Moment 0 maps of SiO (8-7) | 53 |
| 3.23 | P-V diagram of the SiO (8-7) emission along the jet axes | 54 |
| 3.24 | moment 0 maps of SO (5 ₆ -4 ₅) | 55 |
| 3.25 | moment 0 maps of SO (5 ₆ -4 ₅) | 56 |
| 3.26 | P-V diagram of the SO (5 ₆ -4 ₅) emission along the jet axes | 57 |
| 3.27 | moment 0 map of C ¹⁸ O (2-1) and moment 0 map of C ¹⁸ O (2-1)(contours) overlaid with ¹² CO contour | 61 |
| 3.28 | The moment 1 map of the C ¹⁸ O (2-1) emission and P-V diagram of the C ¹⁸ O (2-1) emission along the outflow axis | 62 |
| 3.29 | Moment 0 map of C ¹⁸ O (2-1) contours | 63 |
| 3.30 | Moment 0 maps of ¹³ CO (2-1)(contours) emission | 64 |
| 3.31 | moment 0 map of CS (7-6)(contours) and P-V diagram of the CS (7-6) emission along the outflow axis | 65 |
| 3.32 | Moment 0 map of H ₂ CO (5 _{1,5} – 4 _{1,4} contours and P-V diagram of the H ₂ CO (5 _{1,5} – 4 _{1,4} emission along the outflow axis | 66 |
| 3.33 | The moment 0 map of CH ₃ OH (7 ₋₁ -6 ₋₁) | 67 |
| 4.1 | moment 0 maps(Figure 3.5 & Figure 3.21(d) of each sources overlaid with black (L1157) and brown (L1448C) curves | 69 |
| 4.2 | PV-diagram of L1157 (left) and L1448C (right) along the outflow axes overlaid with the model | 70 |
| 4.3 | The moment 0 map of ¹² CO emission in L1157 overlaid with jet pre- cessing models | 72 |
| 4.4 | Schematic diagram of the different outflow structure in L1448C (a) and L1157 (b) | 74 |
| 4.5 | Schematic diagrams | 76 |
| 4.6 | PV-diagram of N ₂ H ⁺ 1-0 along the axis of 75° and PV-diagram of the C ¹⁸ O 2-1 along the axis of 65° | 78 |
| 4.7 | P-V diagrams of the C ¹⁸ O, CS and H ₂ CO emission along the outflow axis | 79 |
| 4.8 | Diagram of specific angular momentum versus rotation radius | 81 |
| 4.9 | P-V diagrams of the C ¹⁸ O, CS and H ₂ CO emission along the outflow axis | 83 |
| 4.10 | Schematic diagrams of two possible envelope structures | 83 |



List of Tables

| | | |
|-----|--|----|
| 2.1 | Source Information | 11 |
| 2.2 | Spectral Setup: 230 GHz | 11 |
| 2.3 | Spectral Setup: 337 GHz | 12 |
| 2.4 | Spectral Setup: 342 GHz | 12 |
| 2.5 | Observation Log | 13 |
| 2.6 | Calibrators | 13 |
| 2.7 | Observational Parameters of L1157 | 14 |
| 2.8 | Observational parameters of L1448 | 15 |
| 3.1 | 2D Gaussian fit result | 17 |
| 3.2 | Photometric Data of L1157 | 20 |
| 3.3 | 2D Gaussian fit result | 38 |
| 3.4 | Photometric Data of L1448C | 41 |
| 3.5 | Parameters of the ^{12}CO line emission | 50 |
| 3.6 | Time scales of the SiO and SO line emission | 51 |

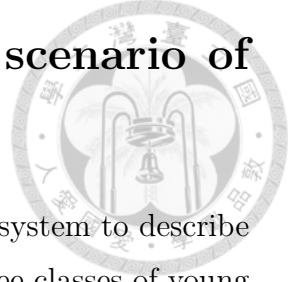


Chapter 1

Introduction

It is believed that low mass stars form from molecular cloud cores by gravitationally contraction. This formation process involves a series of stages (Lada 1987, Shu et al. 1987, André et al. 2000). Initially, the molecular cloud cores are supported against gravity by a combination of thermal, magnetic and turbulent pressures (Mouschovias 1991, Shu et al. 1987). Then, the condensation inside these cores become unstable, and start to collapse. The gravitational energy is freely radiated away, and staying at an isothermal condition during this initial phase of collapse. The isothermal approximation begin to break down when the infalling dust and gas becomes optically thick and heats up, and reaches to a quasi-equilibrium state (e.g., Kürschner 1994) and forming a hydrostatic equilibrium object at its center. As this first core gains mass and increases in temperature, molecular hydrogen dissociates and creates an energy sink, thus starts a second collapse phase, leading to the formation of the second protostellar core (Boss & Yorke, 1995). After these central protostellar objects have formed, surrounding materials begin to accreted onto the central object. During this main accretion phase, the temperature is getting higher and higher, the accreted mass is also increasing. Finally, when the central object has accumulated most ($\geq 90\%$) of its final, main-sequence mass, it becomes a pre-main-sequence star, a T Tauri star with a disk. As time goes by, this circumstellar disk will gradually clears out and forms planets or stellar companions.

1.1 Evolutionary Stages of YSOs: A scenario of protostellar evolution



From observational point of view, Lada (1987) presented a class system to describe the evolutionary stages of the protostellar sources. There are three classes of young stellar objects (YSOs) could be classified based on their spectra energy distributions (SEDs) in the near- to mid-infrared band observation. Depending on the value of the infrared spectral index, $\alpha_{IR} = -d \log(\nu F_\nu)/d \log \nu$. Evaluated from 2.2 μm to 10-25 μm .

- **Class I:** $\alpha_{IR} > 0$ (Wilking et al. 1989), with broader SEDs than single black body functions. They are found to be associated with dense molecular gas (Myers et al. 1987), and likely to be embedded in their parent molecular cloud cores.
- **Class II:** $-1.5 > \alpha_{IR} > 0$, SEDs are still broader than single temperature black body curves. They correspond to classical T Tauri stars, lacking circumstellar envelope and are optically visible. They are surrounded by optically thick circumstellar disk.
- **Class III:** $\alpha_{IR} < -1.5$, SEDs are similar to single black body curves, and do not exhibit large infrared excess. Like Class II, they lack circumstellar envelope, but with an optically thin disk and correspond to weak line T Tauri stars.

Apart from these three categories, André et al. (1993) suggested another new class of YSOs, **Class 0**, which are with stronger submillimeter dust emission (The class system is summarized in Figure 1.1). They are defined with following observational features from SEDs (André et al. 1993 and 2000, Chen et al. 1995 and 1997):

- weak emission at $\lambda < 10 \mu\text{m}$.
- a spectral energy distribution similar to a black body at 15-30 K.
- high ratio of submillimeter to bolometric luminosity, $L_{sub}/L_{bol} > 0.5\%$, where L_{sub} is the luminosity measured at $\lambda > 350 \mu\text{m}$., suggesting that the envelope mass exceeds the central stellar mass.

Another parameter called bolometric temperature T_{bol} (Myers & Ladd, 1993), the temperature of a black body having the same mean frequency as the observed SED, is introduced in an attempt to describe the evolution of YSOs and main-sequence stars in a unified way (Myers et al. 1998). T_{bol} increases monotonically from Class 0 to Class III, where Class 0 sources have T_{bol} is less than 70 K, 70 ~ 650 K for Class I, 650 ~ 2880 K for Class II, and larger than 2880 K for Class III.

Circumstellar Disk

The Class 0 protostars are the youngest protostars (typically $1 \sim 3 \times 10^4$ yr), and at the beginning of the main accretion phase (André, Ward-Thompson, & Barsony, 1993). In this stage, central protostellar object gradually builds up its mass (M_*) from a surrounding infalling envelope of mass M_{env} , and then forming an accretion disk (Looney et al. 1999). According to the model proposed by Terebey et al. (1984), disks should be already present at the class 0 stage. Although, circumstellar disks have been detected widely at class I stage, the presence of disks at the class 0 stage is not yet clear on the observation (Chandler et al. 2005, Jørgensen et al. 2007). Most of the class 0 sources observed with submm/mm interferometers show compact components on the longest baselines, which may suggest a presence of circumstellar disks. However, to distinguish emission comes from between inner envelope or rotationally-supported disk is one of the problems. The recent PROSAC project (Jørgensen et al. 2007) surveys 20 embedded class 0/I protostars in a wide range of submillimeter lines and continuum, providing new studies of the inner regions of protostellar envelope.

Molecular Outflow

In addition to the accretion, observations also have shown a powerful mass ejection along the poles which is accompanied by the main accretion phase. This mass-loss phenomena from young stars called bipolar jets or outflows (Snell et al. 1980). Almost all young stellar objects undergo periods of mass loss, and these outflows are believed to carry away not only material but excess angular momentum of the infalling matter (Konigl & Pudritz 2000). The interaction with the surrounding molecular material of this phenomena are detected in high-velocity CO emission (Snell et al. 1980, Rodríguez et al. 1980). The fast well-collimated stellar wind sweeps up the ambient molecular gas in its vicinity, forming two cavities oriented in opposite directions with respect to the protostar. These molecular gas then expands

in the form of lobes and shells and thus constitutes the CO outflow.

Many models have been proposed to explain the morphology and kinematics of molecular outflow. The jet-driven bow shock model (Raga & Cabrit 1993, Masson & Chernin 1993) and the wind-driven-shell model (Shu et al. 1991, Li & Shu 1996, Shu et al. 2000) are the standard of the field. In the jet-driven model, a jet propagates into the ambient material and forms a bow shock surface at the head of the jet. The shock then interacts with the ambient material and produces the molecular outflow around the jet. In the wind-driven model, a wide-angle magnetized wind is blowing into the ambient material, and creating a forward shock running ahead of the wind bubble, and then sweeping up the ambient material and producing the molecular outflow. However, none of these two models are suitable for explanation of all types of outflows simultaneously. Santiago-García et al. (2009) presented observation with high angular resolution, showing class 0 molecular outflow such as HH211, L1448 and IRAS 04166+2706 with two outflow components simultaneously: at low velocity, outflow appears as a limb-brightened shell, while at high velocity, the outflow becomes more jet-like. Recently, a "unified model" was proposed by Shang et al. (2006), presenting a possible explanation of these jet+shell system. The highly collimated jet is described as an on-axis density enhancement of the X-wind type of wide-opening angle wind, and the jet corresponds to the densest part of the primary wind, the shell instead is mostly consisted of the swept-up ambient material. On the other hand, detection of multiple cavities in some CO molecular outflows presents further challenges for any suitable steady state models (e.g., L1157 in Gueth, Guilloteau, & Bachiller 1996).

In this thesis, we present the observations of two class 0 young stellar objects, L1157-mm and L1448C. Using the continuum and molecular line data observed with the Submillimeter Array (SMA), we discuss the protostellar envelopes and outflows of these sources.

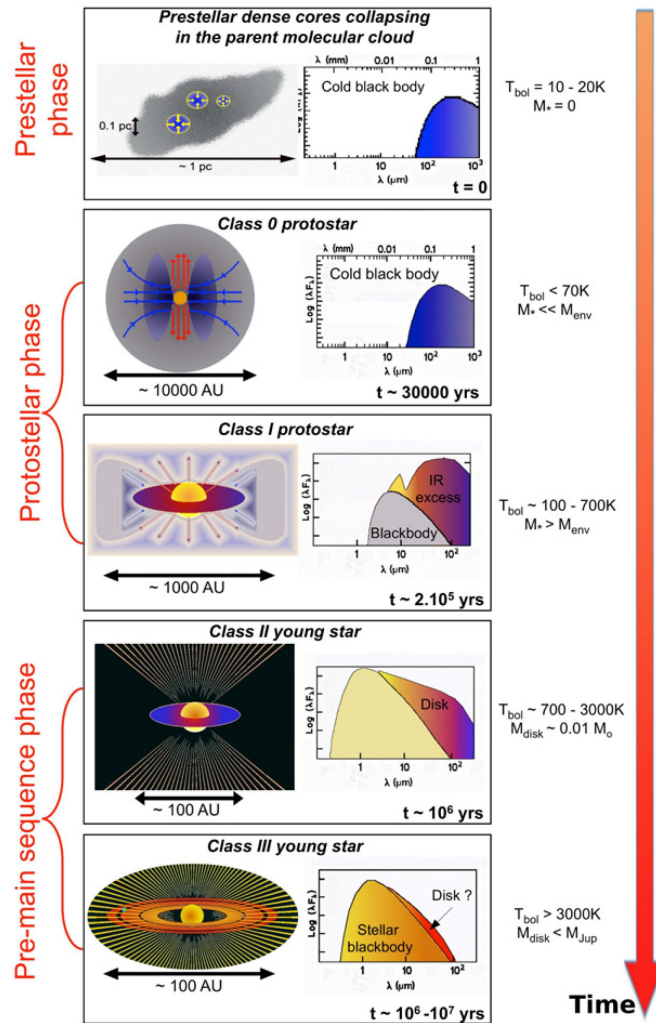


Figure 1.1: Schematic diagram of the evolutionary sequence proposed by André et al. 2002 and 2002. Showing the the evolution of SED with time.



1.2 Sources

1.2.1 L1157-mm

L1157 is a low-luminosity ($\sim 11 L_{\odot}$) class 0 protostar at a distance about 440 pc (Viotti, 1969). Spitzer IRAC image (Figure 1.2, Looney et al. 2007) shows a highly collimated bipolar outflow. It reveals an S-shaped point-symmetry and indicating that the direction of mass ejection varies by means of precession (Bachiller et al. 2001, Looney et al. 2007). This prominent outflow (Bachiller et al. 1997, and 2001) is discovered by Umemoto et al. (1992). This outflow is highly collimated and with high inclination angle (with respect to the line of sight, 80° , Gueth et al. 1996). Observations and detailed studies of this outflow have been done in many molecular lines, such as CO (Gueth et al. 1996, Bachiller et al. 1997, Hirano et al. 2001), H_2 (Hodapp 1994, Davis et al. 1995) and CH_3OH (Bachiller et al. 1995 and 2001, Avery et al. 1996). Especially the blue lobe of this outflow is well studied using the shock tracers such as SiO (Zhang et al. 1995 and 2000, Gueth et al. 1998, and Bachiller et al. 2001) and NH_3 (Bachiller et al. 1993, Tafalla et al. 1995, and Umemoto et al. 1999). Once the shocked gas is heated and compressed, some chemical reactions which are not easy to see in cold and quiescent cloud may happens. Observation in a wide range of wavelengths and detection of many transition lines (Bachiller et al. 2001) also shows that chemical variance and stratification, suggested that L1157 is the prototype of a chemically active outflow.

In addition to the prominent outflow, the Spitzer images shows an extinction perpendicular to the outflow axis, suggesting that there is an flatten envelope (Figure 1.2). The dust continuum in 2.7 mm (Gueth et al. 1997) reveals that continuum emission consists a marginally resolved compact, flattened core and a low level extended emission may delineates the edges of the cavity which is excavated by the CO outflow. ^{13}CO emission observed with the IRAM PdBI (Gueth et al. 1997) shows sign of envelope infall motion. Detection of methanol, which traces the warm layer in the infall-disk interface suggested there is accretion shock (Goldsmith et al. 1999, Velusamy et al. 2002). A combination of gravitational infall in the inner region and a slow, solid rotation at large scale is also suggested by N_2H^+ observation (Chiang et al. 2010). The rotation in small scale is probably been observed (Gueth et al. 1997)

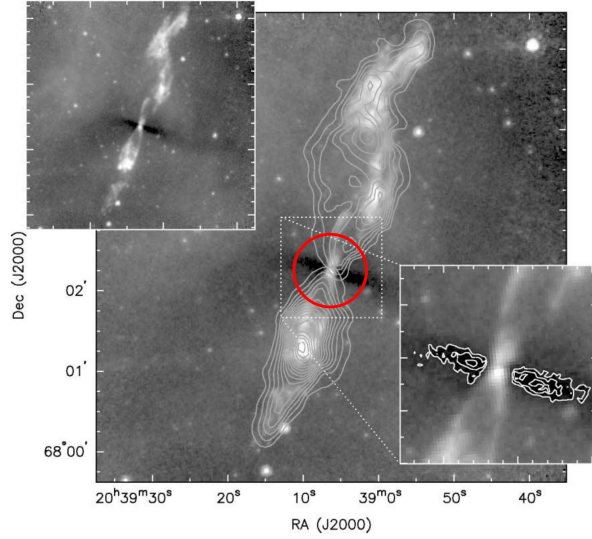


Figure 1.2: IRAC grey-scale image of L1157 overlaid with the CO 2-1 emission (Looney et al. 2007). The upper left inset is the same gray-scale without the contours. The lower right is a closeup of the absorption structure with contours. The red circle is the SMA 230 GHz field of view.

1.2.2 L1448C

L1448C is a class 0 protostar with low luminosity ($L_{bol} = 7.5 L_{\odot}$, Tobin et al. 2007) in the L1448 complex in the Perseus molecular cloud ($D \sim 220$ pc). Figure 1.3 (a) show the Spitzer IRAC image of the L1448 complex (Tobin et al. 2007). The red arrow points out the position of L1448C. The most characteristic feature is its highly collimated outflow. This outflow was also observed in the $^{12}\text{CO}(2-1)$ with the single dish telescope (Figure 1.3 (b), Bachiller et al. 1990). This molecular outflow is unique in many aspects: Its highest velocity ^{12}CO emission coincides with the axis of main outflow in the form of a narrow molecular jet, and moving with terminal radial velocity up to about 70 km s^{-1} ; It consists in a well defined chain of clumps (bullets), which are also symmetrically placed with respect to the central source (L1448C). This extremely high velocity (EHV) component is not only detected in ^{12}CO emission, but also in several transition of the SiO emission (Bachiller et al. 1991, Dutrey et al. 1997). The detection of SiO in EHV bullets suggests the presence of shocks that enhanced the abundance in gas. This outflow is also associated with a conical shell component with relatively lower velocity (Bachiller et al. 1995, Jørgensen et al. 2007, Maury et al. 2010, and Hirano et al. 2010).

Previous continuum observations show the effect of its outflow on the envelope: there is an extend feature along the outflow axis observed in 3 mm (Guilloteau et al. 1992), 2.6 mm (Bachiller et al. 1995), 1.37 mm (Schöier et al. 2004), 1.3 mm (Maury et al. 2010), and 0.85 mm (Hirano et al. 2010). The dust continuum emission also show a compact component, which is likely to be the circumstellar disk (1.3 mm, Terebey et al. 1993; 2.6 mm, Bachiller et al. 1995; Hirano et al. 2010).

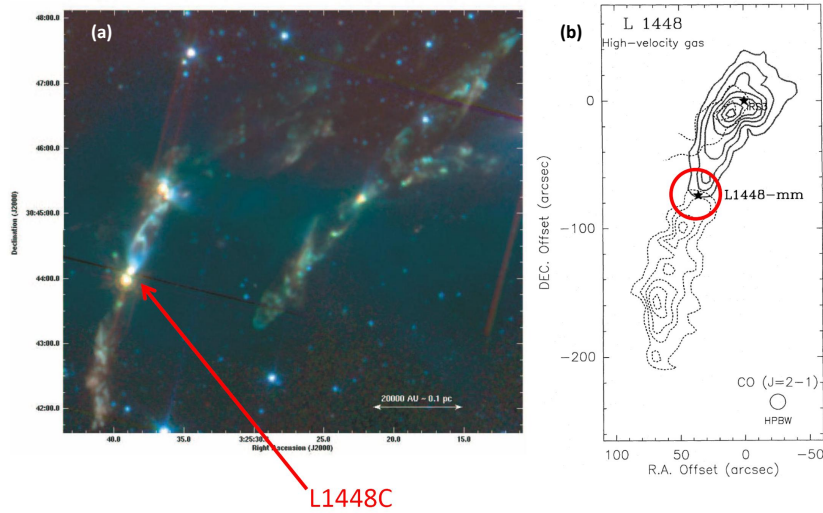


Figure 1.3: (a) IRAC image of L1448 (Tobin et al. 2007). The red arrow point out the position of L1448C. (b) CO map of the L1448 outflow (Bachiller et al. 1990). The solid contours are for the blueshifted emission and the dashed contours for the redshifted emission. The red circle is the SMA 230 GHz field of view.



Chapter 2

Observations and Data Reduction

The observations of L1157 and L1448C (Table 2.1) were carried out with The Submillimeter Array (SMA, Ho et al. 2004) as a part of the PROSAC project (Jorgensen et al. 2007). The SMA is a radio-interferometer made up of eight 6 meter diameter antennas located atop Mauna Kea in Hawaii.

The PROSAC project adopted three spectral settings. The first setup includes the J=2-1 transition of ^{12}CO and its isotopic lines using the 230 GHz receivers. The frequency coverage was from 219.5 to 220.3 GHz in the lower sideband and from 230.4 to 231.3 GHz in the upper sideband for the 230 GHz receiver. The second and third setups used the 345 GHz receivers; The second setup includes the CH_3OH J=7_k-6_k and SiO J=8-7 lines, ranging from 337.0 to 338.7 GHz in the lower sideband and from 346.9 to 348.6 GHz in the upper sideband, and the third setup includes the CS J=7-6 and H_2CO J=5_{1,5}-4_{1,4} lines, ranging from 342.0 to 342.9 GHz in the lower sideband and from 350.9 to 351.7 GHz in the upper sideband. The primary-beam size (HPBW) of the antennas at 230 GHz and 345 GHz were about 55'' and 36''.

The SMA correlator covers 2 GHz bandwidth in each of the two sidebands separated by 10 GHz. The upper sideband (USB) and the lower sideband (LSB) are each divided into 24 slightly overlapping chunks of 104 MHz width, each with a usable bandwidth of 82 MHz, which can be covered by varying spectral resolution. A hybrid resolution mode was used with 512, 256 and 128 channels per chunk for the high resolution (0.2, 0.4, 0.81 MHz resolution), 32 channels per chunk for the lower resolution (3.25 MHz resolution, line free chunks for continuum). The details of the spectral setups are shown in Table 2.2, 2.3 and 2.4.

The 2004 November and December observations were performed with the array in the Compact-North configuration. Others in 2005 were done with the array in

the Compact configuration. The detailed array configuration is summarized in Table 2.5.

The visibility data were calibrated using the MIR package, which was originally developed for Owens Valley Radio Observatory. The absolute flux density scale was determined by Uranus. Nearby quasars were used to calibrate relative amplitude and phase. We used bright quasars and Saturn as bandpass calibrators. Detail of the calibrators for each sources are summarized in Table 2.6. The calibrated visibility data were Fourier transformed and CLEANed using MIRIAD package. The maps were made with natural weighting. The synthesized beam size, noise level and velocity resolution are summarized in Table 2.7 and Table 2.8.

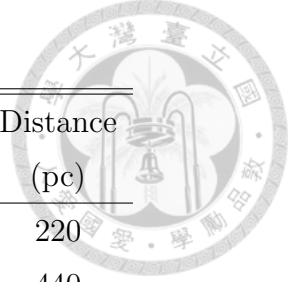


Table 2.1: Source Information

| Source | Pointing Center | | Distance (pc) |
|-----------------|---|-------------|------------------|
| | RA(J2000) | DEC(J2000) | |
| L1448C(N) | 03 ^h 25 ^m 38 ^s .80 | 30°44'05".0 | 220 |
| L1157 MM | 20 ^h 39 ^m 06 ^s .20 | 68°02'15".9 | 440 |
| NGC1333 IRAS 2A | 03 ^h 28 ^m 55 ^s .70 | 31°14'37".0 | 220 |

Table 2.2: Spectral Setup: 230 GHz

| Channels | Chunk | Sideband | Frequency Range | Lines |
|----------|-------|----------|-----------------|--|
| | | | (GHz) | |
| 512 | s13 | LSB | 220.238-220.342 | ¹³ CO (2-1) |
| | | USB | 230.407-230.511 | ... |
| | s23 | LSB | 219.506-219.610 | C ¹⁸ (2-1) |
| | | USB | 231.221-231.325 | (CH ₃ OH (10 _{2,9} -9 _{3,6} (A))) |
| 256 | s18 | LSB | 219.909-220.013 | SO (5 ₆ -4 ₅) |
| | | USB | 230.817-230.921 | ... |
| 128 | s14 | LSB | 220.225-220.329 | ... |
| | | USB | 230.489-230.593 | ¹² CO (2-1) |



Table 2.3: Spectral Setup: 337 GHz

| Channels | Chunk | Sideband | Frequency Range (GHz) | Lines |
|----------|-------|----------|--------------------------|---|
| 512 | s02 | LSB | 338.654-338.758 | CH ₃ OH (7 _{±2} -6 _{±2} (E)) |
| | | USB | 346.937-347.041 | H ¹³ CO ⁺ (4-3) |
| | s18 | LSB | 337.342-337.446 | C ³⁴ S (7-6) |
| | | USB | 348.249-348.353 | (HN ¹³ C (4-3)) |
| | s22 | LSB | 337.014-337.118 | C ¹⁷ O (3-2) |
| | | USB | 348.577-348.681 | SO ₂ (5 _{3,3} -6 _{0,6}) |
| 128 | s05 | LSB | 338.408-338.512 | CH ₃ OH (7 _k -6 _k) |
| | | USB | 347.183-348.287 | ... |
| | s06 | LSB | 338.326-338.430 | CH ₃ OH (7 ₋₁ -6 ₋₁ (E)) |
| | | | | CH ₃ OH (7 ₀ -6 ₀) |
| | | USB | 347.266-347.369 | SiO (8-7) |

Table 2.4: Spectral Setup: 342 GHz

| Channels | Chunk | Sideband | Frequency Range (GHz) | Lines |
|----------|-------|----------|--------------------------|---|
| 512 | s01 | LSB | 342.828-342.932 | CS (7-6) |
| | | USB | 350.947-351.051 | (NO (4-3)) |
| | s10 | LSB | 342.090-342.194 | ... |
| | | USB | 351.685-351.789 | H ₂ CO 5 _{1,5} -4 _{1,4} |
| 256 | s04 | LSB | 342.588-342.696 | (CH ₃ OHO (12 _{3,10} -22 _{1,11})) |
| | | USB | 351.187-351.291 | (SO ₂ (5 _{3,3} -4 _{2,2})) |



Table 2.5: Observation Log

| Source | Observation Date | Setting (GHz) | Array Configuration |
|-----------|------------------|------------------|---------------------|
| L1448C(N) | 2004 November 21 | 342 | Compact-North |
| | 2004 November 14 | 337 | Compact-North |
| | 2005 December 3 | 342 | Compact |
| L1157-mm | 2005 July 3 | 337 | Compact |
| | 2005 July 6 | 230 | Compact |
| | 2005 August 22 | 342 | Compact |

Table 2.6: Calibrators

| Source | Flux Calibrator | Bandpass Calibrators | Gain Calibrators |
|-----------|-----------------|----------------------|------------------|
| L1448C(N) | Uranus | Saturn | 3C84 |
| | | 3C273(342 GHz) | |
| L1157-mm | Uranus | 3C434 | 1642+689 |
| | | | 2200+420 |



Table 2.7: Observational Parameters of L1157

| Line | Transition | Rest Frequency (GHz) | Frequency Resolution (MHz) | Velocity Resolution (km/s) | Noise Level (mJy/Beam) | Beam Size (P.A.) |
|----------------------------|-------------------|----------------------|----------------------------|----------------------------|------------------------|--|
| ^{12}CO | 2-1 | 230.538 | 0.81 | 1.06 | 217 | $4''.23 \times 2''.57$ (-47°) |
| ^{13}CO | 2-1 | 220.399 | 0.20 | 0.28 | 300 | $4''.62 \times 3''.35$ ($-50^\circ.3$) |
| C^{18}O | 2-1 | 219.560 | 0.20 | 0.28 | 319 | $4''.64 \times 3''.36$ ($-50^\circ.3$) |
| C^{17}O | 3-2 | 337.061 | 0.20 | 0.18 | 461 | $2''.77 \times 2''.15$ ($-30^\circ.9$) |
| H^{13}CO^+ | 4-3 | 346.998 | 0.20 | 0.18 | 490 | $2''.68 \times 2''.08$ ($-30^\circ.7$) |
| CS | 7-6 | 342.883 | 0.20 | 0.17 | 450 | $2''.74 \times 2''.27$ ($-17^\circ.2$) |
| H_2CO | $5_{1,5}-4_{1,4}$ | 351.769 | 0.20 | 0.18 | 578 | $2''.80 \times 2''.14$ ($-19^\circ.3$) |
| Continuum | | | | | | |
| 1.3mm | ... | ... | ... | ... | 4.56 | $4''.31 \times 2''.67$ ($-47^\circ.3$) |
| 0.8mm | ... | ... | ... | ... | 7.88 | $2''.76 \times 2''.14$ ($-30^\circ.9$) |
| | | | | | 7.86 | $3''.12 \times 2''.06$ ($-9^\circ.8$) |



Table 2.8: Observational parameters of L1448

| Line | Transition | Rest Frequency (GHz) | Frequency Resolution (MHz) | Velocity Resolution (km/s) | Noise Level (mJy/Beam) | Beam Size (P.A.) |
|-------------------------|-------------------|----------------------|----------------------------|----------------------------|------------------------|--|
| ^{12}CO | 2-1 | 230.538 | 3.25 | 4.23 | 48 | $2''.62 \times 1''.85$ ($-6^\circ.2$) |
| ^{13}CO | 2-1 | 220.399 | 0.20 | 0.28 | 153 | $2''.86 \times 2''.02$ ($-5^\circ.9$) |
| C^{18}O | 2-1 | 219.560 | 0.20 | 0.28 | 180 | $2''.87 \times 2''.03$ ($-5^\circ.9$) |
| CH_3OH | 7_{-1-6-1} | 338.345 | 0.81 | 0.72 | 305 | $1''.66 \times 1''.15$ ($-79^\circ.3$) |
| SiO | 8-7 | 347.331 | 0.81 | 0.70 | 164 | $1''.66 \times 1''.16$ ($-70^\circ.4$) |
| CS | 7-6 | 342.883 | 0.20 | 0.18 | 212 | $2''.27 \times 1''.88$ ($-33^\circ.4$) |
| H_2CO | $5_{1,5-4_{1,4}}$ | 351.769 | 0.20 | 0.17 | 182 | $2''.12 \times 1''.93$ ($-7^\circ.0$) |
| Continuum | | | | | | |
| 1.3mm | ... | ... | ... | ... | 2.20 | $2''.88 \times 2''.04$ ($-5^\circ.9$) |
| 0.8mm | ... | ... | ... | ... | 7.59 | $1''.81 \times 1''.87$ ($-74^\circ.9$) |
| | | | | | 6.02 | $2''.97 \times 1''.97$ ($-29^\circ.8$) |



Chapter 3

Results

3.1 L1157

3.1.1 230 GHz and 345 GHz Continuum emissions

Figure 3.1 shows the natural weight maps of the 1.3 mm and 0.85 mm continuum emission. The synthesized beam of the 1.3 mm map was $4''.49 \times 3''.25$ (1900 AU \times 1180 AU) with a PA $\cong -50.2^\circ$ for 1.3 mm, and that of the 0.85 mm map was $3''.10 \times 1''.99$ (1360 AU \times 870 AU) with a PA $\cong -15^\circ$. In order to get the peak position of the central emission, the images were fitted with two-dimensional gaussian using the MIRIAD task IMFIT. The peak position of each wavelength map is listed in Table 3.1. It is in agreement (Offset: RA $\sim -0^s.06$, Dec $\sim +0.72''$) with the previous PdBI 1.3 mm observation with higher angular resolution ($1''.24 \times 1''.22$): R.A(J2000) = $20^h39^m06^s.24$, Dec(J2000) = $68^\circ02'15''.6$ (Beltrán et al. 2004). The total integrated flux, deconvolved size and position angle are also estimated and listed in Table 3.1.

Figure 3.1 suggests that 0.85 mm emission consists of two components. One is specially extended component elongated along the NE-SW direction, and the other is the compact component. In the visibility amplitude plot (Figure 3.2), the extended component dominates the flux at a uv-distance of $< 30 \text{ k}\lambda$, and the compact component is prominent at $> 30 \text{ k}\lambda$. The visibility data of 0.85 mm emission can be fitted with two circular gaussian components: one is a compact component with a size of about $1''.41 \pm 0''.19$ ($\sim 620 \text{ AU}$) and a flux of $\sim 450 \pm 60 \text{ mJy}$, and the other is an extended component with a size of $\sim 5''.40 \pm 0''.58$ ($\sim 2400 \text{ AU}$) and a flux of $\sim 660 \pm 64 \text{ mJy}$. The size of the compact component is consistent to that derived in the previous 2.7 mm data ($1''.24 \pm 0''.09 \times 0''.89 \pm 0''.06$, 550×400

AU) of Gueth et al. 1997). It is likely that the compact component comes from the circumstellar disk.

In order to estimate how much flux was recovered with the SMA, we compared our results with those of the previous single-dish measurements. The 1.3 mm flux observed with the 10'' beam of the IRAM-30 m telescope was 630 mJy (Motte and André et al. 2001). Therefore, the SMA recovered $\sim 70\%$ of the 1.3 mm flux. The 0.85 mm flux measured with the JCMT SCUBA was 2200 mJy within a 20'' area. This implies that the 0.85 mm flux recovered by the SMA was only $\sim 30\%$ of the single-dish flux.

Table 3.1: 2D Gaussian fit result

| | 1.3 mm | 0.85 mm |
|-----------------------------|----------------------|----------------------|
| R.A.(J2000) | $20^h39^m06^s.18$ | $20^h39^m06^s.25$ |
| Dec.(J2000) | $68^\circ02'16''.33$ | $68^\circ02'15''.81$ |
| Total integrated flux (mJy) | 420 | 692 |
| Deconvolved Size: | | |
| Major axis(arcsec) | 4.46 | 2.45 |
| Minor axis(arcsec) | 2.95 | 1.43 |
| Position angle(degree) | -55 | 71.3 |

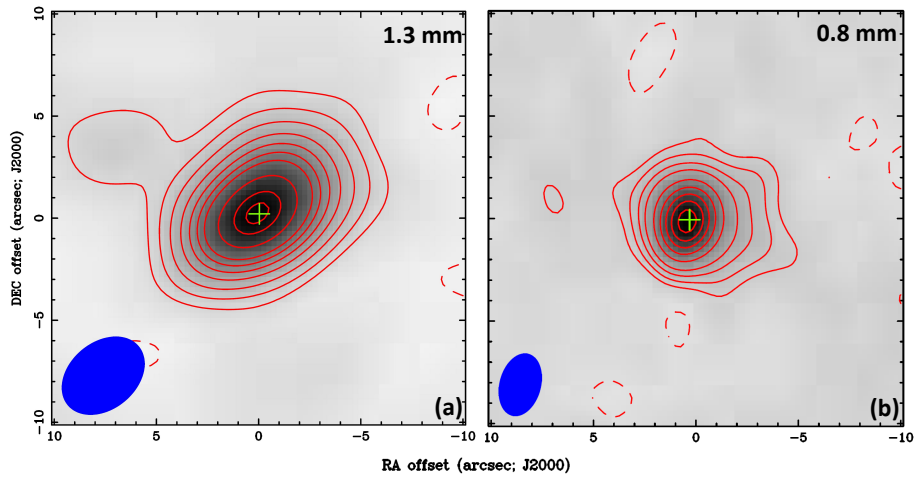


Figure 3.1: 1.3 mm and 0.85 mm continuum map of L1157 (contours and linear gray scale). Red contour levels are $-3, 3, 6, 10, 15, 20, 25, 30, 40, 50$ and 55σ , where 1σ is 4.0 mJy for (a) 1.3 mm and $-3, 3, 6, 10, 15, 20, 25, 30$ and 33σ , where 1σ is 6.1 mJy for (b) 0.85 mm. The green crosses indicate the peak of 1.3 and 0.85 mm continuum. The filled ellipses at the bottom left corner show the synthesized beams.

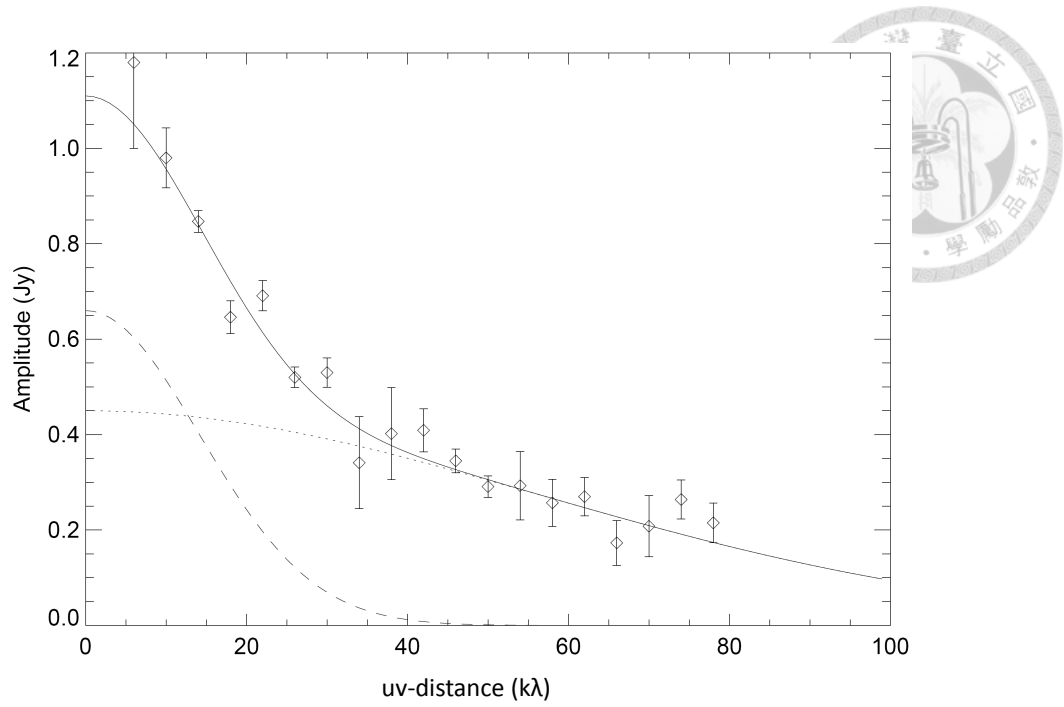


Figure 3.2: Visibility amplitude versus uv distance plot for the 0.85 mm continuum emission with 1σ error bars. The dashed line is the fitted curve for the extended component and the dotted line is the fitted curve for the compact component. The solid curve is the total amplitude of the two components.



Table 3.2: Photometric Data of L1157

| Wavelength (μm) | Flux Density (Jy) | Error (Jy) | Note |
|---------------------------------|----------------------|----------------------|------|
| 12 | 6.6×10^{-2} | 1.1×10^{-2} | 1 |
| 24 | 0.08 | 7.5×10^{-3} | 2 |
| 25 | 0.226 | 0.016 | 1 |
| 60 | 9.97 | 0.5 | 1 |
| 100 | 43.51 | 8.6 | 1 |
| 160 | 42 | 1.7 | 3 |
| 200 | 38.6 | 7.7 | 3 |
| 450 | 6 | 1.2 | 4 |
| 850 | 0.9 | 0.18 | 4 |
| 850 | 0.692 | 2.3×10^{-2} | 0 |
| 1300 | 0.4 | 0.04 | 4 |
| 1300 | 0.42 | 6.7×10^{-3} | 0 |
| 2700 | 3.5×10^{-2} | 3.5×10^{-3} | 5 |
| 3400 | 2.0×10^{-2} | 2.0×10^{-3} | 6 |

1. Beichman, C. A. et al. 1998; 2. Jason M. Kirk et al. 2009 ; 3. Froebrich, D. et al. 2003; 4. Chini, R. et al. 2001; 5. Gueth, F. et al. 1997; 6. Choi, Minho et al. 1999; 0. our results

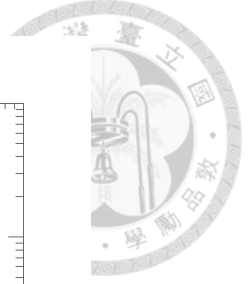
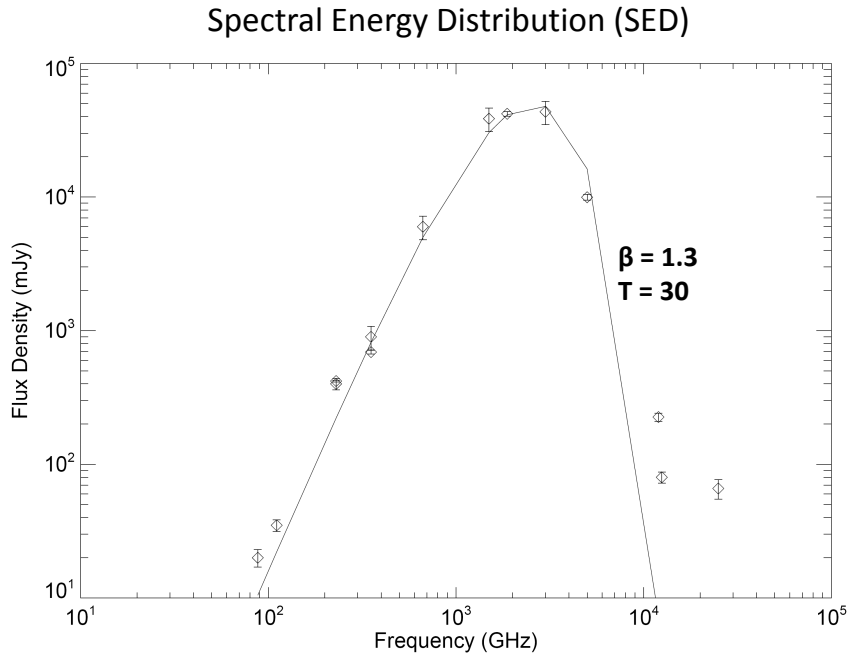


Figure 3.3: Spectral energy distributions of L1157. The data are from IRAS satellite (12 μm with FWHM $45'' \times 300''$, 25 μm with FWHM $45'' \times 300''$ and 60 μm with FWHM $90'' \times 300''$, and 100 μm with FWHM $180'' \times 300''$), MIPS with resolution about $6''$ (24 μm), ISOPHOT with aperture size about $45''$ (160 μm and 200 μm), JCMT SCUBA with resolution about $10''$ (450 μm , 850 μm , and 1300 μm), SMA with resolution around $3''$ (0.85 mm and 1.3 mm), IRAM with resolution about $2''.5$ (2.7 mm) and BIMA with resolution about $10''$ (3.4 mm). The black curve is the fit with $T_{dust} \approx 30$ K and $\beta = 1.3$.

The Spectral energy distribution (SED) of L1157 is shown in Figure 3.3. The SED was fitted with the form, grey-body radiation, and with single emissivity, β , and temperature, T_{dust} ,

$$F_\nu = \Omega B(T_{dust})(1 - e^{-\tau_\nu})$$

where F_ν is the total flux density, Ω is the solid angle of the emitting region, τ_ν is the optical depth of dust that is assumed to be proportional to ν^β , T_{dust} is the dust temperature, and B is the Planck function. The photometric data in different wavelength is shown in Table 3.2. The SED is fitted by the dust temperature $T_{dust} = 30$ K and $\beta = 1.3$.

In order to study the physical properties, the bolometric luminosity, L_{bol} , and bolometric temperature, T_{bol} , were estimated. These quantities have been suggested to be indicators of stellar age and mass (Myers & Ladd 1993; Myers et al. 1998). These values were calculated as follows:

$$L_{LW} = 4\pi D^2 \int_0^\infty F_\nu d\nu$$

for longer wavelength, and

$$L_{IRAS} = 4\pi D^2 \times (F_{12} + F_{25})$$

for IRAS data, then

$$L_{bol} = L_{LW} + L_{IRAS}$$

$$T_{bol} = 1.25 \times 10^{-11} \bar{\nu}$$

where D is the distance to the source (440 pc) and $\bar{\nu}$ is the mean frequency of the grey-body spectra, which is also derived from (Myers & Ladd 1993)

$$\bar{\nu} = \frac{\int_0^\infty \nu F_\nu d\nu}{\int_0^\infty F_\nu d\nu}$$

The results are $L_{bol} \approx 9.5 L_\odot$ and $T_{bol} \approx 40$ K.

Assuming that the continuum emission is optically thin, the total gas mass (M_{gas}) has been estimated as follows:

$$M_{gas} = \frac{F_\nu D^2}{\kappa_{230GHz} B(T_{dust})}$$

The dust mass opacity was assumed to be

$$\kappa_\nu = 0.1 \times \left(\frac{\nu}{10^{12}}\right)^\beta$$

(Beckwith et al. 1990). With $\beta = 1.3$, the κ_ν is calculated to be 0.014 and 0.025 $\text{cm}^2 \text{g}^{-1}$ at $\nu = 230$ and 345 GHz, respectively. The derived gas mass (M_{gas}) is about 0.5 and 0.3 M_\odot in 230 and 345 GHz, respectively.

3.1.2 ^{12}CO (2-1) Molecular Line

The ^{12}CO (2-1) emission is detected in the velocity ranges from $V_{lsr} = -13$ to 2.8 km s^{-1} , and from 3.9 to 16.5 km s^{-1} . Figure 3.4 shows the moment 0 map of ^{12}CO (2-1) in these velocity ranges. The velocity ranges are blueshifted (blue contour) and redshifted (red contour) with respect to the ambient cloud velocity of 2.60 ± 0.05 km s^{-1} (from C^{18}O spectra in Gueth et al. 1997). There is no significant emission in the velocity range from 2.8 to 3.9 km s^{-1} . The blue-shifted emission delineates a V-shaped structure open to the southeast. The opening angle of this V-shaped structure is about 40° . On the other hand, the red-shifted emission shows a triangle structure in the northwest of the driving source. There are two kinds of asymmetries in this ^{12}CO map. First, the intensity of the southern blue lobe is brighter than that of the northern red lobe. This result is consistent with the previous ^{12}CO (2-1) single dish result (Bachiller et al. 2001). Second, there is an asymmetry between the eastern and western side of each lobes; the blue lobe is brighter in the eastern wall, while the red lobe is brighter in the western wall.

Figure 3.5 presents position-velocity (P-V) diagram of the ^{12}CO (2-1) emission along the outflow direction (P.A. = 155°). There are two different velocity components in this PV diagram; the High velocity component (from -12 to -4 km s^{-1} in blue lobe; from 8 to 16 km s^{-1} in red lobe) around the central source, and the low velocity component (from -4 to 8 km s^{-1}) with spatially extended feature.

Figure 3.6 shows the high velocity emission comes from the narrow ridge-like region with a position angle of about 140° . The blue ridge coincides with the eastern wall of the blue lobe, and the red ridge coincides with the western wall of the red lobe. The spatial distribution of the high velocity component suggests that the direction of the recent mass ejection is along the ridge (PA= 140°), which is different from the axis of the V-shaped (or triangle) structure (PA= 155°). Previous ^{12}CO and SiO observation also show direction change between ejection events from one episode to others (Gueth et al. 1997, Zhang et al. 2000/Bachiller et al. 2001). They suggest that the outflow axis may precess over its lifetime, and present a simple precession model with different precession angle (6° in Gueth; 15° in Zhang and Bachiller).

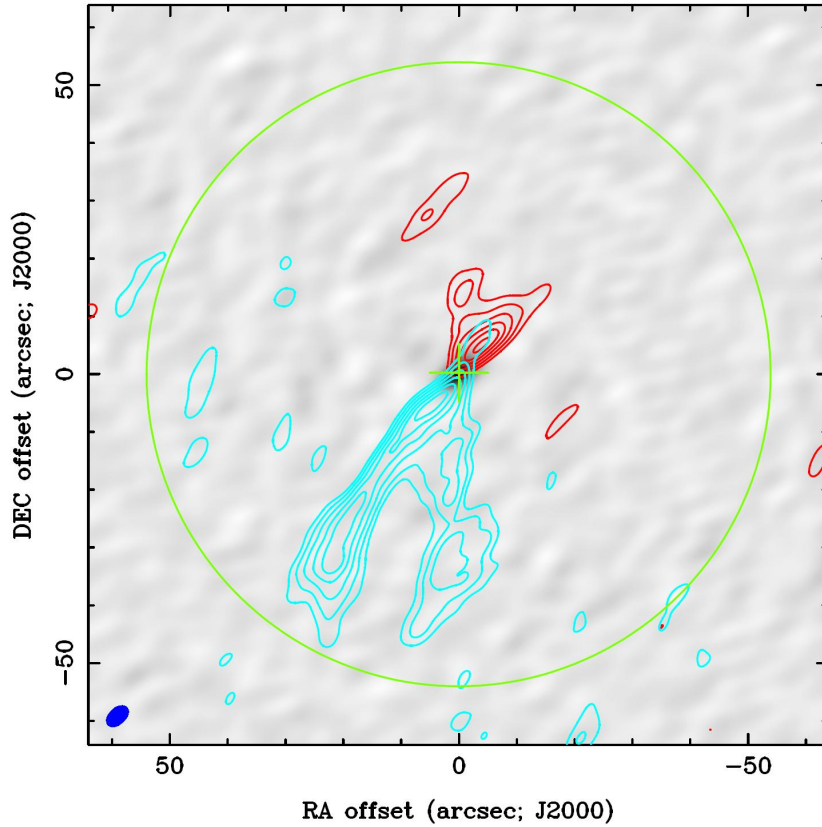


Figure 3.4: Total integrated intensity map of ^{12}CO (2-1)(contours) overlaid on the 1.3 mm continuum grey scale. The blue and red contours indicate the blueshifted component ($-12 \sim 2.2 \text{ km s}^{-1}$) and redshifted component ($4.3 \sim 16 \text{ km s}^{-1}$), respectively. Contours are $-3, 3, 6, 10, 15, 20, 25\sigma$ with 1σ are $1.7 \text{ Jy Beam}^{-1} \text{ km s}^{-1}$ for red contours and $2.0 \text{ Jy Beam}^{-1} \text{ km s}^{-1}$ for blue contours. Green circle is the FOV about 54, and the cross indicates the peak of 1.3 mm continuum.

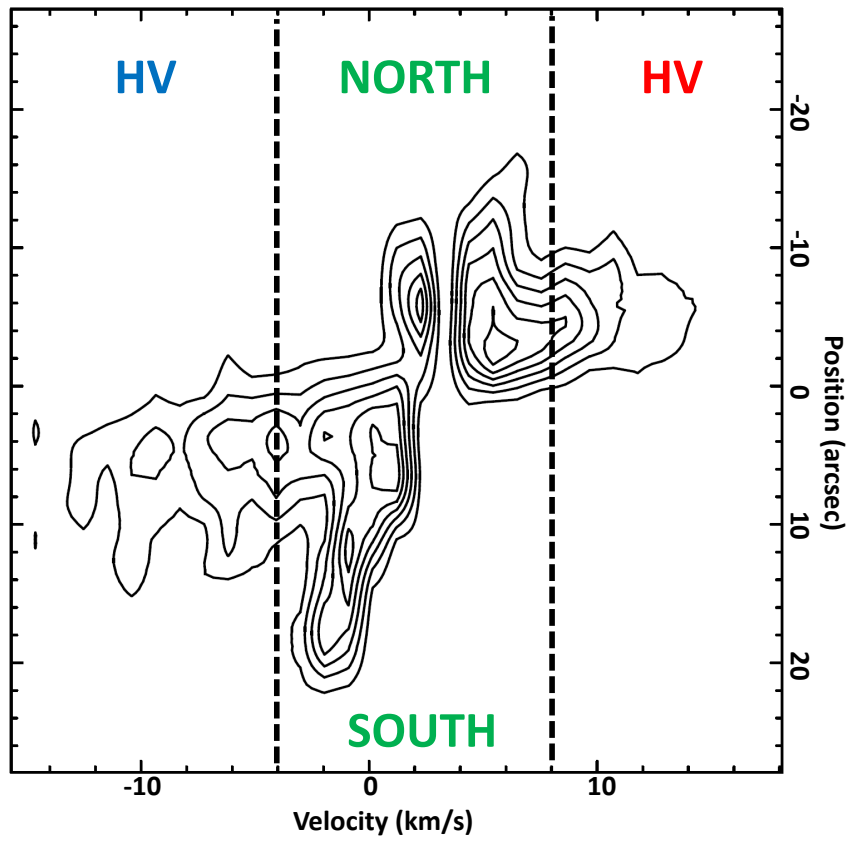


Figure 3.5: P-V diagram of the ^{12}CO (2-1) emission along the outflow axis in L1157. Black dotted lines divide the ^{12}CO emission into two different velocity components, high and low velocity. Contour levels are 0.97, 1.94, 2.91, 3.88, 4.85, 5.82 Jy Beam $^{-1}$

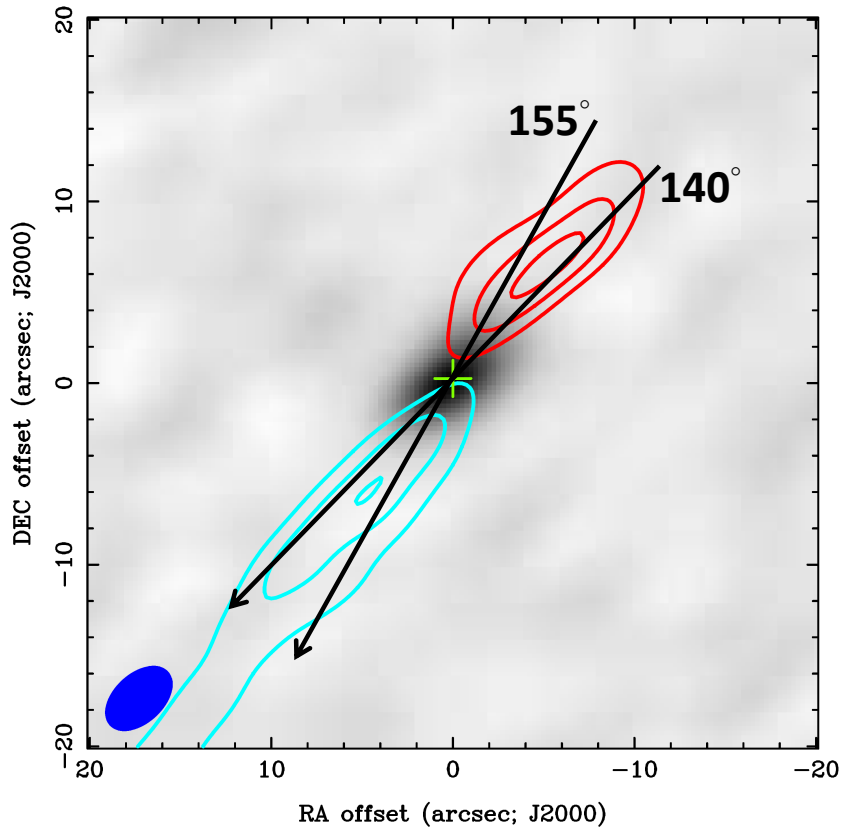


Figure 3.6: moment 0 map (contours) of the HV(from -4 to -12(blue); 8 to 16(red) km s^{-1}) component of ^{12}CO emission. Contours are drawn every 3σ steps with the lowest contour at 3σ , where 1σ is $2.25 \text{ Jy Beam}^{-1} \text{ km s}^{-1}$ for red and $2.86 \text{ Jy Beam}^{-1} \text{ km s}^{-1}$ for blue. Grey scale is the 1.3 mm continuum emission. The green cross shows the peak position of the continuum. The two black arrowed lines shows the direction of the HV component(140°), and the direction of outflow(155°).

3.1.3 ^{13}CO (2-1) Molecular Line

The ^{13}CO (2-1) emission is detected in the velocity range from 0.84 to 3.90 km s $^{-1}$. Figure 3.7 is the moment 0 map in this velocity range overlaid with ^{12}CO grey scale image. The ^{13}CO emission shows V-shaped structure open to the southeast, and coincides with the walls of the ^{12}CO south lobe.

Figure 3.8 presents the ^{13}CO distribution in three velocity ranges. Figure 3.8 (a) and (c) show triangle-shaped structure in blueshifted component and redshifted component, which are consistent with the morphology of the base of ^{12}CO outflow. The ^{13}CO emission near the cloud systemic velocity (Figure 3.8 (b)) shows an elongated feature center at the protostellar position. This suggests that the ^{13}CO emission in this velocity range comes from the envelope.

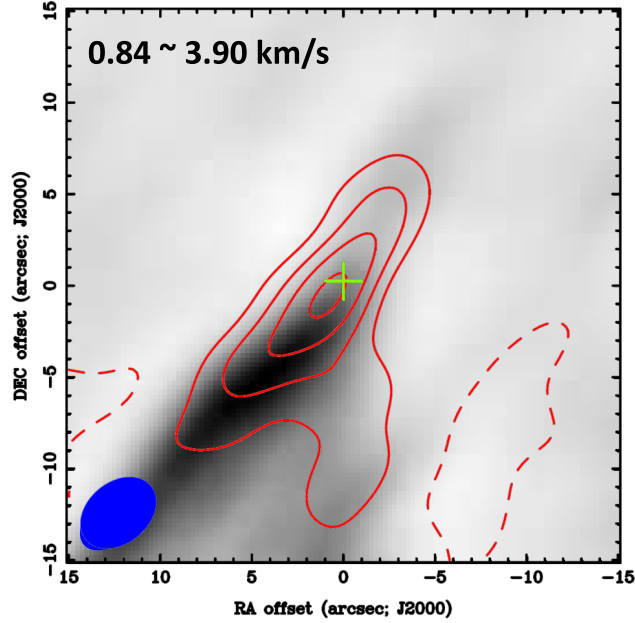


Figure 3.7: The moment 0 of ^{13}CO (2-1) emission. contour levels are from 3σ to 12σ in steps of 3σ , where 1σ is $0.4 \text{ Jy Beam}^{-1} \text{ km s}^{-1}$. Crosses represent the peak position of 1.3 mm continuum, and the filled ellipse at the bottom left corner in each panels shows the synthesized beam.

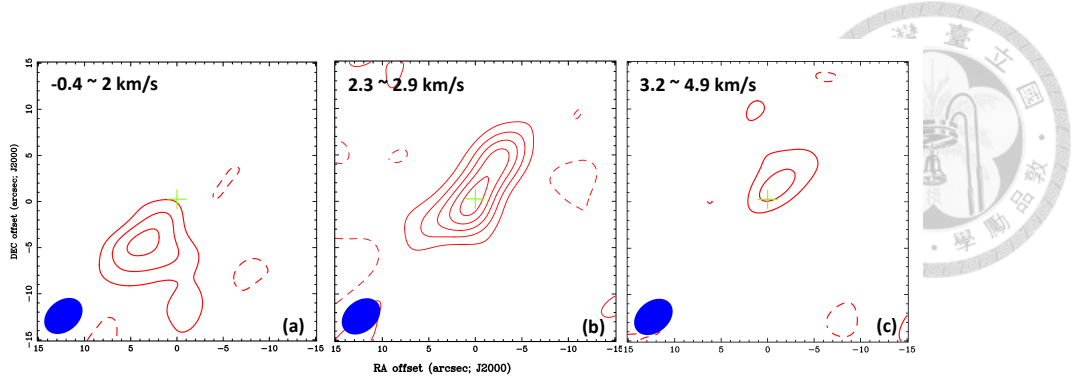


Figure 3.8: Moment 0 maps of ^{13}CO (2-1) at three different velocity ranges. (a) For the blueshifted component, contour levels are from 3σ to 9σ in steps of 3σ , where 1σ is $0.28 \text{ Jy Beam}^{-1} \text{ km s}^{-1}$. (b) For the component around the systemic velocity (2.7 km s^{-1}), contour levels are from 3σ to 15σ in steps of 3σ , where 1σ is $0.16 \text{ Jy Beam}^{-1} \text{ km s}^{-1}$. (c) For the redshifted component, contour levels are from 3σ to 6σ in steps of 3σ , where 1σ is $0.24 \text{ Jy Beam}^{-1} \text{ km s}^{-1}$. Crosses represent the peak position of 1.3 mm continuum, and the filled ellipse at the bottom left corner in each panels shows the synthesized beam.

3.1.4 Physical parameters of ^{12}CO (2-1) emission

We estimated the outflow mass using the ^{12}CO (2-1) and ^{13}CO (2-1) data corrected for the primary beam attenuation. We assumed a LTE condition with an excitation temperature of 30 K, which is same as the dust temperature. We adopted the $[\frac{H_2}{^{12}\text{CO}}] \cong 10^4$ and a mean atomic weight of the gas of 1.36. A comparison between the velocity range of ^{12}CO and that of ^{13}CO suggests that the ^{12}CO may be optically thick in the low-velocity blueshifted component at $V_{lsr} = 0.84 \sim 2.8 \text{ km s}^{-1}$. In this velocity range where the ^{13}CO and ^{12}CO emission both exist, we estimated the optical depth of the ^{12}CO (2-1) line using the following equation

$$\frac{S_\nu(^{12}\text{CO})}{S_\nu(^{13}\text{CO})} = \frac{[^{12}\text{CO}]}{[^{13}\text{CO}]} \left(\frac{1 - e^{-\tau}}{\tau} \right)$$

where the S_ν is the intensity, τ is the optical depth of the ^{12}CO (2-1) emission and the $[\frac{^{12}\text{CO}}{^{13}\text{CO}}] = 77$ (Wilson & Rodd 1994). The optical depth of the ^{12}CO emission in the low-velocity blueshifted component is ~ 3.37 . Thus, the outflow masses in the optically thick velocity channels were corrected using the following equation

$$M_{thick} = \sum m(v_i) = \sum m'(v_i) \left[\frac{\tau_i}{1 - e^{-\tau(v_i)}} \right],$$

where $m'(v_i)$ is the mass at velocity v_i without optical depth correction; $m(v_i)$ is the mass after optical depth correction; τ_i represents the optical depth at velocity v_i . Outside the velocity of ^{13}CO emission, the ^{12}CO emission is assumed to be optically thin, and obtained the mass by

$$M_{thin} = \sum m'(v_i),$$

and with this equation:

$$M_{thin} = 36.3 \times \frac{(d_{kpc})^2}{\nu_{GHz}^3} \times \frac{e^{2.78 \frac{J_L(J_L+1)}{T_{ex}}}}{J_L + 1} \int S_\nu \frac{T_{ex} + 0.9267}{e^{\frac{-h\nu}{\kappa T_{ex}}}} dv$$

with $J_L=1$ and $\nu_{GHz}^3 = 230.538 \text{ GHz}$. Then, the total mass of the outflow was obtained by

$$M_{total} = M_{thin} + M_{thick},$$

The total masses in redshifted and blueshifted lobes are summarized in Table 3.3. Since there is missing flux in the velocity range around systemic velocity due to the lack of short spacing data, the masses estimated here are the lower limits. The total mass in blueshifted component is significantly larger than redshifted component

about two orders of magnitude. This is probably because the ambient gas in front of the protostar is much more than the gas behind the protostar. The redshifted component of the outflow may expand more freely, while the blueshifted component in the front needs to push more material.

The momentum (P_{12CO}), the force (F_{12CO}) and mechanical luminosity (L_{12CO}) of the outflow lobes are also estimated using the velocity channel maps and following equations,

$$P_{12CO} = \sum M_i \times \Delta V_i$$

$$F_{12CO} = \frac{\sum M_i \times \Delta V_i}{t_d}$$

$$L_{12CO} = \frac{\frac{1}{2} \sum M_i \times \Delta V_i^2}{t_d}$$

where i are the different velocity channels and $\Delta V_i = V_i - V_{sys}$. The dynamical time scale of the outflow, t_d , are calculated by l/\bar{V} , where l is the length of the outflow lobe and the \bar{V} is the mean velocity corrected by the flow inclination ($\sim 80^\circ$, from the line of sight). The parameters of the two lobes in different velocity ranges are also listed in Table 3.3.

Table 3.3 Parameters of the ^{12}CO line emission

| | Mass (M_\odot) | Momentum ($M_\odot \text{ km s}^{-1}$) | Time Scale (yr) | Force ($M_\odot \text{ km s}^{-1} \text{ yr}^{-1}$) | Luminosity (L_\odot) |
|----------|-----------------------|---|--------------------|--|-----------------------------|
| Red | 5.81×10^{-3} | 0.031 | 1180 | 2.61×10^{-5} | 1.42×10^{-2} |
| Blue | 1.0×10^{-1} | 0.413 | 2410 | 1.71×10^{-4} | 8.98×10^{-2} |
| Red(HV) | 7.19×10^{-4} | 0.017 | 560 | 3.06×10^{-5} | 2.32×10^{-2} |
| Blue(HV) | 1.42×10^{-3} | 0.186 | 688 | 2.71×10^{-4} | 2.09×10^{-1} |

3.1.5 C¹⁸O (2-1), C¹⁷O (3-2) and H¹³CO⁺ (4-3)

Molecular Line

The C¹⁸O (2-1) emission is detected in the velocity range from $V_{lsr} = 1.3$ to 3.5 km s⁻¹. Figure 3.9 (a) shows the moment 0 map of the C¹⁸O emission in this velocity range. The C¹⁸O emission shows an elongation structure in the outflow direction (deconvolved size & P.A.: $6''.9 \times 2''.6$, $\sim 3000 \times 1200$ AU, $-25^\circ.8$) with emission peak close to the central protostellar position. Although, most of the C¹⁸O emission comes from the systemic velocity (Figure 3.10); there is a velocity gradient along the major axis of the envelope: redshifted component to the north and blueshifted component to the south of the protostellar position, which is same as the outflow (Figure 3.10). Such a velocity gradient in the C¹⁸O emission, which is same as outflow, is also seen in other class 0 protostars like RNO43 and IRAS3282 (Héctor G. Arce et al. 2006). It is likely that the envelope is affected by the outflow. Figure 3.11 shows P-V diagrams of the C¹⁸O emission along the minor axis (perpendicular to the outflow, 65°). There is a possible velocity gradient along the minor axis: blue in the south-west and red in the north-east of the protostellar position ($\Delta R \simeq \pm 1''$, $\simeq 880$ AU; velocity gradient $\sim 2.27 \times 10^{-4}$ km s⁻¹ AU⁻¹). After the primary beam correction has been done, we estimate the mass of envelope by assuming the excitation temperature (T_{ex}) of 30 K, an optically thin assumption and local thermodynamic equilibrium (LTE) condition, respectively. And by using the following equations for C¹⁸O:

$$M = 2.22 \times 10^4 \times \frac{(d_{kpc})^2}{\nu_{GHz}^3} \times \frac{e^{2.6356 \frac{J_L(J_L+1)}{T_{ex}}}}{J_L + 1} \int S_\nu \frac{T_{ex} + 0.8785}{e^{\frac{-h\nu}{kT_{ex}}}} \frac{\tau}{1 - e^{-\tau}} dv,$$

with $J_L=1$, $\nu_{GHz}^3 = 219.560$ GHz and abundance of $[\frac{C^{18}O}{H_2}] \cong 1.7 \times 10^{-7}$ (Frerking et al. 1982).

Figure 3.9 (b) and (c) show the moment 0 maps of the C¹⁷O (3-2) and H¹³CO⁺ (4-3) integrated from $V_{LSR} = 1.5$ to 3.5 km s⁻¹ and $V_{LSR} = 2$ to 3 km s⁻¹, respectively. They are more compact than C¹⁸O emission. We also estimate the mass using C¹⁷O and H¹³CO⁺ lines by assuming the excitation temperature (T_{ex}) of 30 K, an optically thin assumption and local thermodynamic equilibrium (LTE) condition, respectively. And by using the following equations and for C¹⁷O:

$$M = 2.24 \times 10^4 \times \frac{(d_{kpc})^2}{\nu_{GHz}^3} \times \frac{e^{2.78 \frac{J_L(J_L+1)}{T_{ex}}}}{J_L + 1} \int S_\nu \frac{T_{ex} + 0.9267}{e^{\frac{-h\nu}{kT_{ex}}}} \frac{\tau}{1 - e^{-\tau}} dv,$$

with $J_L=2$, $\nu_{GHz}^3 = 337.061$ GHz and abundance of $[\frac{C^{17}O}{H_2}] \cong 1.5 \times 10^{-7}$ (J. E. Lee et al. 2003), and for $H^{13}CO^+$:

$$M = 1.01 \times 10^4 \times \frac{(d_{kpc})^2}{\nu_{GHz}^3} \times \frac{e^{2.08 \frac{J_L(J_L+1)}{T_{ex}}}}{J_L + 1} \int S_\nu \frac{T_{ex} + 0.693}{e^{\frac{-h\nu}{kT_{ex}}}} \frac{\tau}{1 - e^{-\tau}} d\nu,$$

with $J_L=3$, $\nu_{GHz}^3 = 346.99$ GHz and abundance of $[\frac{H^{13}CO^+}{H_2}] \cong 3.5 \times 10^{-10}$ (Bachiller et al. 1997). The masses are estimated about $0.22M_\odot$, $0.054M_\odot$ and $0.014M_\odot$ for $C^{18}O$, $C^{17}O$ and $H^{13}CO^+$, respectively. From the masses we estimated $C^{18}O$ emission seems to trace the largest region within these three.

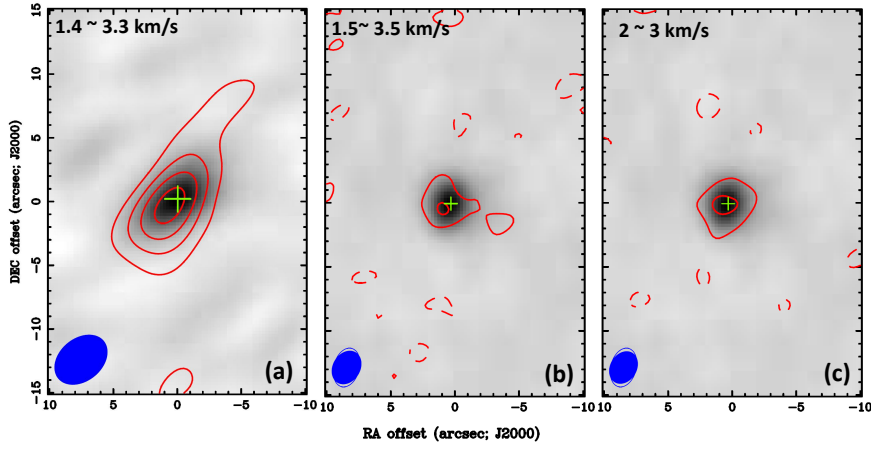


Figure 3.9: Moment 0 maps of different molecular lines overlaid on the 1.3 mm and 0.8 mm continuum grey scale. (a) $C^{18}O$: Contour levels are from 3σ to 12σ in steps of 3σ , where 1σ is $0.27 \text{ Jy Beam}^{-1} \text{ km s}^{-1}$. (b) $C^{17}O$: Contour levels are from 3σ to 6σ in steps of 3σ , where 1σ is $0.43 \text{ Jy Beam}^{-1} \text{ km s}^{-1}$. (c) $H^{13}CO^+$: Contour levels are from 3σ to 6σ in steps of 3σ , where 1σ is $0.43 \text{ Jy Beam}^{-1} \text{ km s}^{-1}$. Crosses represent the peak position of 1.3 mm and 0.8 mm continuum, and the filled ellipse at the bottom left corner in each panels shows the synthesized beam.

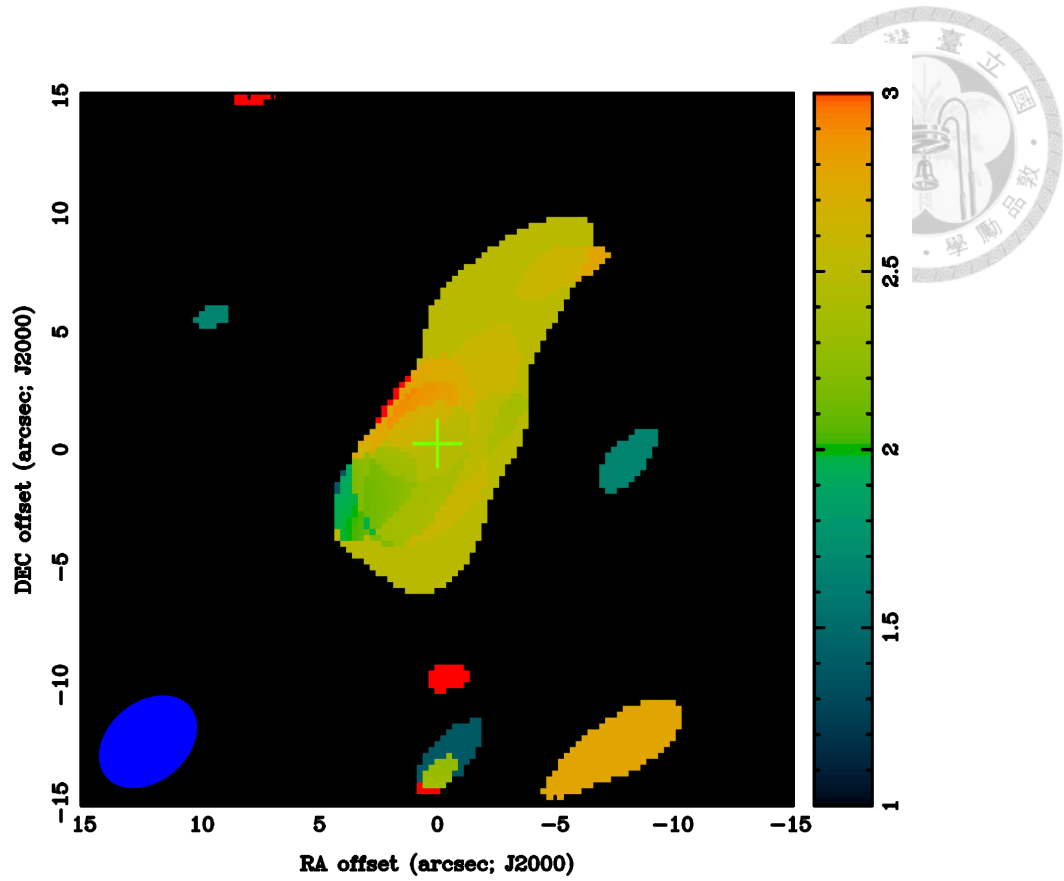


Figure 3.10: Moment 1 map of the C^{18}O (2-1). The color scales ranged from 1 to 3 km/s. cross shows the position of 1.3 mm continuum. Filled ellipse at the bottom left corner shows the synthesized beam.

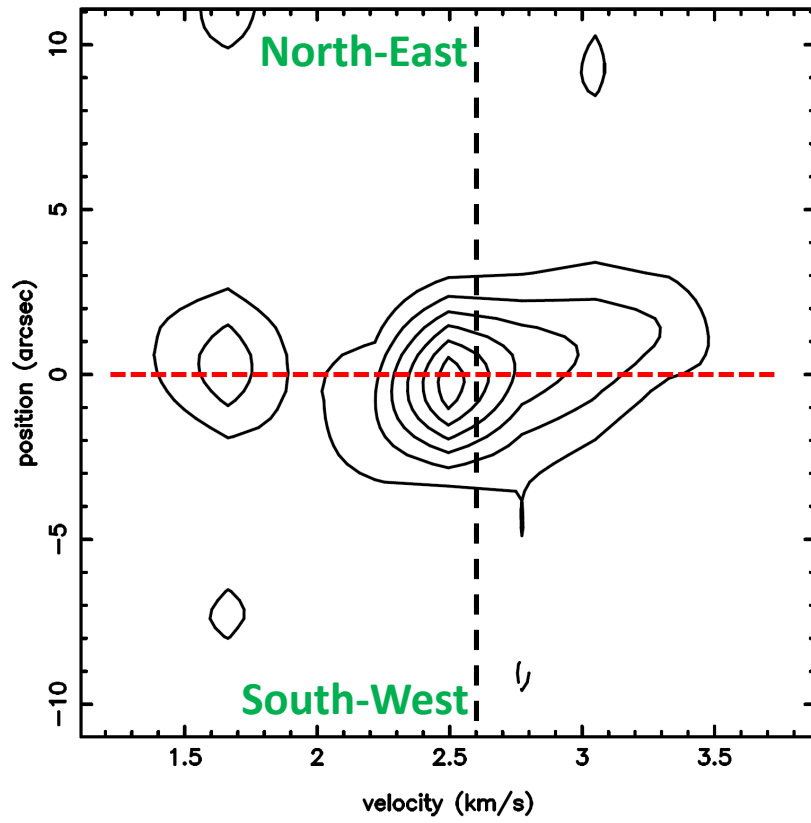


Figure 3.11: P-V diagram of the $C^{18}O$ (2-1) emission along the minor axis (PA=65°) in L1157. Black dashed line indicates the systemic velocity (2.6 km/s). Contour levels are 0.64, 1.27, 1.91, 2.55, 3.19, 3.82 Jy Beam⁻¹.

3.1.6 CS (7-6) and H₂CO (5_{1,5} – 4_{1,4}) Molecular Lines

The CS (7-6) and H₂CO (5_{1,5} – 4_{1,4}) emission lines are detected in the velocity ranges of $V_{lsr} = 2.3$ to 3.5 km s⁻¹ and $V_{LSR} = 2.3$ to 4.3 km s⁻¹, respectively. Figure 3.12 are the moment 0 maps of CS and H₂CO emission in the above velocity ranges. Most of the CS and H₂CO emission show compact structure around the protostellar position. In addition to the component around the center, there are protrusions toward the north-west in both molecular lines. Two dimensional Gaussian fitting to each line show the deconvolved size are about $7''.2 \times 2''.9$ (~ 3200 AU \times 1300 AU, PA = -25°) for CS line; and are about $9''.1 \times 3''.1$ (~ 4000 AU \times 1300 AU, PA = -36°) for H₂CO line. The PV-diagram (Figure 3.13) along the outflow show that the emission around the protostar is slightly redshifted with respect to the V_{sys} , which the components at the north is blueshifted to the V_{sys} . The velocity gradient shown in PV-diagram appear to be opposite to that seen in the C¹⁸O line, and ¹²CO outflow, in which the red lobe is at the north and blue lobe is at the south. These opposite velocity gradient feature are also seen in L1551 IRS 5 (Takakuwa et al. 2011), L483 and B335 (Takakuwa et al. 2007).

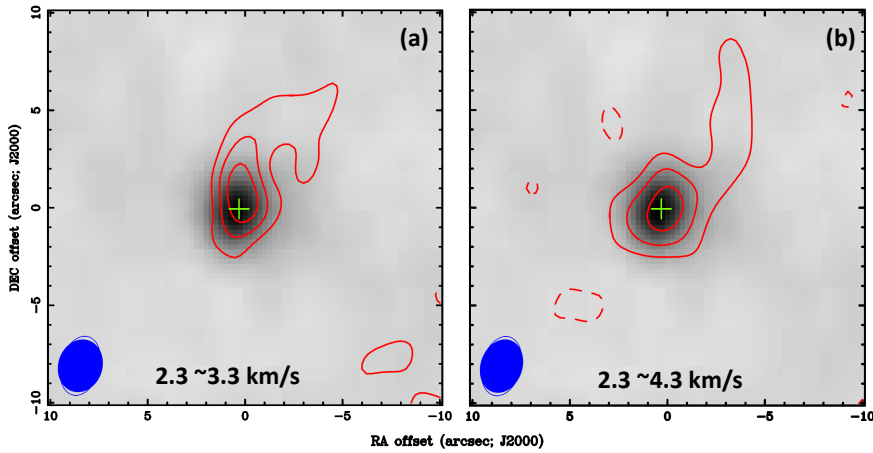


Figure 3.12: Moment 0 maps of different molecular line contours overlaid on the 0.8 mm continuum grey scale. (a)CS (7-6): Contour levels are from 3 to 9 in steps of 3, where 1 is 0.28 Jy Beam⁻¹ km s⁻¹. (b)H₂CO (5_{1,5} – 4_{1,4}): Contour levels are from 3 to 9 in steps of 3, where 1 is 0.38 Jy Beam⁻¹ km s⁻¹. Crosses represent the peak position of 0.8 mm continuum, and the filled ellipse at the bottom left corner in each panels shows the synthesized beam.

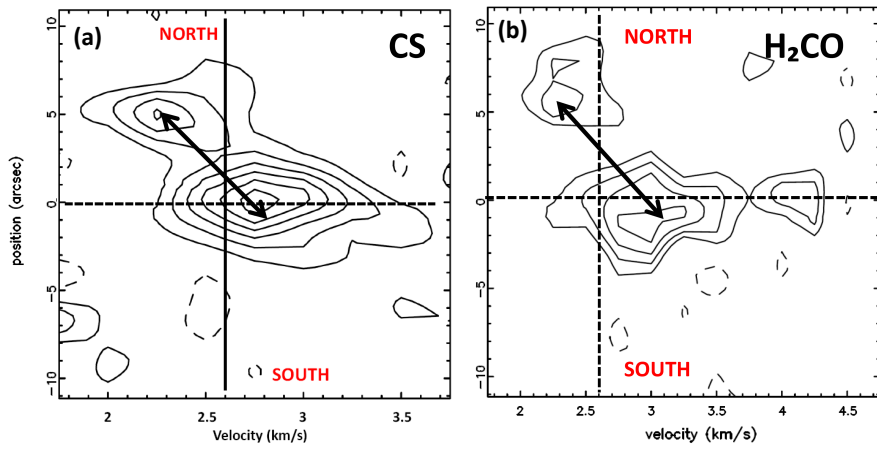


Figure 3.13: P-V diagram of the CS (7-6) emission along the outflow axis in L1157(155°). Black dashed lines indicates the systemic velocity. Contour levels are 0.59, 1.17, 1.76, 2.34, 2.93, 3.52 Jy Beam⁻¹.

3.2 L1448C

3.2.1 230 GHz and 345 GHz Continuum emissions

Figure 3.14 shows the natural weight maps of the 1.3 mm and 0.85 mm continuum emission. The angular resolutions are $2''.88 \times 2''.04$ (650 AU \times 460 AU) at PA $\cong -59.4^\circ$ for 1.3 mm, and $2''.09 \times 1''.71$ (520 AU \times 430 AU) at PA $\cong -55^\circ$ for 0.85 mm, respectively. In order to get the peak position of the central emission, the images was fitted with two-dimensional gaussian with the MIRIAD task IMFIT. The peak positions obtained in two wavelengths (listed in Table 3.3) coincide well with the 3.6 cm continuum position observed with the higher resolution ($0''.31 \times 0''.27$) VLA observation by Reipurth et al. (2002). These continuum peaks correspond to the position of L1448C(N). The total integrated flux, deconvolved size and position angle are also estimated and listed in Table 3.3.

As in the case of L1157, the 0.85 mm continuum consists of two components; one is specially extended with two protrusions toward southeast and southwest; the other is compact around the peak position. The visibility amplitude profile of the 0.85 mm continuum emission (Figure 3.15) is fitted by two circular gaussian components; one is a compact component with a size of $\sim 0''.90 \pm 0''.18$ ($\sim 190 \pm 40$ AU) and a flux of ~ 413 mJy, and the other is an extended component with a size of $\sim 7''.47 \pm 1''.6$ and a flux of ~ 1190 mJy. As in the case of L1157, the compact component is consider to be a circumstellar disk. Previous 350 GHz continuum observation also suggests that there is a possible circumstellar disk surrounding the protostar with size: $0''.37 \times 0''.26$ (90 AU \times 65 AU, Hirano et al. 2010).

The 0.85 mm image shows another emission component to the southeast. The green cross is the position of L1448C(S) : R.A(J2000) = $3^h25^m39^s.14$, Dec(J2000) = $30^\circ43'58''.3$ (Jørgensen et al. 2007), which is consistent with our 6σ peak. The flux was measured to be ~ 70 mJy, which is consistent with the 350 GHz result (~ 60 mJy; Hirano et al. 2010). However, L1448C(S) was not detected in the 1.3 mm.

The Spectral energy distribution (SED) of L1448C is shown in Figure 3.16. The SED was fitted with the form of grey-body radiation with a single emissivity, β , and temperature, T_{dust} ,

$$F_\nu = \Omega B(T_{dust})(1 - e^{-\tau_\nu})$$

where F_ν is the total flux density, Ω is the solid angle of the emitting region, τ_ν is the optical depth of dust that is assumed to be proportional to ν^β , T_{dust} is the

dust temperature, and B is the Planck function. The photometric data in different wavelength is shown in Table 3.4. The SED is fitted by the dust temperature $T_{dust} = 30$ K and $\beta = 1.3$. The physical properties, the bolometric luminosity, L_{bol} , bolometric temperature, T_{bol} and total gas mass, M_{gas} , were also estimated with the same methods and assumptions described in section 3.1.1. We obtained $L_{bol} \approx 5.7 L_{\odot}$, $T_{bol} \approx 40$ K; and the gas mass (M_{gas}) of $\sim 0.062 M_{\odot}$.

Table 3.3: 2D Gaussian fit result

| | 1.3 mm | 0.85 mm |
|-----------------------------|---------------------------|---------------------------|
| R.A.(J2000) | $3^h 25^m 38^s .883$ | $3^h 25^m 38^s .869$ |
| Dec.(J2000) | $30^{\circ} 44' 05'' .50$ | $30^{\circ} 44' 05'' .39$ |
| Total integrated flux (mJy) | 182 | 529 |
| Deconvolved Size: | | |
| Major axis(arcsec) | 1.948 | 1.199 |
| Minor axis(arcsec) | 0.925 | 1.045 |
| Position angle(degree) | -30.6 | -41.8 |

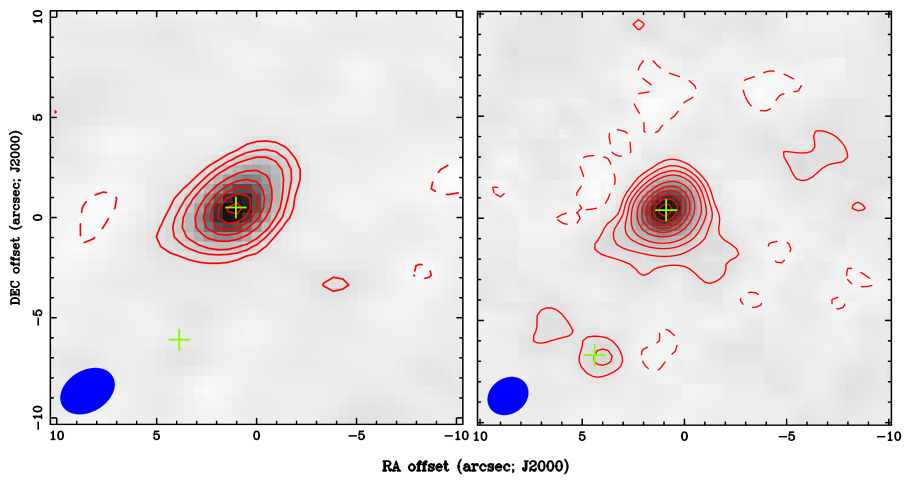


Figure 3.14: 1.3 mm and 0.85 mm continuum map of L1448C (contours and linear gray scale). Red contour levels are $-3, 3, 6, 10, 20, 30, 40, 50$ and 60σ , where 1σ is 2.2 mJy for (a) 1.3 mm and $-3, 3, 6, 10, 15, 25, 35, 45, 55, 65$ and 75σ , where 1σ is 5.1 mJy for (b) 0.85 mm. The green crosses indicate the peak of 1.3 and 0.85 mm continuum in L1448C(N) and L1448C(S). The filled ellipses at the bottom left corner show the synthesized beams.

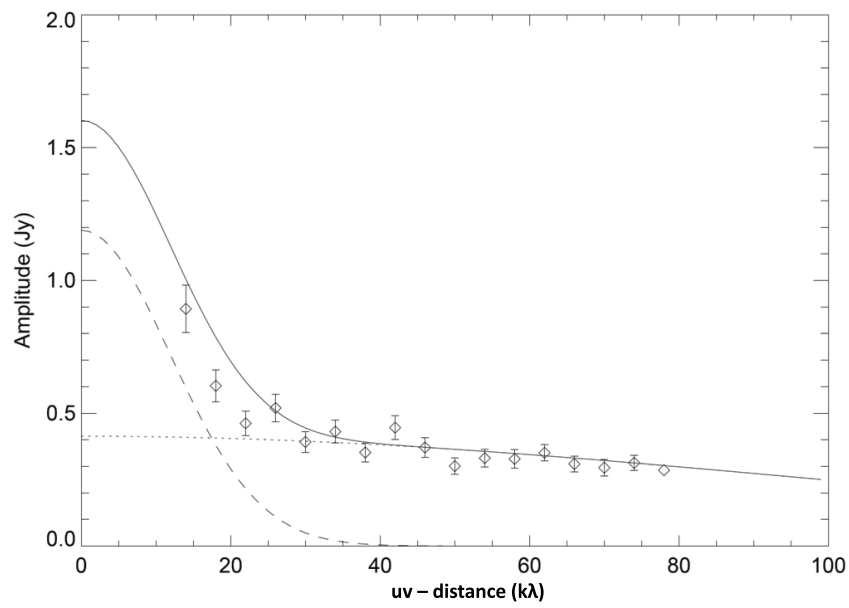
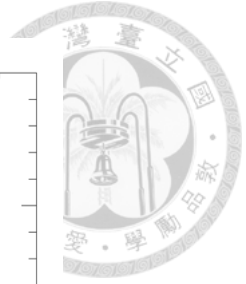


Figure 3.15: Visibility amplitude versus uv distance plot for the 0.85 mm continuum emission with 1σ error bars. The dashed line is the fitted curve for the extended component and the dotted line is the fitted curve for the compact component. The solid curve is the total amplitude of the two components.



Table 3.4: Photometric Data of L1448C

| Wavelength (μm) | Flux Density (Jy) | Error (Jy) | Ref. |
|---------------------------------|----------------------|---------------|------|
| 12 | 0.33 | 0.07 | 3 |
| 17.9 | 0.73 | 0.14 | 1 |
| 20.8 | 0.55 | 0.17 | 1 |
| 24 | 1.56 | 0.043 | 2 |
| 24.5 | 2.37 | 1.52 | 1 |
| 25 | 2.9 | 0.6 | 3 |
| 60 | 31.2 | 6.5 | 3 |
| 100 | 70.3 | 14,8 | 3 |
| 350 | 30 | 3 | 3 |
| 450 | 21 | 2 | 3 |
| 800 | 3 | 0.3 | 3 |
| 850 | 0.529 | 0.05 | 0 |
| 1300 | 0.182 | 0.018 | 0 |
| 1370 | 0.32 | 0.032 | 7 |
| 2600 | 0.091 | 0.002 | 4 |
| 3500 | 0.026 | 0.002 | 5 |
| 3500 | 0.016 | 0.001 | 6 |

1. O'Linger, J. C. et al. 2006; 2. Jørgensen et al. 2006 3. Barsony, M. et al. 1998;
4. Bachiller, R. et al. 1995; 5. Bachiller, R. et al. 1991; 6. Guilloteau, S. et al.
1992; 7. Schöier, F. L. et al. 2004 0. our results.

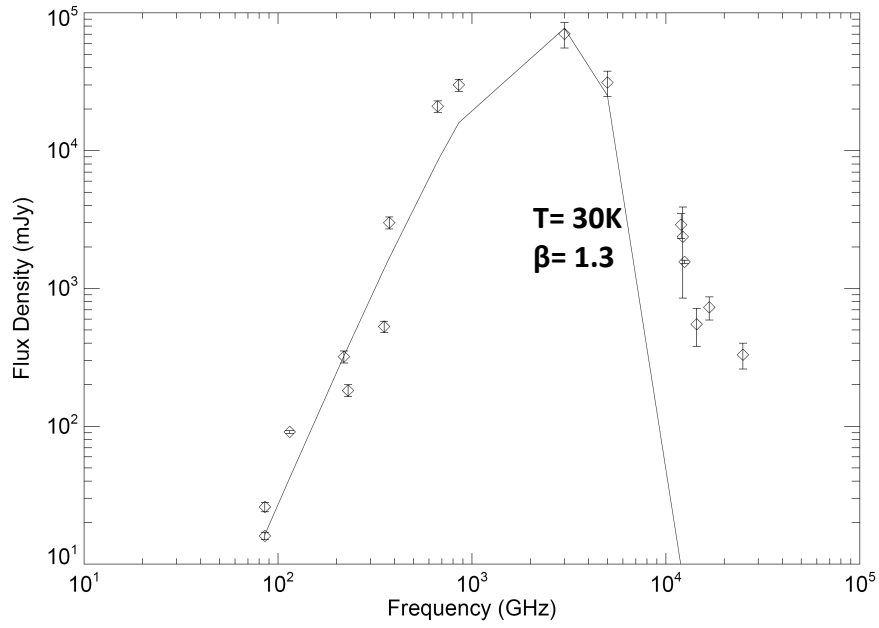


Figure 3.16: Spectral energy distributions of L1448C. The data are from IRAS satellite (12 μm with FWHM $45'' \times 267''$, 25 μm with FWHM $45'' \times 279''$ and 60 μm with FWHM $90'' \times 285''$ and 100 μm with FWHM $180'' \times 303''$), IRTF MIRLIN (17.9 μm , 20.8 μm , 24.5 μm , with resolution $1''.29$, $1''.50$, $1''.77$, respectively) MIPS with resolution about $2''.4$ (24 μm), JCMT (350 μm with resolution $19''.5$, 450 μm with resolution $18''.5$ and 850 μm with resolution about $16''.5$), SMA with resolution about $2''$ (0.8 mm and 1.3 mm), OVRO with resolution about $2''$, IRAM PdBI with resolution about $3''$ (2.6 mm and 3.5 mm). The black curve is the fit with $T_{dust} \approx 30$ K and $\beta = 1.3$.

3.2.2 Outflow: ^{12}CO (2-1), SO (5_6-4_5), SiO (8-7)

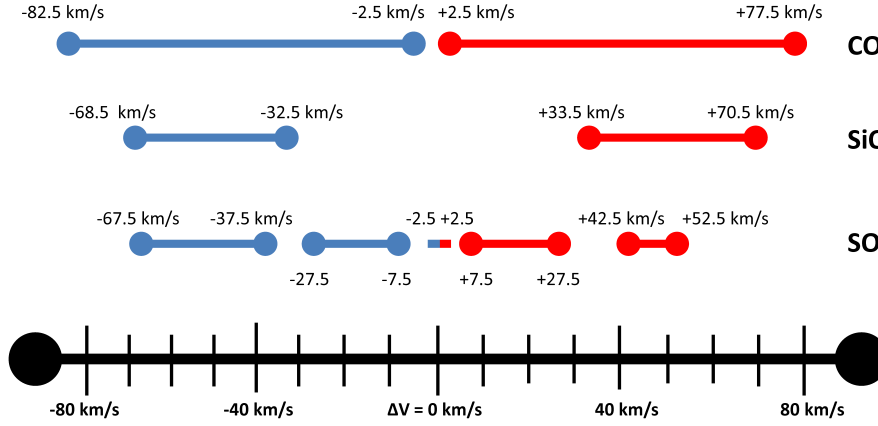


Figure 3.17: Scheme of velocity ranges of ^{12}CO (2-1), SiO (8-7) and SO (5_6-4_5) emission detected from our SMA observation. The velocity values are all with respect to systemic velocity ($\sim 5 \text{ km s}^{-1}$). The blue and red colors represent the blueshifted and redshifted velocity ranges, respectively.

Three molecular lines, ^{12}CO (2-1), SO (5_6-4_5) and SiO (8-7), are detected in the velocity ranges shown above in Figure 3.17. Figure 3.18 shows the spectra of these three lines in three different position. The middle column represents the profile toward the central stellar position; the left and right columns represent the profile toward the position $\sim 1''$ southeast and northwest away from the central position (along the outflow axis).

Although these three lines are possible tracers of outflowing gas, the prominent emission peak in each line appears in the different velocity. For example, at the position of $\sim 1''$ SE, the ^{12}CO shows a prominent peak at $\Delta V \sim +5 \text{ km s}^{-1}$, with a secondary peak at $\Delta V \sim +50 \sim +60 \text{ km s}^{-1}$; the SiO only has one prominent peak at $\Delta V \sim +45 \sim +55 \text{ km s}^{-1}$; and the SO shows one prominent peak at $\Delta V \sim +25 \text{ km s}^{-1}$, and the other at $\Delta V \sim +55 \text{ km s}^{-1}$. In addition, the SO spectrum at the protostellar position shows an emission peak around the systemic velocity. These results suggest that ^{12}CO , SiO and SO emission arises from different components: they all have components with extremely high velocity ($\Delta V \geq \pm 50 \text{ km s}^{-1}$); ^{12}CO and SO instead have components with lower velocity, but they are not consistent due to the different peak velocity.

For the purpose of comparing morphology of different velocity components, we present the velocity-channel maps at 20 km s^{-1} intervals. Figure 3.19 show the

^{12}CO (2-1) maps. The ^{12}CO (2-1) in the low velocity (Figure 3.19 (d)) delineates the V-shaped structures open to the southeast (redshifted lobe), and to the northwest (blueshifted lobe). The opening angle of the redshifted lobe is $\sim 30^\circ$. In the blueshifted lobe, the emission in the western wall is more extended and brighter than eastern wall, A comparison between Figure 3.19 (c) and (d) suggests that the opening angles of the red and blue lobes become narrower as the velocity increases.

In higher velocity components (a) and (b), neither the blueshifted or redshifted emission shows V-shaped structure. Instead, the CO emission comes from a narrow jet-like region. We estimated the ^{12}CO flux recovered by the SMA by comparing the ^{12}CO (2-1) spectra observed by the SMA with those observed by the IRAM-30 m telescope (Schiller et al. 1990). The SMA maps were convolved to be a $12''$ circular beam in order to match the beam of the IRAM-30m. We found that almost 90% \sim 100% of the ^{12}CO flux in the velocity range of $\Delta V = \pm 42.5 \sim \pm 82.5 \text{ km s}^{-1}$ were recovered by the SMA. This suggests that almost all the ^{12}CO (2-1) flux in velocity ranges of Figure 3.19 (a) and (b) come from the narrow jet.

The emission in (a) and (b) also show clumpy structure, which was seen in previous single dish ^{12}CO (2-1) result (Bachiller et al.1990). However, our ^{12}CO (2-1) emission mostly comes from the R1 and B1 pair in single dish map. The significant knots seen in ^{12}CO (2-1) map correspond to the B1-C and R1-C pair and the BII-a and RII-a pair in the ^{12}CO (3-2) map of Hirano et al. (2010). Other knots seen in the ^{12}CO (3-2) map are not clearly seen in the ^{12}CO (2-1) map, probably because of the insufficient angular resolution. The axes of red and blue lobe are also misaligned by $\sim 5^\circ$ (Red $\sim -25^\circ$; Blue $\sim -20^\circ$) as in the case of the ^{12}CO (3-2) emission. The position angle also changes slightly at $\pm 8''$ from the central source as in the case of ^{12}CO (3-2) jet.

Figure 3.20 presents position-velocity (P-V) diagram of the ^{12}CO (2-1) emission along the outflow axes (P.A. = -25° for blueshifted part, and -20° for the redshifted part). There are obviously two different velocity components in this PV diagram. One is in the velocity ranges of $\Delta V = \sim \pm 30 \text{ km s}^{-1}$ to $\pm 80 \text{ km s}^{-1}$, the other is in the velocity ranges of $\Delta V \leq \pm 30 \text{ km s}^{-1}$, corresponds to the low velocity component. The velocity pattern of low velocity component is similar to that of the ^{12}CO outflow in L1157. It shows a spatially extended feature and a Hubble-law like feature, suggesting that this component traces the outflow shell as in the case of L1157. The velocity of the extremely high velocity component rapidly increases and reaches to highest velocity ($\sim \pm 60 \text{ km s}^{-1}$ from V_{sys}) at $\pm 2''$ from the central

source.

Figure 3.19 (c) and (d) shows a blueshifted component in the redshifted lobe. This component is located to the northeast of L1448C(S). There is an extended redshifted component to the southwest of the L1448C(S). These blueshifted and redshifted components are likely to be related to the outflow activity of L1448C(S). This outflow is more collimated in this lower velocity range than the outflow of L1448C(N). This outflow does not appear in the higher velocity ranges shown in Figure 3.19 (a) and (b). The significant enhancement and the bending of the west wall of the redshifted outflow in L1448C(N) could be caused by the overlapping of these two outflow.

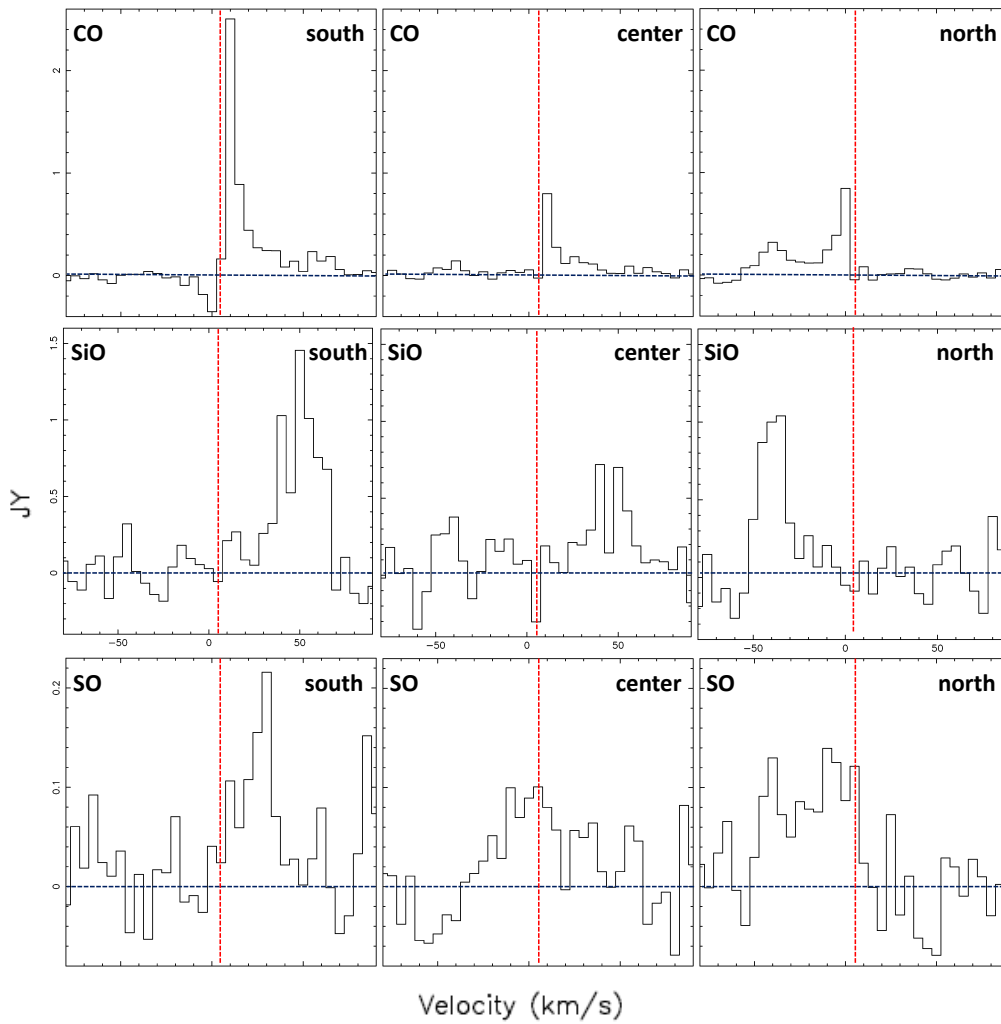


Figure 3.18: The spectra of the ^{12}CO (2-1), SiO (7-8) and SO (5_6-4_5) line emissions in three positions. South and North: $\sim \pm 1''$ away from protostellar position. Center: protostellar position. The black and red dashed represent the 0 Jy level and systemic velocity, respectively.

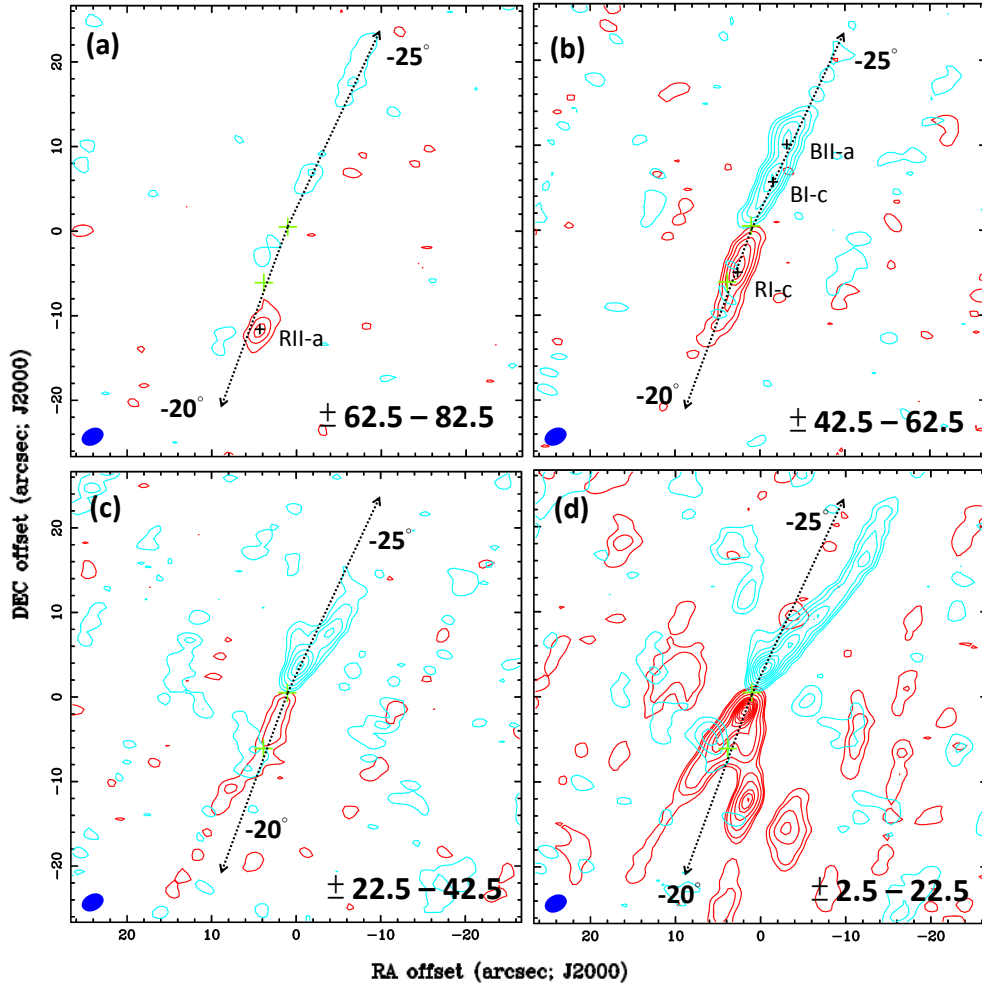
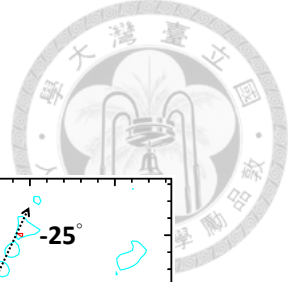


Figure 3.19: moment 0 maps of ^{12}CO (2-1)(contours). The velocity ranges of these four maps are shown in the lower side of each panels. (a) The Contours are drawn every $1.44 \text{ Jy Beam}^{-1} \text{ km s}^{-1}$ (3σ) with the lowest contour level at $1.44 \text{ Jy Beam}^{-1} \text{ km s}^{-1}$ (3σ). (b) and (c) Contours are 3, 6, 10, 15, 20, 25σ with the lowest contour level at $1.44 \text{ Jy Beam}^{-1} \text{ km s}^{-1}$ (3σ). (d) Contours are 3, 6, 12, 20, 30, 35, 40, 45, 50, 55, 60, 65σ in red contours and 3, 6, 10, 15, 20, 25, 30, 35, 40σ in blue contours with the lowest contour level at $1.44 \text{ Jy Beam}^{-1} \text{ km s}^{-1}$ (3σ). Black dashed arrows show the two outflow axes. Green crosses indicate the peak of 1.3 mm continuum and the position of L1448C(S). Black crosses represent the position of knots. The filled ellipse at the bottom left corner in each panels show the synthesized beam.

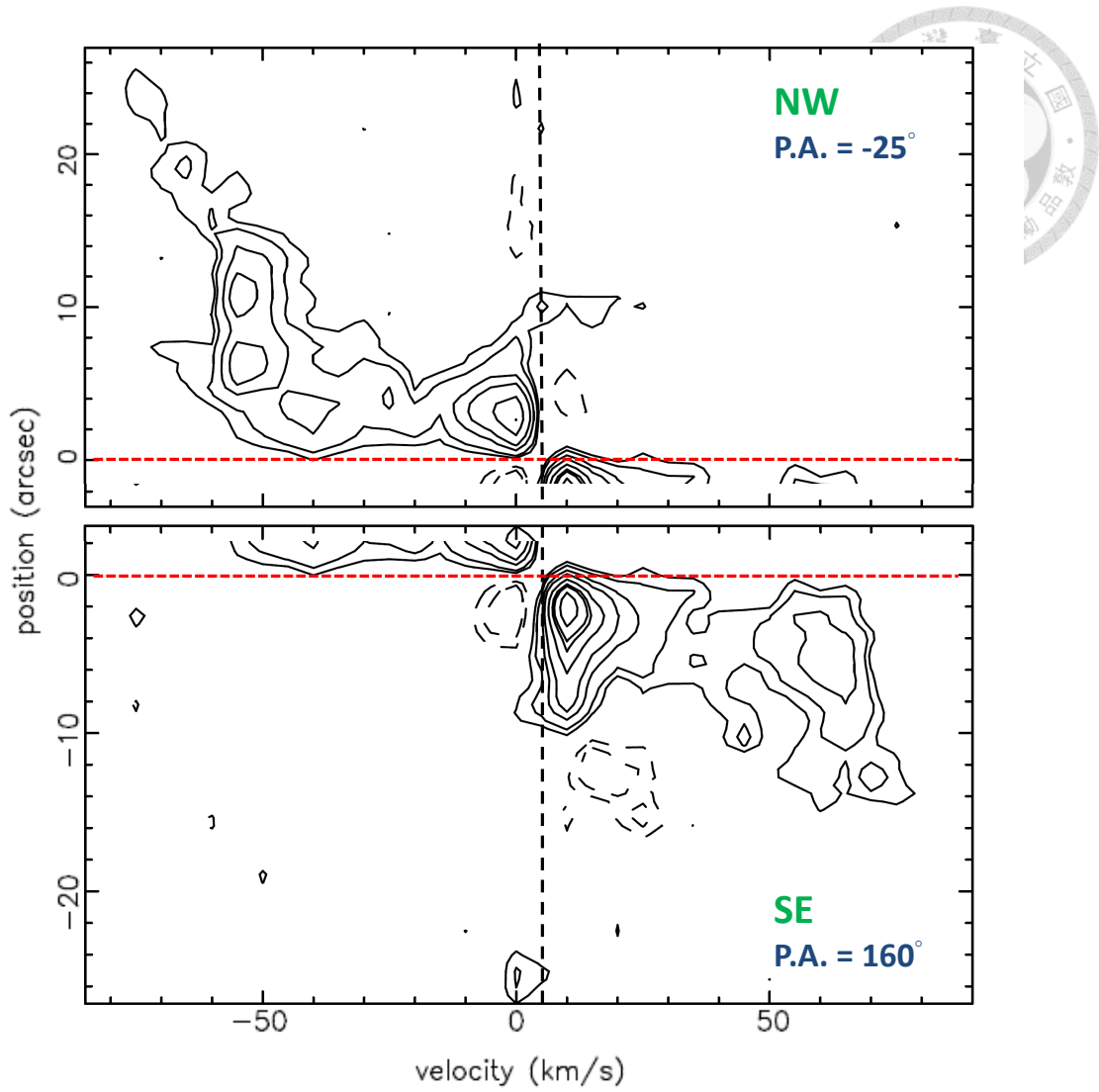


Figure 3.20: P-V diagram of the ^{12}CO (2-1) emission along the jet axes (-25° in the blueshifted part and -20° in the redshifted part). The horizontal red dashed lines are the position of L1448C(N), while the vertical black dashed lines label the systemic velocity $\sim 5 \text{ km s}^{-1}$. Contour levels are from 3σ in step of 3σ , where 1σ is 0.68 K .

Figure 3.21 is the blueshifted and redshifted SiO maps integrated over the velocity ranges shown in Figure 3.17. The SiO reveals jet-like structure similar to the high velocity component in ^{12}CO images. The misalignment of the blue and red lobes is also consistent with the ^{12}CO emission. While the change of the position angle started from about $\pm 8''$ away from the central source is not easy to see because of the SiO emission is faint at BII-a and RII-a. The SiO jet also consists of a chain of knots, which is seen in Figure 3.22. Comparing with the previous higher resolution SMA SiO (8-7) map (Hirano et al. 2010), B1-c and R1-c, B1-b and R1-b and RII-a and BII-a pairs can be identified in Figure 3.22. However, only R1-a can be identified without its counterpart in blueshifted component. It is likely that the BI-a knot is overlapped with B1-b because of the insufficient angular resolution.

This clumpy structure can also be seen in Position-Velocity diagram (Figure 3.23). In the same cuts used in the ^{12}CO , the velocity structure of the jet is similar to the extremely high velocity component (Figure 3.19 (a) and (b)) of the ^{12}CO . From the velocity structure in redshifted part, there is a velocity increase from R1-a to R1-c (the highest velocity $\sim 60 \text{ km s}^{-1}$ in R1). In blueshifted part, there is only an increase of velocity from the stellar position to the BI-c (BI-b and BI-a can not be distinguished). However, there is a difference between red and blue from B1-C to BII-a and from R1-C to RII-a. The velocity slightly decreases in blueshifted part, instead it increases in redshifted part.

Figure 3.24 shows the maps of SO (5_6-4_5) emission integrated over the velocity ranges of $\Delta V = \pm 2.5 \text{ km s}^{-1} \sim \pm 62.5 \text{ km s}^{-1}$. As in the case of the SiO and the EHV CO, the SO emission also comes from the narrow jet-like regions. However, the SO emission is barely seen in the highest velocity ranges (Figure 3.25 (a)). Instead, the jet-like SO emission is seen in the lowest velocity ranges shown in Figure 3.25 (d). There is no V-shaped structure in the SO map.

Figure 3.26 presents position-velocity (P-V) diagram of the SO (5_6-4_5) emission along the two outflow axes. There are two pairs with different velocity offsets; one is in the extremely high velocity at $\Delta V \sim \pm 50 \text{ km s}^{-1}$ with a more extended structure in blueshifted part; and the other is in lower velocity at $\Delta V \sim \pm 10 - \pm 20 \text{ km s}^{-1}$. There is a weaker emission at the systemic velocity and is $2''$ north away from the stellar position. In addition, there is a blueshifted emission component at $\sim 9''$ south of the protostar. This blueshifted component is also seen in Figure 3.27 (d), and is likely to be related to the activity of the L1448C(S) outflow.

The low velocity component in SO ($\Delta V = \pm 22.5 \sim \pm 2.5 \text{ km s}^{-1}$) is very different

from the low velocity component in ^{12}CO outflow not only the peak velocity, but also the morphology. The SO emission in Figure 3.26 (c) and (d) show similar structure to its high velocity component((b)) rather than V-shaped shell-like structure like in ^{12}CO . Comparing the PV-diagram of these two molecular lines, we found that the position of the low velocity component in SO is consistent with the Hubble-law like component in ^{12}CO emission. This suggests that the SO emission consists of not only extremely high velocity molecular jet but also a standard high velocity component ($V_{lsr} \sim 20 \text{ km s}^{-1}$).

We estimated the outflow mass using the ^{12}CO (2-1) data and corrected for the primary beam attenuation. The LTE condition has been assumed. We also assumed 30 K (the temperature from SED fitting) as an excitation temperature. The abundance ratio of H_2 to ^{12}CO we adopted are 10^4 . Although ^{12}CO (2-1) is probably optically thick at the velocity range from $V_{lsr} = 3.05 \sim$ to 7.05 km s^{-1} that ^{13}CO has been detected. We did not detect ^{12}CO (2-1) emission in that velocity range. Then, optically thin assumption are also adopted.

The gas masses derived from ^{12}CO is estimated by following equations:

$$M = 36.3 \times \frac{(d_{kpc})^2}{\nu_{GHz}^3} \times \frac{e^{2.78 \frac{J_L(J_L+1)}{T_{ex}}}}{J_L + 1} \int S_\nu \frac{T_{ex} + 0.9267}{e^{\frac{-h\nu}{\kappa T_{ex}}} (1 - e^{-\tau})} dv,$$

The other physical parameters such as momentum, outflow force and mechanical luminosity are also estimated following methods same as section 3.1.4 in L1157 part. We also estimated the time scale of the EHV components in the SiO and SO emission. The results are listed in Table 3.5 and 3.6.

Table 3.5: Parameters of the ^{12}CO line emission

| | Mass (M_\odot) | Momentum ($M_\odot \text{ km s}^{-1}$) | Time Scale (yr) | Force ($M_\odot \text{ km s}^{-1} \text{ yr}^{-1}$) | Luminosity (L_\odot) |
|----------|-----------------------|---|--------------------|--|-----------------------------|
| Red | 1.31×10^{-3} | 0.008 | 320 | 2.72×10^{-5} | 0.032 |
| Blue | 8.81×10^{-4} | 0.010 | 610 | 1.58×10^{-5} | 0.028 |
| Red(HV) | 3.66×10^{-4} | 0.018 | 100 | 1.65×10^{-4} | 0.81 |
| Blue(HV) | 6.46×10^{-4} | 0.030 | 180 | 1.60×10^{-4} | 0.79 |



Table 3.6: Time scales of the SiO and SO line emission

| | SiO Time Scale (yr) | SO Time Scale (yr) |
|----------|------------------------|-----------------------|
| Red(HV) | 50 | 50 |
| Blue(HV) | 55 | 100 |

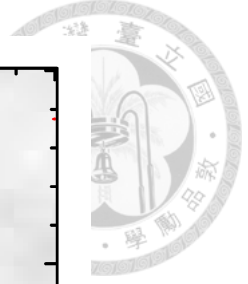
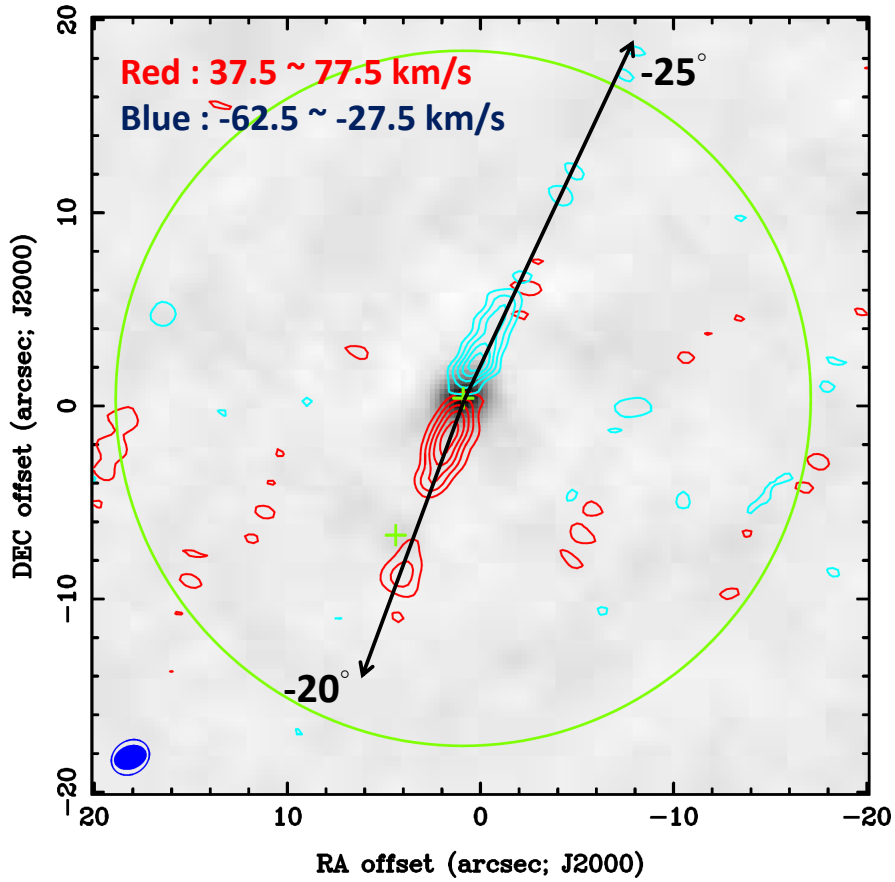


Figure 3.21: Moment 0 map of SiO (8-7)(contours) overlaid on the 1.3 mm continuum grey scale. The blue and red contours indicate the blueshifted component and redshifted component, respectively. The Contours are drawn every 5.31 and $5.1 \text{ Jy Beam}^{-1} \text{ km s}^{-1}$ (3σ) with the lowest contour level at 5.31 and $5.1 \text{ Jy Beam}^{-1} \text{ km s}^{-1}$ (3σ) in red and blue contours, respectively. Green crosses indicate the peak of 1.3 mm continuum and the position of L1448C(S). The filled ellipses at the bottom left corner show the synthesized beams. The green circle is the FOV of 345 GHz. The two dashed arrows are the jet axes.

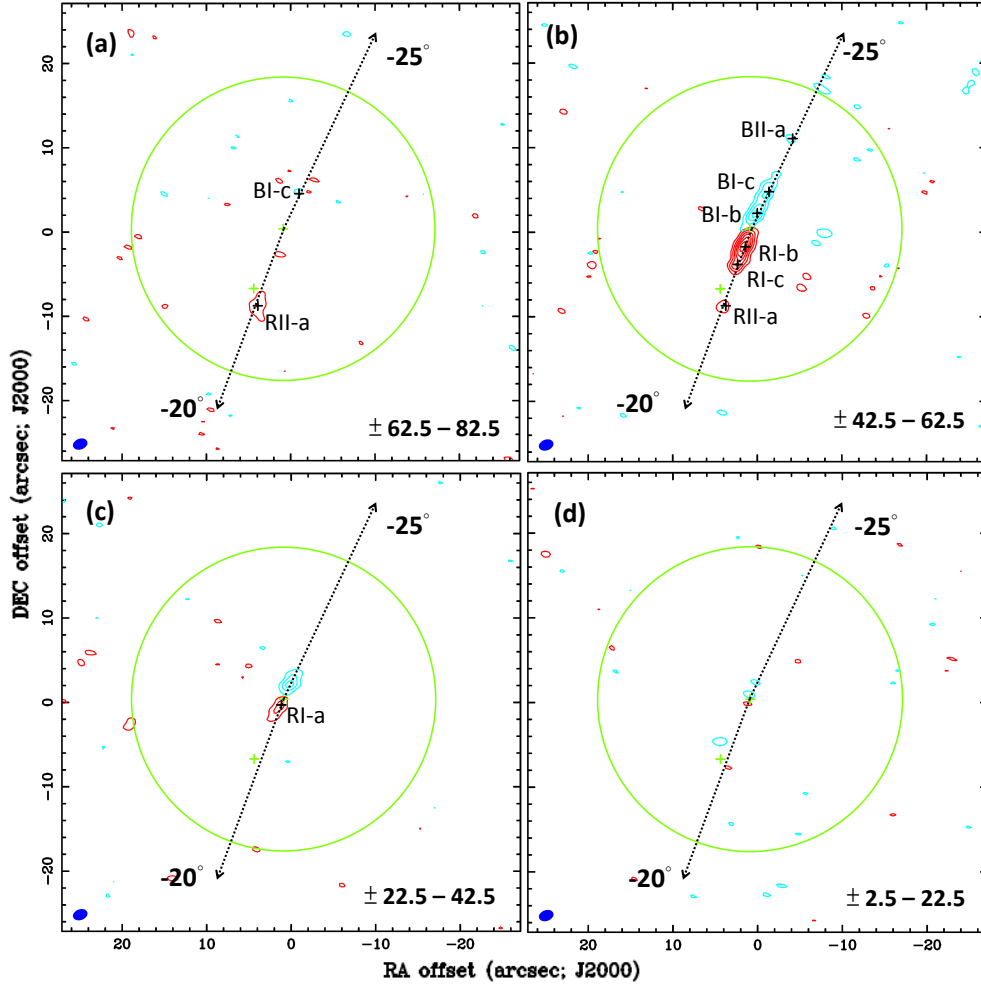


Figure 3.22: Moment 0 maps of SiO (8-7)(contours). The velocity ranges of these four maps are shown in the lower side of each panels. EHV: The Contours are drawn every $3.9 \text{ Jy Beam}^{-1} \text{ km s}^{-1}$ (3σ) with the lowest contour level at $3.9 \text{ Jy Beam}^{-1} \text{ km s}^{-1}$ (3σ). HV: The Contours are drawn every 3.6 and $3.9 \text{ Jy Beam}^{-1} \text{ km s}^{-1}$ (3σ) with the lowest contour level at 3.6 and $3.9 \text{ Jy Beam}^{-1} \text{ km s}^{-1}$ (3σ) in red and blue contours, respectively. MV: The Contours are drawn every 3.9 and $3.6 \text{ Jy Beam}^{-1} \text{ km s}^{-1}$ (3σ) with the lowest contour level at 3.9 and $3.6 \text{ Jy Beam}^{-1} \text{ km s}^{-1}$ (3σ) in red and blue contours, respectively. LV: The Contours are drawn every $3.6 \text{ Jy Beam}^{-1} \text{ km s}^{-1}$ (3σ) with the lowest contour level at $3.6 \text{ Jy Beam}^{-1} \text{ km s}^{-1}$ (3σ). Green crosses indicate the peak of 1.3 mm continuum and the position of L1448C(S). Black crosses represent the position of knots. The filled ellipse at the bottom left corner in each panels show the synthesized beam. The two dashed arrows are the jet axes.

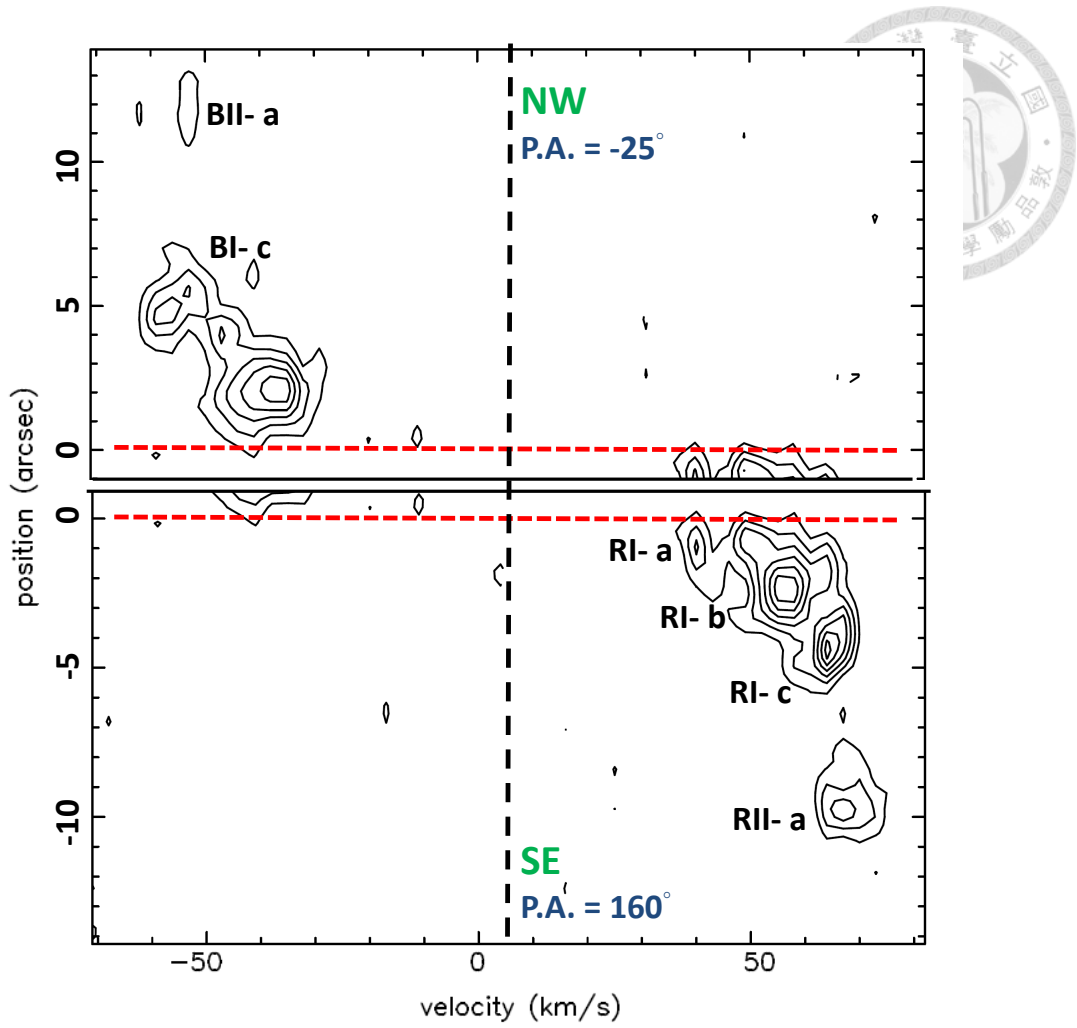


Figure 3.23: P-V diagram of the SiO (8-7) emission along the jet axes (-25° in the blueshifted part and -20° in the redshifted part). The horizontal red dashed lines are the position of L1448C(N), while the vertical black dashed lines label the systemic velocity $\sim 5 \text{ km s}^{-1}$. Contour levels are from 3σ in step of 3σ , where 1σ is 1.95 K.

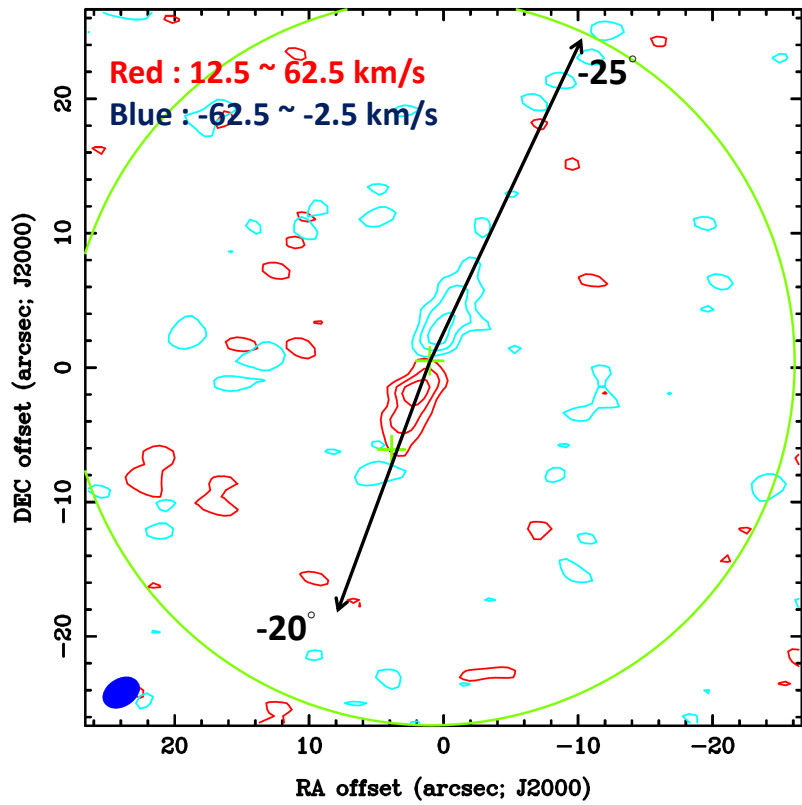


Figure 3.24: moment 0 maps of SO (5_6-4_5)(contours). The velocity ranges of these four maps are shown in the lower side of each panels. The Contours are drawn every $1.11 \text{ Jy Beam}^{-1} \text{ km s}^{-1}$ (3σ) with the lowest contour level at $1.11 \text{ Jy Beam}^{-1} \text{ km s}^{-1}$ (3σ) in four panels. Green crosses indicate the peak of 1.3 mm continuum and the position of L1448C(S). The filled ellipse at the bottom left corner in each panels show the synthesized beam. The arrows are the jet axes.

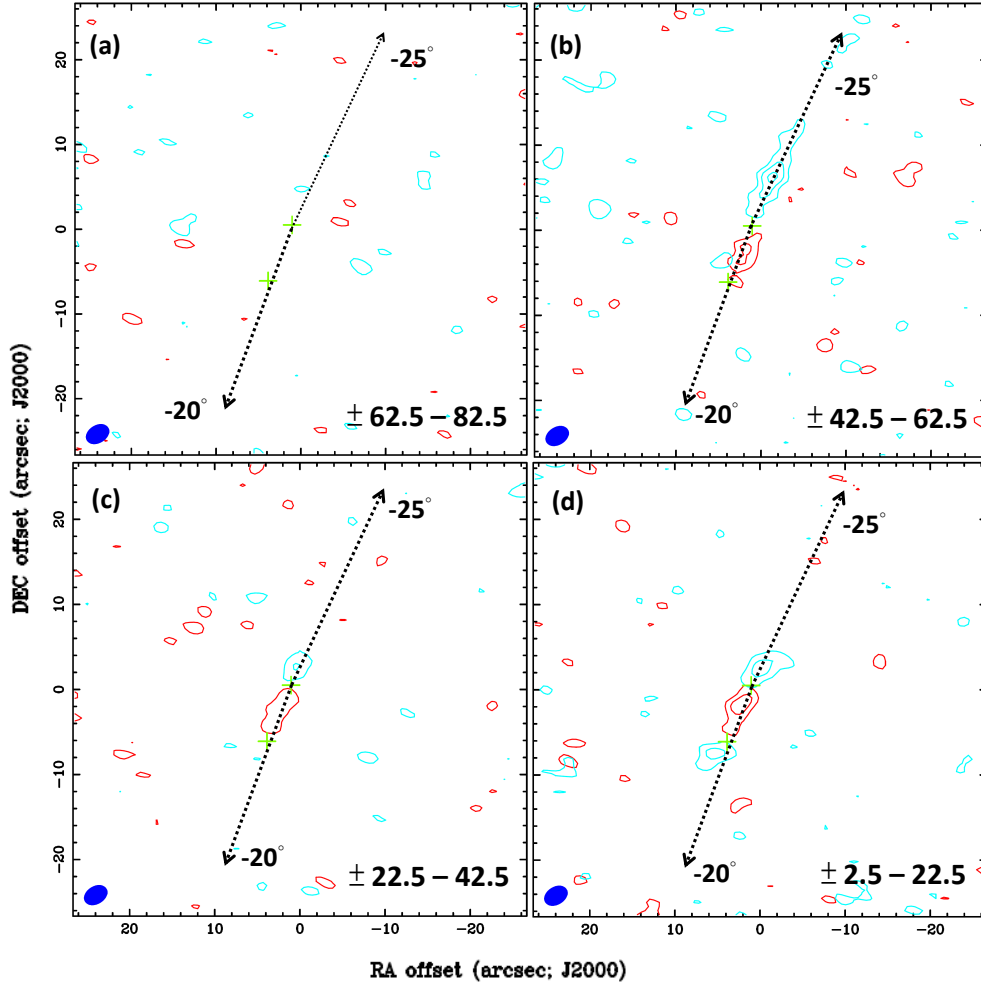


Figure 3.25: moment 0 maps of SO (5_6-4_5)(contours). The velocity ranges of these four maps are shown in the lower side of each panels. The Contours are drawn every $1.11 \text{ Jy Beam}^{-1} \text{ km s}^{-1}$ (3σ) with the lowest contour level at $1.11 \text{ Jy Beam}^{-1} \text{ km s}^{-1}$ (3σ) in four panels. Green crosses indicate the peak of 1.3 mm continuum and the position of L1448C(S). The filled ellipse at the bottom left corner in each panels show the synthesized beam. The arrows are the jet axes.

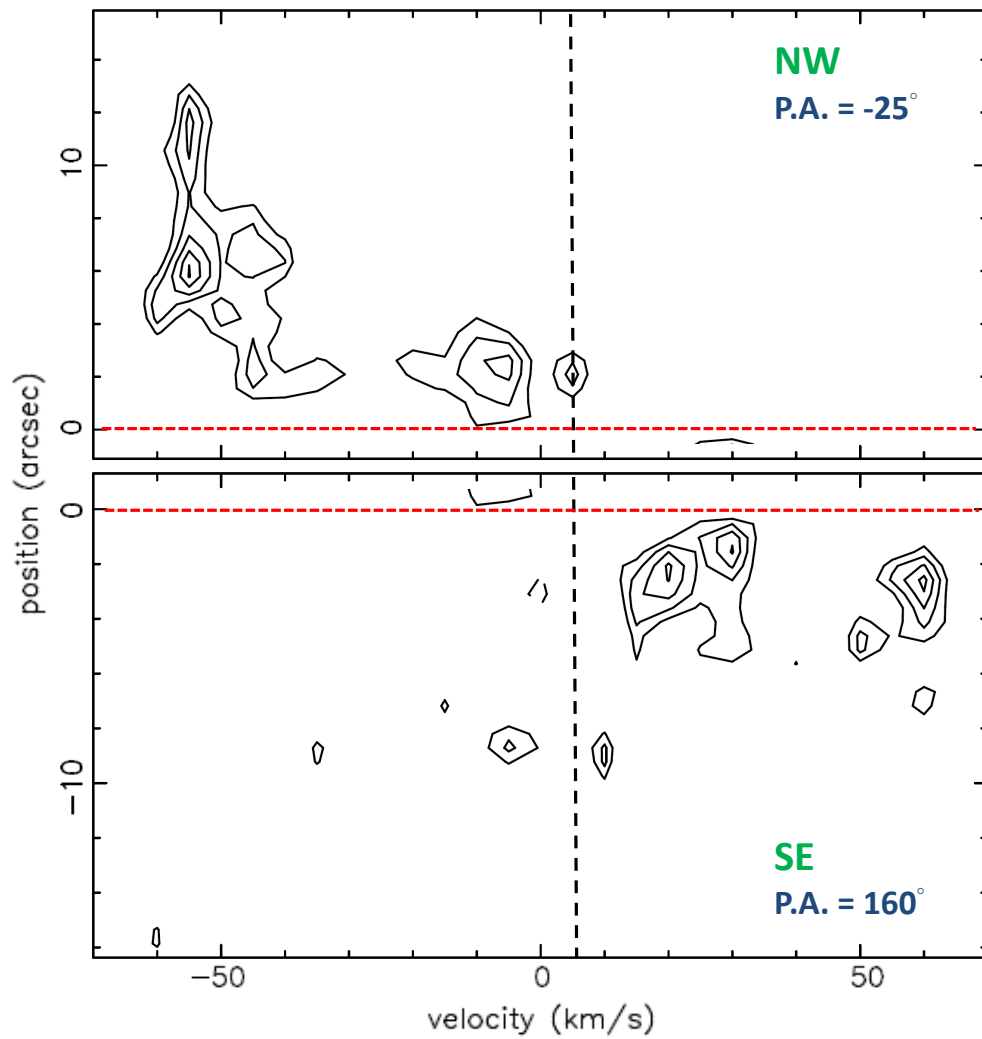


Figure 3.26: P-V diagram of the SO (5_6-4_5) emission along the jet axes (-25° in the blueshifted part and 160° in the redshifted part). The horizontal red dashed lines are the position of L1448C(N), while the vertical black dashed lines label the systemic velocity $\sim 5 \text{ km s}^{-1}$. Contour levels are from 3σ in step of 3σ , where 1σ is 0.48 K .

3.2.3 Envelope: ^{13}CO (2-1), C^{18}O (2-1), CH_3OH ($7_{-1}-6_{-1}$), CS (7-6), H_2CO ($5_{1,5} - 4_{1,4}$)

The C^{18}O (2-1) emission is detected in the velocity ranges from $V_{LSR} = 4.35$ to 4.95 km s^{-1} and from $V_{LSR} = 5.25$ to 6.15 km s^{-1} . Figure 3.27 (a) presents the moment 0 map integrated in these two velocity ranges overlaid on the 1.3 mm continuum emission. The C^{18}O emission peak coincides with the continuum peak position. It reveals a compact component around the protostellar position, suggesting that the C^{18}O emission traces the gas of circumstellar envelope in L1448C(N). Figure 3.27 (b) presents C^{18}O emission overlaid on the ^{12}CO contours in the same velocity range as Figure 3.19 (d). The C^{18}O envelope elongates along the northwest-southeast direction, and which is same as the direction of the ^{12}CO outflow. The elongation of the envelope along the outflow axis is same as the C^{18}O case of L1157, and is often seen in other class 0 source (Arce et al. 2006), suggesting that there is an interaction between outflow and the envelope.

Figure 3.28 (a) is the moment 1 map of C^{18}O (2-1) emission, which shows velocity gradient along the northeast - southwest direction. The direction of this velocity gradient is perpendicular to the outflow axis. The position-velocity diagram along the minor axis (P.A. = 67.5° , Figure 3.28 (b)) clearly shows that blueshifted peak to the northeast and the redshifted peak to the southwest of the protostar. This velocity gradient is nearly symmetric with respect to the central stellar position ($\Delta R \simeq \pm 1''$, $\simeq 440$ AU). The velocity gradient along the minor axis was measured to be $2.05 \times 10^{-3} \text{ km s}^{-1} \text{ AU}^{-1}$. If this velocity gradient is due to the envelope rotation, the specific angular momentum can be estimated as follows:

$$j = R_{rot} \times V_{rot}$$

, j is the local specific angular momentum; R_{rot} is the radius at which rotation was measured; V_{rot} is the rotational velocity at R_{rot} , by estimating the $V_{rot} \simeq 0.482 \text{ km s}^{-1}$ at a radius of about 220 AU after correction for the inclination of 21° (to the plane of sky, Girart et al. 2001). Then the j is calculated to be $5.14 \times 10^{-4} \text{ km s}^{-1} \text{ pc}$.

The mass of the envelope was estimated using the assumption of local thermodynamic equilibrium:

$$M = 2.22 \times 10^4 \times \frac{(d_{kpc})^2}{\nu_{GHz}^3} \times \frac{e^{2.6356 \frac{J_L(J_L+1)}{T_{ex}}}}{J_L + 1} \int S_\nu \frac{T_{ex} + 0.8785}{e^{\frac{-h\nu}{kT_{ex}}}} \frac{\tau}{1 - e^{-\tau}} dv,$$

where τ is the optical depth of $C^{18}O$ and we assume optically thin ($\tau \ll 1$), $[\frac{C^{18}O}{H_2}] \cong 1.7 \times 10^{-7}$ (Frerking et al. 1982), and $T_{ex} = T_{dust} = 30$ K. The $C^{18}O$ total integrated intensity of $78.2 \text{ Jy Beam}^{-1} \text{ km s}^{-1}$ (after the primary beam correction) gives us a gas mass of $9.2 \times 10^{-3} M_{\odot}$.

The ^{13}CO (2-1) emission is detected in the velocity ranges from $V_{LSR} = 3.75$ to 4.35 km s^{-1} and from $V_{LSR} = 5.25$ to 7.05 km s^{-1} . Figure 3.30 (a) presents moment 0 map of ^{13}CO , which is separated in three velocity ranges: blue contour is blueshifted ($\Delta V = -1.25 \sim -0.65 \text{ km s}^{-1}$); both red and green contours are redshifted (Green: $\Delta V = +0.25 \sim +1.15 \text{ km s}^{-1}$; Red: $\Delta V = +1.15 \sim +2.05 \text{ km s}^{-1}$). In addition to the emission which is related to L1448C(N), there is also emissions around the L1448C(S) and an stronger redshifted emission ($\Delta V = +0.85 \sim +2.05 \text{ km s}^{-1}$) southwest ($\sim 7''$, $\sim 1500 \text{ AU}$) toward the L1448C(S).

The velocity range of the green contours was chosen to be the same range as the redshifted $C^{18}O$ component shown in Figure 3.29 ($V_{lsr} = 5.25 \sim 6.15 \text{ km s}^{-1}$). The ^{13}CO emission in this velocity range appears in the west of the central star, which is same as the location of the $C^{18}O$ component in the same velocity range. This suggests that the ^{13}CO in this velocity range arises from the envelope. The ^{13}CO emission components in the velocity ranges of red and blue contours are elongated along the outflow direction, suggesting that they come from the outflow. As shown in Figure 3.30 (b), which compares the blue and redshifted ^{13}CO with the grey scale image of ^{12}CO outflow. The ^{13}CO emission around L1448C(N) coincides with the western and eastern edge of the ^{12}CO outflow shell. This implies that the ^{13}CO redshifted and blueshifted emission may delineates the base of the outflow shell.

Figure 3.30 (b) shows that the southernmost redshifted emission coincides with the region where the outflow from L1448C(S) intersects the western wall of the L1448C(N) outflow. This implies two outflows from two sources are intersecting.

The CS (7-6) emission is detected in the velocity ranges from $V_{LSR} = 3.75$ to 8.75 km s^{-1} . Figure 3.31 (a) presents the moment 0 map integrated over this velocity range overlaid with the 1.3 mm continuum emission in grey scale. As in the case of the $C^{18}O$ emission, the CS emission is centered at the continuum peak position and elongated along the northwest-southeast direction (i.e. along the outflow axis). This suggests that the CS emission traces the gas of envelope in L1448C(N) and is probably affected by the outflow. The PV diagram (Figure 3.31 (b)) of CS emission along the outflow axis (between two different axis: -22.5°) passing through the central protostar. Shows a velocity gradient with the blueshifted component to the

northwest and the redshifted component to the southeast of the protostar. Since this velocity gradient is in the same sense as the ^{12}CO outflow, this is likely to be caused by the interaction between outflow and envelope.

The H_2CO ($5_{1,5} - 4_{1,4}$) emission is detected in the velocity ranges from $V_{LSR} = 3.75$ to 7.75 km s^{-1} . Figure 3.32 (a) presents the moment 0 map separated in blueshifted and redshifted parts overlaid with the 1.3 mm continuum emission. As shown in Figure 3.32 (a), the H_2CO emission shows similar morphology and velocity gradient to the CS; it peaks at the continuum position with an elongation along the outflow axis, and exhibits the velocity gradient with the same sense as the outflow. The PV diagram along the outflow axis presented in Figure 3.32 (b) clearly shows the velocity gradient along the outflow axis. In the case of the H_2CO emission the blue component is stronger than red component, on the contrary, the blue component is much weaker than red component in CS emission.

The CH_3OH ($7_{-1}-6_{-1}$) emission is also detected, at the level of 3σ (Figure 3.33), The CH_3OH component is marginally resolved around the protostellar position of L1448C(N). There is no sign of emission related to L1448C(S).

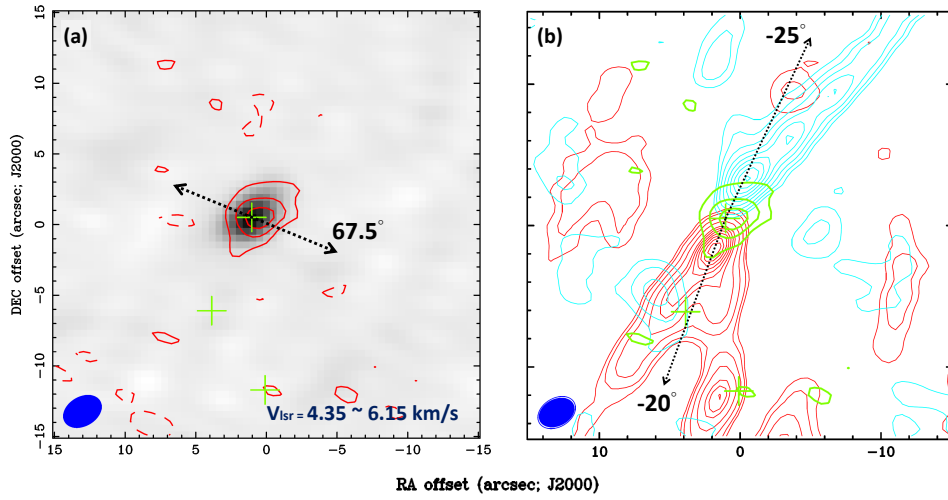


Figure 3.27: (a) moment 0 map of $C^{18}O$ (2-1)(contours) overlaid on the 1.3 mm continuum grey scale. The velocity range is shown in the upper left. The contours are drawn every $0.396 \text{ Jy Beam}^{-1} \text{ km s}^{-1}$ (3σ) with the lowest contour level at $0.396 \text{ Jy Beam}^{-1} \text{ km s}^{-1}$ (3σ). Green crosses indicates the position of L1448C(N), L1448C(S) and the emission seen in ^{13}CO emission. Dashed arrow represents the direction of minor axis. The filled ellipse at the bottom left corner in each panels show the synthesized beam. (b) moment 0 map of $C^{18}O$ (2-1)(contours) overlaid with ^{12}CO contour of Figure 3.21 (d). Dashed arrows represent two outflow axes.

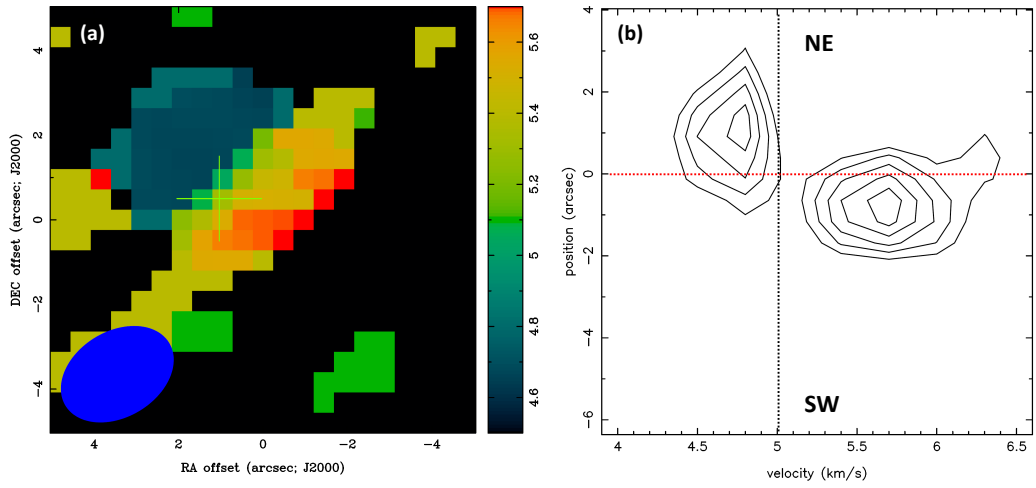


Figure 3.28: (a) The moment 1 map of the $C^{18}O$ (2-1) emission. The color scales ranged from $V_{lsr} = 4.5$ to $5.7\ km\ s^{-1}$. (b) P-V diagram of the $C^{18}O$ (2-1) emission along the outflow axis (-22.5°). Black dotted line shows the systemic velocity, and red dotted line is the protostellar position.

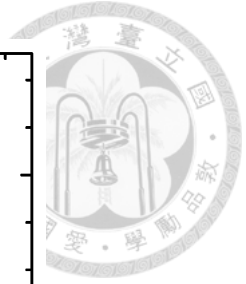
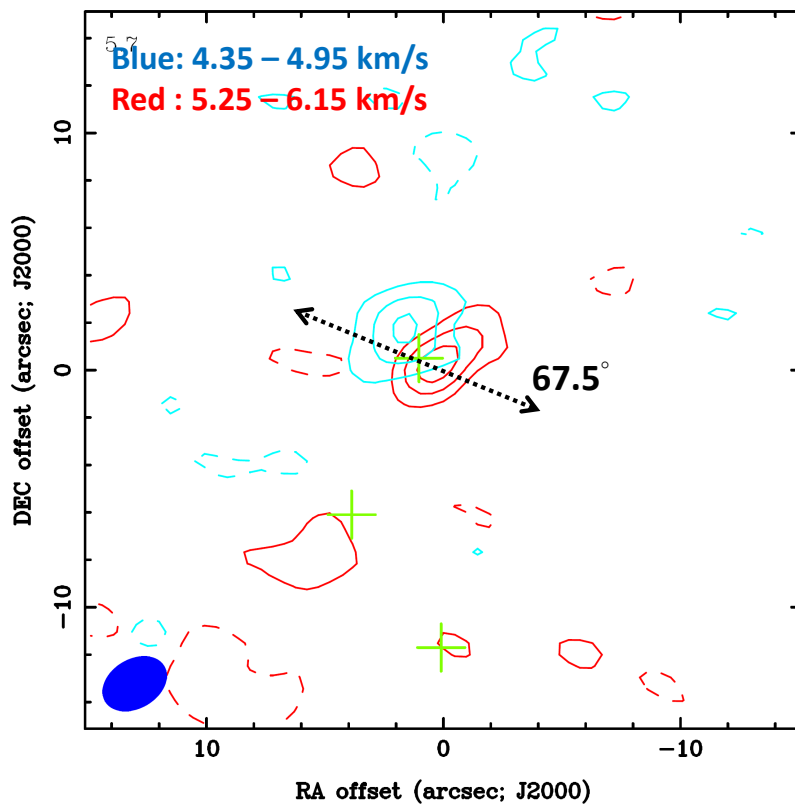


Figure 3.29: Moment 0 map of C^{18}O (2-1) contours. The blue and red contours indicate the blueshifted component and redshifted component, respectively. The velocity range (in V_{lsr}) is shown in the upper left. The contours are drawn every 0.093 and 0.076 $\text{Jy Beam}^{-1} \text{ km s}^{-1}$ (3σ) contours with the lowest contour level at -0.093 and -0.076 $\text{Jy Beam}^{-1} \text{ km s}^{-1}$ (-3σ) for red and blue, respectively. Green crosses indicates the position of L1448C(N), L1448C(S) and the emission seen in ^{13}CO emission. Dashed arrow represents the direction of minor axis. The filled ellipse at the bottom left corner in each panels show the synthesized beam.

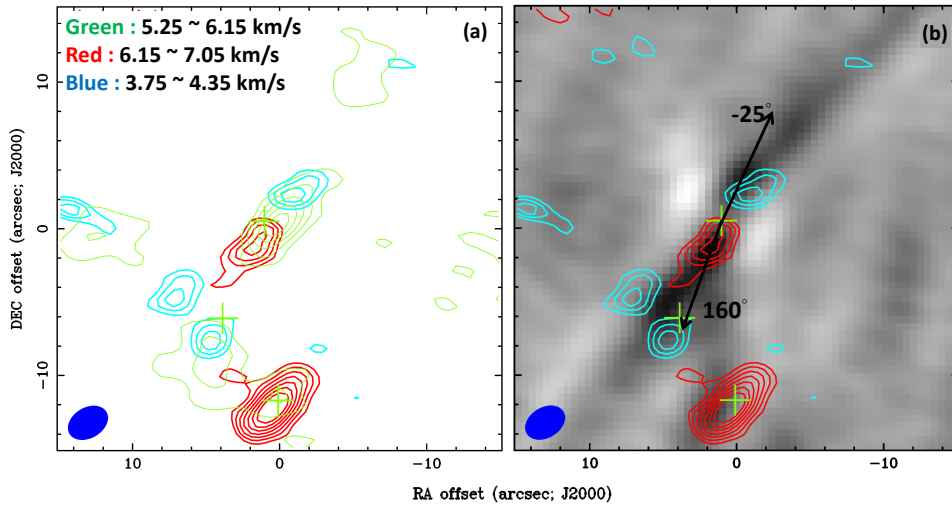


Figure 3.30: Moment 0 maps of ^{13}CO (2-1)(contours) emission. The blue and red contours indicate the blueshifted component and redshifted component, respectively. The green contours in the left panel indicates the component around the systemic velocity ($\sim 5 \text{ km s}^{-1}$). The contours in right panel is overlaid on the ^{12}CO grey scale. The velocity ranges are shown in the upper left of the left panels. The contours are drawn every 0.079 and $0.064 \text{ Jy Beam}^{-1} \text{ km s}^{-1}$ (1σ) with the lowest contour level at 0.237 and $0.192 \text{ Jy Beam}^{-1} \text{ km s}^{-1}$ (3σ) for red and blue contours, and are drawn every $0.237 \text{ Jy Beam}^{-1} \text{ km s}^{-1}$ (3σ) with the lowest contour level at $0.237 \text{ Jy Beam}^{-1} \text{ km s}^{-1}$ (3σ) for the green contours. The upper two green crosses indicate the position of L1448C(N) and L1448C(S). The southernmost green cross indicates the peak of another emission. The filled ellipse at the bottom left corner in each panels show the synthesized beam. The arrows in right panel are the jet axes.

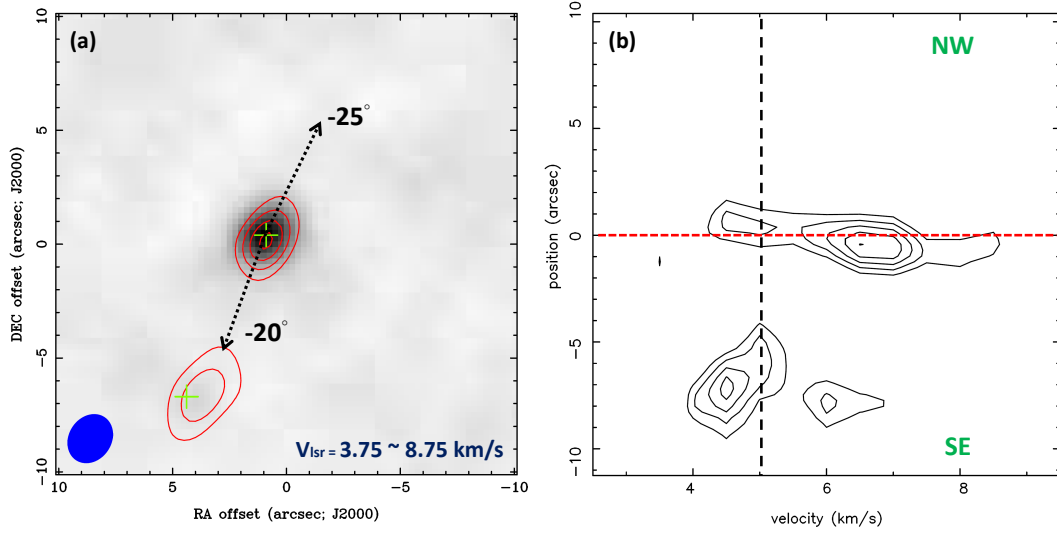


Figure 3.31: (a) moment 0 map of CS (7-6)(contours) overlaid on the 0.85 mm continuum grey scale. The velocity range is shown in the upper left. The contours are drawn every $1.02 \text{ Jy Beam}^{-1} \text{ km s}^{-1}$ (3σ) with the lowest contour level at $1.02 \text{ Jy Beam}^{-1} \text{ km s}^{-1}$ (3σ). Green crosses indicates the position of L1448C(N) and L1448C(S). Dashed arrow represents the direction of outflow axes. The filled ellipse at the bottom left corner in each panels show the synthesized beam. (b) P-V diagram of the CS (7-6) emission along the outflow axis (-22.5°). Black dotted line shows the systemic velocity, and red dotted line is the protostellar position.

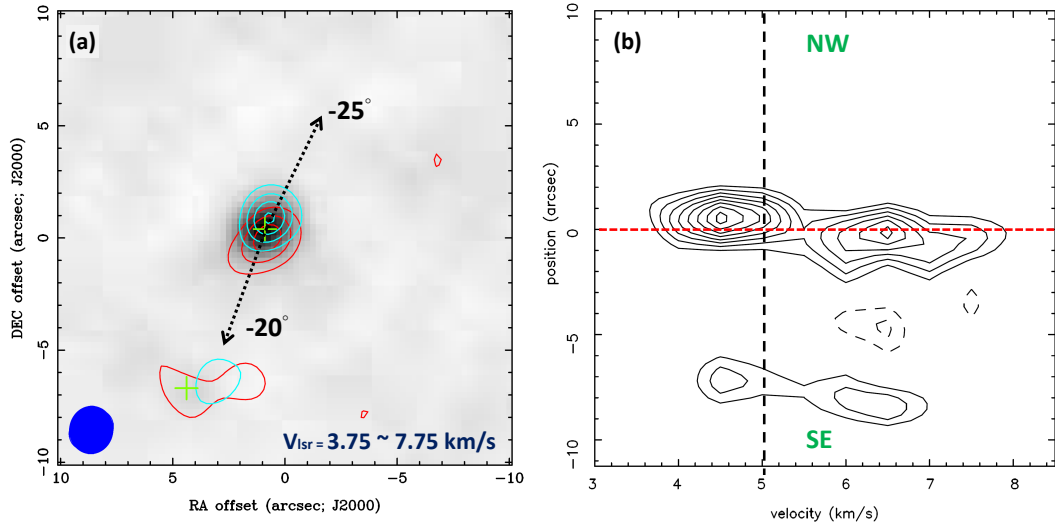


Figure 3.32: (a) Moment 0 map of H₂CO (5_{1,5} - 4_{1,4} contours. The blue and red contours indicate the blueshifted component and redshifted component, respectively. The velocity range (in V_{lsr}) is shown in the upper left. The contours are drawn every 0.546 and 0.471 Jy Beam⁻¹ km s⁻¹ (3σ) contours with the lowest contour level at 0.546 and 0.471 Jy Beam⁻¹ km s⁻¹ (3σ) for red and blue, respectively. Green crosses indicates the position of L1448C(N) and L1448C(S). Dashed arrow represents the direction of outflow axes. The filled ellipse at the bottom left corner in each panels show the synthesized beam. (b) P-V diagram of the H₂CO (5_{1,5} - 4_{1,4} emission along the outflow axis (-22.5°). Black dotted line shows the systemic velocity, and red dotted line is the protostellar position.

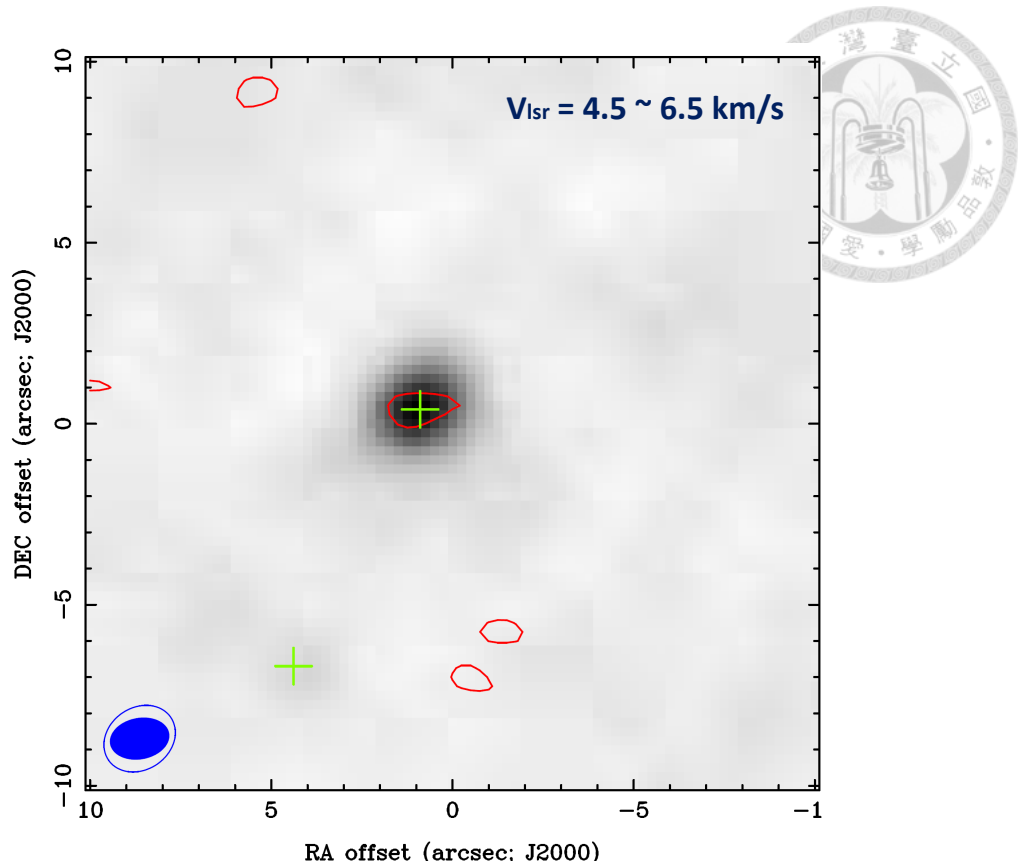


Figure 3.33: The moment 0 map of CH_3OH ($7_{-1}-6_{-1}$) (contours) overlaid on the 0.85 mm continuum grey scale. The velocity range is shown in the upper right. The contours are drawn every $1.29 \text{ Jy Beam}^{-1} \text{ km s}^{-1}$ (3σ) with the lowest contour level at $1.29 \text{ Jy Beam}^{-1} \text{ km s}^{-1}$ (3σ). Green crosses indicates the position of L1448C(N) and L1448C(S). The filled ellipse at the bottom left corner shows the synthesized beam.



Chapter 4

Discussion

4.1 Outflow

4.1.1 Low Velocity ^{12}CO Outflow Shells in L1157 and L1448C

The ^{12}CO outflows from both L1157 and L1448C show V-shaped structures in the low velocity ranges ($\Delta V = \pm 7.5 \text{ km s}^{-1}$ in L1157; $\Delta V = \pm 12.5 \text{ km s}^{-1}$ in L1448C). The velocity structure of these V-shaped component is characterized by the extended low velocity component and Hubble-law like patterns in the PV-diagram ($\Delta V \leq \pm 10 \text{ km s}^{-1}$ in L1157, $\Delta V \leq \pm 20 \text{ km s}^{-1}$ in L1448C).

These morphological and kinematic features seem can be reproduced by the wide-angle wind-driven shell model (Shu et al. 2000). The density and velocity structure of the outflow in this model depend on the wind stratification and on the structure of the ambient medium. If a radially-blowing wide-opening angle wind with density profile of $\propto 1/\sin^2\theta$ is propagating into a flattened ambient medium with a density of $\propto \sin^2\theta/r^2$, the shape of the expanding shell becomes parabolic, and the velocity pattern becomes Hubble-law like. We adopted the simplified analytical model by Lee et al. (2000) to see if these morphological and kinematic features in ^{12}CO emission can be produced by this model.

In the cylindrical coordinate system, the structure and velocity of the shell can be written as follows:

$$z = CR^2, v_R = v_0R, v_z = v_0z,$$

where z is the distance along the outflow axis; R is the radial size of the outflow perpendicular to z ; C and v_0 are free parameters which can define the spatial and velocity structure of the shell. In L1157, the model curves with $C = 0.4 \text{ arcsec}^{-1}$, v_0

$= 0.9 \text{ km s}^{-1} \text{ arcsec}^{-1}$, and the inclination angle of the outflow axis from the plane of the sky, $i = 10^\circ$ successfully reproduce the shape and PV-diagram of the northern red lobe, while the southern blue lobe is reproduced with $C = 0.6 \text{ arcsec}^{-1}$, $v_0 = 1.2 \text{ km s}^{-1} \text{ arcsec}^{-1}$, and $i = 18^\circ$. In the case of L1448C, both the blueshifted and redshifted lobes are reproduced by the model curves with $C = 0.9 \text{ arcsec}^{-1}$, $v_0 = 5.0 \text{ km s}^{-1} \text{ arcsec}^{-1}$, and $i = 21^\circ$. The model curves that delineate the boundaries of the outflow lobe and PV-diagram are shown in Figure 4.1 and 4.2, respectively. The model curves does not trace well the velocity structure around V_{sys} , especially in the blue lobe of L1157, this is probably because significant fraction of the flux is missed in the velocity near the V_{sys} . However, this simple model reproduces the parabolic features in the moment 0 maps and PV-diagram of L1157 and L1448C. Suggesting that the low velocity components in each sources both come from the wind-driven shell.

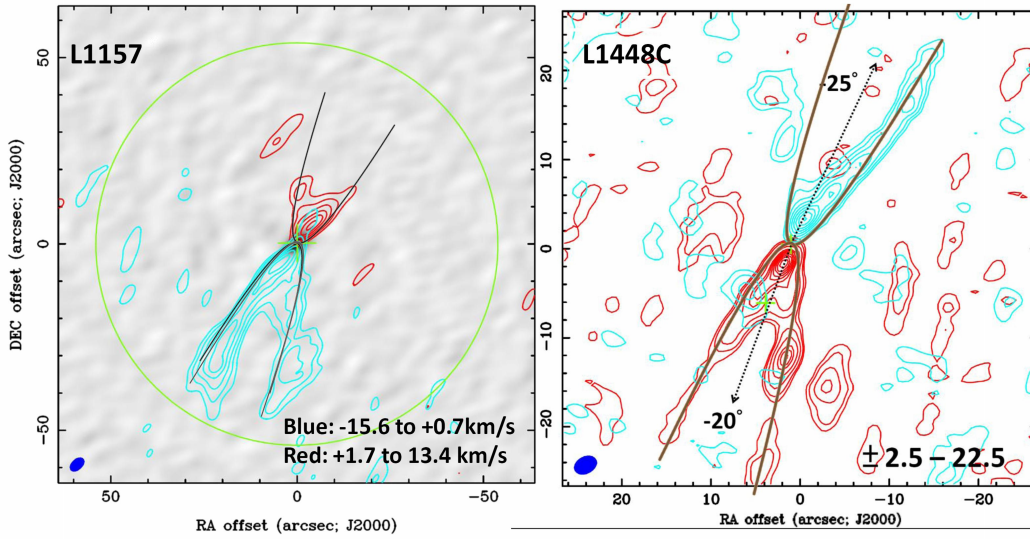


Figure 4.1: moment 0 maps (Figure 3.5 & Figure 3.21(d)) of each sources overlaid with black (L1157) and brown (L1448C) curves. The model parameters are $C = 0.4 \text{ arcsec}^{-1}$, $v_0 = 0.9 \text{ km s}^{-1} \text{ arcsec}^{-1}$, and $i = 10^\circ$ for the red lobe of L1157, $C = 0.6 \text{ arcsec}^{-1}$, $v_0 = 1.2 \text{ km s}^{-1} \text{ arcsec}^{-1}$, and $i = 18^\circ$ for the blue lobe of L1157, and $C = 0.9 \text{ arcsec}^{-1}$ and $v_0 = 5.0 \text{ km s}^{-1} \text{ arcsec}^{-1}$, and $i = 21^\circ$ for the blue and red lobe of L1448C.

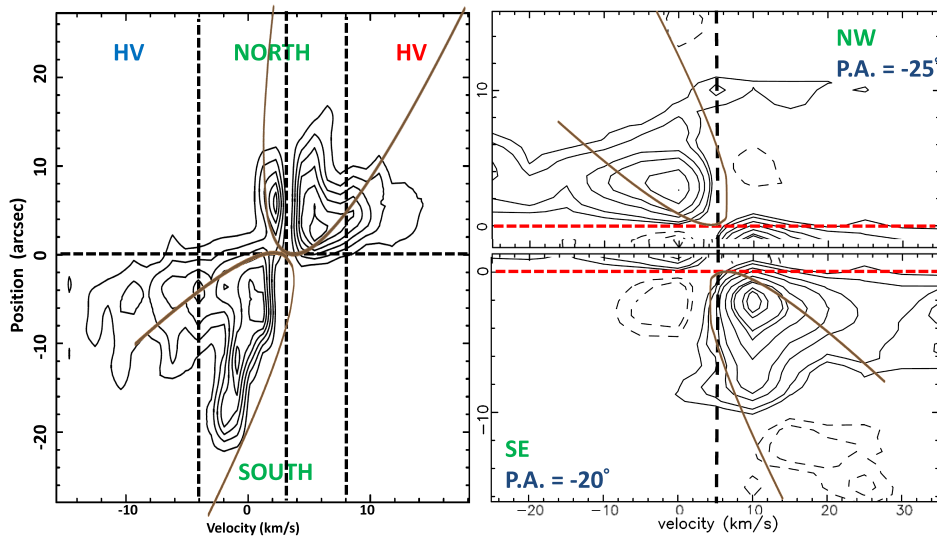


Figure 4.2: PV-diagram of L1157 (left) and L1448C (right) along the outflow axes overlaid with the model. The model parameters are $C = 0.4 \text{ arcsec}^{-1}$, $v_0 = 0.9 \text{ km s}^{-1} \text{ arcsec}^{-1}$, and $i = 10^\circ$ for the red lobe of L1157, $C = 0.6 \text{ arcsec}^{-1}$, $v_0 = 1.2 \text{ km s}^{-1} \text{ arcsec}^{-1}$, and $i = 18^\circ$ for the blue lobe of L1157, and $C = 0.9 \text{ arcsec}^{-1}$ and $v_0 = 5.0 \text{ km s}^{-1} \text{ arcsec}^{-1}$, and $i = 21^\circ$ for the blue and red lobe of L1448C.

4.1.2 High Velocity Components in L1157 and L1448C

In addition to the V-shaped shells in the low velocity ranges, the ^{12}CO emission in both sources also show narrow jet-like features in the high velocity ranges (Figure 3.7 and Figure 3.21 (a), (b)). In the case of the L1157 outflow, the narrow jet-like feature appears in the velocities at $\Delta V \sim \pm 10 \text{ km s}^{-1}$. The position angle of this feature coincides with the line that connects the western wall at the red lobe and the eastern wall of the blue lobe. On the other hand, the jet-like feature in the L1448C outflow is observed along the axes of the lobes with extremely high velocities of $\Delta V \geq \pm 40 \text{ km s}^{-1}$.

In following sections, we discuss the properties of the high velocity component in each source, and propose possible scenario of the outflow structures.

Jet Precession in L1157

The high velocity component of the L1157 outflow has a position angle of $\sim 140^\circ$, while is $\sim 15^\circ$ different from the axis of the V-shaped outflow. If the direction of the high velocity component represents the direction of the recent mass ejection, the outflow should have changed its direction as a function of time. Different position angles between episodic ejection events has already been studied by Gueth et al. 1996 and 1998, Zhang et al. 2000 and Bachiller et al. 2001. They suggested that this change of direction of ejection may caused by the jet precession.

Gueth et al. (1996) modelled the structure of the blue lobe assuming a precession angle of 6° , while Zhang et al. (2000) and Bachiller et al. (2001) modelled the point symmetric structures in the blue and red lobes using a precession angle of 15° .

In order to compare their precession model with our ^{12}CO high velocity component, we apply the simple model assuming that the jet moves in a straight line with constant velocity (100 km s^{-1} for the red part; 65 km s^{-1} for the blue part), and that the ejection direction rotates with constant angular speed with a period of 5000 yr. We modelled the cases with precession angles of 15° and 6° (Gueth). Figure 4.3 shows the model curves overlaid with the map of the high-velocity ^{12}CO component. The purple curve with larger precession angle (15°) coincides with the high velocity component of ^{12}CO emission better than the brown curve with smaller precession angle. This result suggests that the position angle of the high velocity component observed with SMA ^{12}CO is explained by the precessing jet scenario presented by Zhang et al. (2000) and Bachiller et al. (2001).

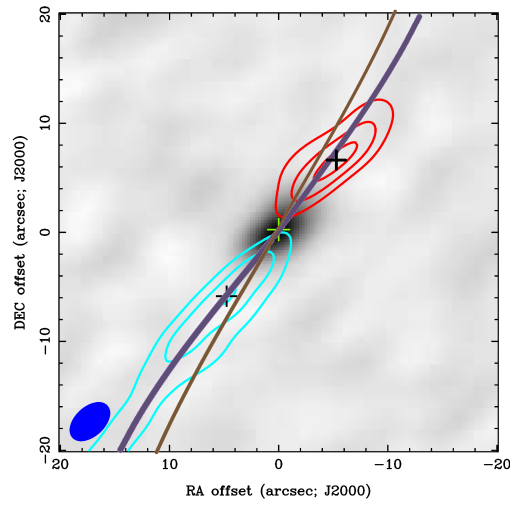


Figure 4.3: The moment 0 map of ^{12}CO emission in L1157 overlaid with jet precessing models. The velocity range is $\Delta V = +5.4 \sim +9.4 \text{ km s}^{-1}$ in red contours and $\Delta V = -6.6 \sim -15.6 \text{ km s}^{-1}$ in blue contours. Purple curve is the model with a precession angle of 15° ; Brown curve is the model with a precession angle of 6° . Green cross and black crosses indicate the position of L1157 and emission peak in red and blue shifted emission, respectively. The filled ellipse at the bottom left corner shows the synthesized beam.

Extremely High Velocity Components along the Jet in L1448C

In the case of L1448C, the jet-like feature is also detected in the SiO ($8-7$) and SO (5_6-4_5). Both SiO and SO are known to become abundant in the shocked regions (e.g. Bachiller & Pérez Gutiérrez 1997). In addition, the SiO and SO lines are exclusively seen in the jet-like feature and not in the V-shaped shells. It is likely that SiO and SO in the EHV jet components represent internal shocks along the jet beam caused by the variation of the velocity of ejection, which is similar to the explanation of the chains of the HH objects (Raga et al. 1990, Raga & Cabrit, 1993, Reipurth & Bally, 2001). The SiO and SO in the protostellar jet are also observed in the HH 211 outflow (Lee et al. 2010).

Difference between High Velocity Components in L1157 and L1448C

The SiO and SO are also detected in the L1157 outflow. However, these lines are not detected along the axis of the outflow but in the regions where the outflow is impinging on the ambient gas. Why the L1157 outflow does not have a narrow jet along its axis like L1448C? This is probably related to the formation mechanism of the jet. The clumpy structure and the velocity feature of the jet seen in the L1448C or HH211 jets suggest that the jet is formed as the fast-moving material plunge into the slow-moving material in the downstream (e.g. Hirano et al. 2010, Figure 4.4 (a)). As a result, the shocks in the jet beam enhance the abundance of SiO and SO. On the other hand, in the case of L1157 (Figure 4.4 (b)), due to the large precession angle, the older ejection event with lower velocity can not be hit by the more recent event with higher velocity. Therefore, successful ejection events do not produce a continuous jet along the axis. The gas ejected in each event directly impinge on the ambient material without interacting without the previously ejected material.

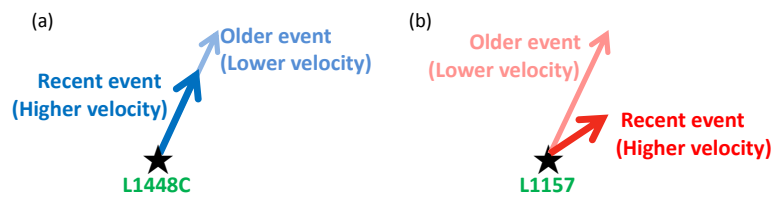


Figure 4.4: Schematic diagram of the different outflow structure in L1448C (a) and L1157 (b).



4.2 Envelope

4.2.1 Kinematics

The $C^{18}O$, CS and H_2CO lines have been detected in both L1157 and L1448C. The spatial distributions of these lines suggest that they are tracing the dense gas envelope surrounding the protostars. However, different lines exhibit different kinetic structures. In the case of L1448C, the velocity gradients seen in the CS and H_2CO lines are parallel to the outflow axis with the same red-blue orientation as the outflow. On the other hand, the velocity gradients of CS and H_2CO in L1157 are opposite to that of the ^{12}CO outflow. In contrast to the CS and H_2CO , the $C^{18}O$ in these two sources show velocity gradient along the axis perpendicular to the outflow. In the following sections, we will discuss the velocity structure parallel and perpendicular to the main outflow axis in L1157 and L1448C.

L1157

Velocity Gradient Parallel to the Outflow Axis: The Opposite Velocity Gradient of CS (7-6) and H_2CO ($5_{1,5} - 4_{1,4}$) emission

The $C^{18}O$ emission from L1157 shows a velocity gradient along the outflow axis (Figure 3.11). The blue-red orientation of this velocity gradient is same as that of the outflow, suggesting that the $C^{18}O$ emission traces the envelope that is affected by the outflow (Figure 3.10 (a) and Figure 3.11). This velocity gradient in the $C^{18}O$ that is same blue-red orientation as the outflow is also observed in several Class 0 sources (Arce et al. 2006).

On the other hand, the CS and H_2CO emission exhibit velocity gradient opposite to the $C^{18}O$ emission: the blue is in the northwest, and the red is in the southeast.

Figure 4.5 (a) shows schematic diagram of one possibility: Such a velocity gradient is explained if the flattened envelope is radially expanding. However, this simple model does not explain the velocity gradient seen in the $C^{18}O$ emission. The observed two different velocity gradient can be explained if the envelope have a pair of cavities the opening angle of which are very large at the base. If the CS and H_2CO emission mainly comes from the dense gas and flattened region at the base, the surface of which is dragged outwards by the outflow, the observed velocity gradient of this region can be opposite to that of the outflow. On the other hand, the $C^{18}O$ emission with lower critical density is likely to arise from more extended region

around the cavities. The gas motion along the cavity walls has the same blue-red orientation in most of the regions except the base of the cavities.

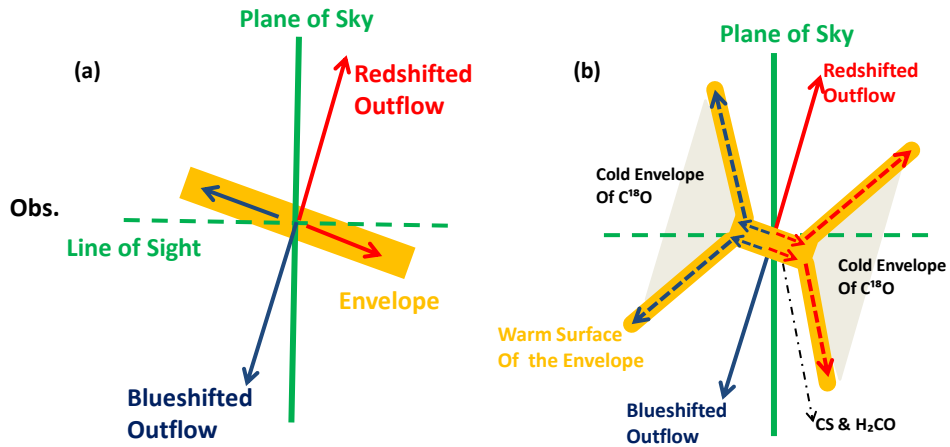


Figure 4.5: Schematic diagrams: (a) A flattened envelope with a radial expanding motion; (b) An envelope with cavities with wide opening angles at the bases.

The Velocity Gradient perpendicular to the outflow axis: Different Envelope Region

The $C^{18}O$ emission from L1157 also shows a small velocity gradient along the minor axis: there is a blueshifted component to the southwest, and the redshifted component to the northeast. Such a velocity gradient along the minor axis was also seen in the $C^{18}O$ (1-0) observed with the IRAM interferometer at Plateau de Bure ($2.4'' \times 2.1''$, Gueth et al. 1997). This velocity gradient is seen in a small region around the central star and is nearly symmetric with respect to the central stellar position ($\Delta R \simeq \pm 2''$, $\simeq 880$ AU). The velocity gradient was measured to be $2.27 \times 10^{-4} \text{ km s}^{-1} \text{ AU}^{-1}$. If this velocity gradient is due to the rotation of the envelope, the specific angular momentum is estimated as follows:

$$j = R_{rot} \times V_{rot},$$

where j is the local specific angular momentum; R_{rot} is the radius at which rotation was measured; V_{rot} is the rotational velocity at R_{rot} . After correction for the inclination of 10° (to the plane of sky), the $V_{rot} \simeq$ was estimated to be 0.102 km s^{-1} at a radius of about 440 AU. Then the j is calculated to be $2.17 \times 10^{-4} \text{ km s}^{-1} \text{ pc}$.

The velocity gradient of the envelope was also studied by Chiang et al. (2010) using the N_2H^+ (1-0) line (Figure 4.6 (a)). The PV-diagram along the minor axis (75° , which is slightly different from ours: 65°) shows that the velocity gradient in large scale is blueshifted at northeast and redshifted at southwest, which is opposite to that seen in our $C^{18}O$ map. However, in the vicinity of the protostellar position ($\leq \pm 10''$), the N_2H^+ (1-0) shows the same velocity gradient as the $C^{18}O$. This indicates that the velocity gradient in the envelope is different in large and small scale. Such an opposite velocity gradient between large and small scale envelope is also seen in IRAS 04365+1535 (Ohashi et al. 1997, and Goodman et al. 1993), IRAS 04368+2557 (Ohashi et al. 1997), and NGC1333 IRAS4a. The possible mechanism to produce such a velocity gradient is magnetic braking.

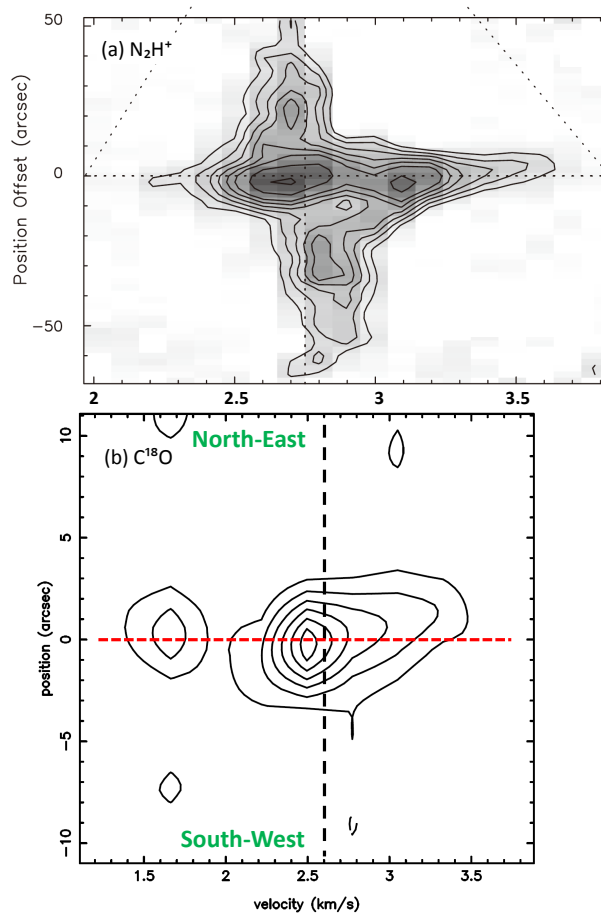


Figure 4.6: (a) PV-diagram of N_2H^+ 1-0 along the axis of 75° (Chiang et al. 2010)
(b) PV-diagram of the C^{18}O 2-1 along the axis of 65° .

L1448C

Velocity Gradient Parallel to the Outflow Axis in L1448C

In the case of $C^{18}O$, CS and H_2CO (Figure 4.7) show the velocity gradient along the outflow axis with the blueshifted component to the northwest, and the redshifted component to the southeast. The blue-red orientation observed in the envelope is same as that of the ^{12}CO outflow. In contrast to L1157, there is no opposite velocity gradient in the CS and H_2CO .

Since the velocity gradient seen in the envelope is same as that of the outflow, it is likely that the envelope gas is dragged by the outflow. In the case of L1448C, the opening angle of cavities one likely to be small even at the base. Therefore, the CS and H_2CO also exhibit the same velocity gradient as the $C^{18}O$.

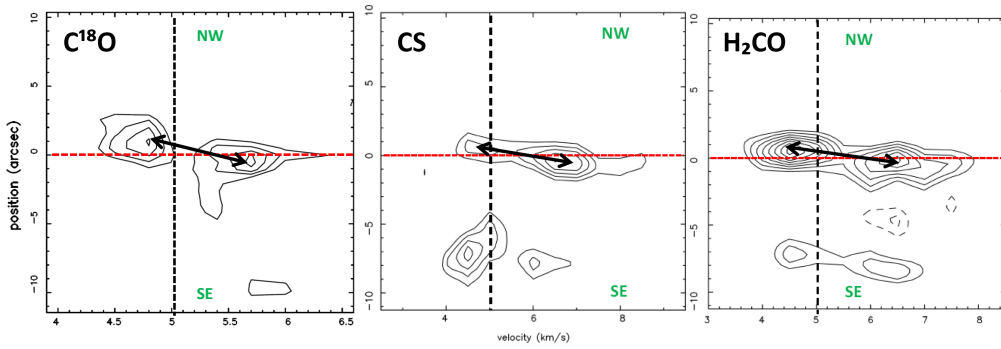


Figure 4.7: P-V diagrams of the $C^{18}O$, CS and H_2CO emission along the outflow axis (-22.5°). The horizontal red dashed lines are the position of L1448C(N), the vertical black dashed lines label the systemic velocity $\sim 5 \text{ km s}^{-1}$. Black arrows show the possible velocity gradient. Contour levels are from 3σ in step of 3σ , where 1σ is 0.27 Jy, 0.33 Jy, and 0.30 Jy for $C^{18}O$, CS and H_2CO , respectively.

Velocity Gradient Perpendicular to the Outflow Axis: Rotation of the circumstellar envelope in C¹⁸O emission in L1448C As shown in Figure 3.28 and 3.29, the C¹⁸O shows a clear velocity gradient along the minor axis: blueshifted at the northeast and redshifted at the southwest. If this velocity gradient is due to the Keplerian rotation, the enclosed mass is calculated using the formula:

$$V_{rot} = \left(\frac{GM_R}{R}\right)^{\frac{1}{2}},$$

where G is the gravitational constant and M_R is the mass contained within the radial distance R. The rotational velocity derived from the PV-diagram of the C¹⁸O is 0.482 km s⁻¹ after the correction of the inclination angle of 21° at a radius of 220 AU. The enclosed mass is estimated to be ~ 0.057 M_⊙. This value is comparable to the mass derived from 1.3 mm continuum emission, 0.062 M_⊙.

4.2.2 Specific Angular Momentum in L1157 and L1448C

The local specific angular momenta of L1448C and L1157 are plotted in Figure 4.8 together with those of YSOs in Taurus. They compare the local specific angular momentum of the Class 0 and Class I objects (filled circles and triangles) with those of the NH₃ dense cores (open squares, Goodman et al. 1993). They suggest the star-forming dense core may consists of two zones: a inner region with relatively constant specific angular momentum; an outer region with power-law relation. The positions of our two sources are similar to other Class I and Class 0 sources in Taurus, falling into the region with relatively constant specific angular momentum. Although the specific angular momentum of L1157 is smaller than that of L1448C (2.17×10^{-4} km s⁻¹ pc and 5.5×10^{-3} km s⁻¹ pc, respectively), there is no significant difference between these two sources.

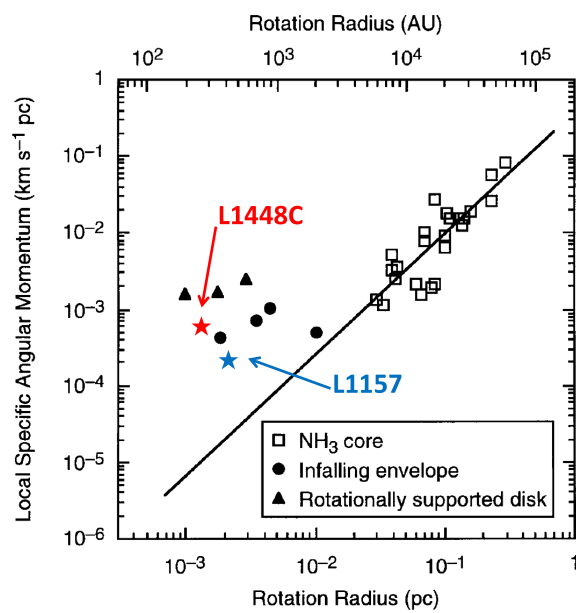


Figure 4.8: Diagram of specific angular momentum versus rotation radius from Ohashi et al. (1997) with blue and red stars representing L1157 and L1448C, respectively.

4.2.3 Origin of Absorption Dips in the C¹⁸O, CS and H₂CO lines in L1448C

As shown in the PV-diagrams of C¹⁸O, CS and H₂CO emission along the outflow axis (Figure 4.9), these three lines show dips in the velocity close to the V_{sys} . The velocity of the dip in each line is indicated by the black dotted line in Figure 4.9. The dip is seen at $V_{lsr} = 5.1 \sim 5.2 \text{ km s}^{-1}$ in the C¹⁸O line, while it appears at $V_{lsr} = 5.5 \sim 5.6 \text{ km s}^{-1}$ in the CS and H₂CO lines. Because the C¹⁸O emission around $V_{lsr} = 5.1 \sim 5.2 \text{ km s}^{-1}$ is totally missing, the dip in the C¹⁸O line likely to be the effect of missing flux (lacking of the short spacing information, thus interferometer resolves out the most extended part of the envelope). However, the different dip velocities of CS and H₂CO lines need an explanation.

The first scenario is an infalling envelope (Figure 4.10 (a)). If the inner dense part of the envelope that is traced by the CS and H₂CO lines is infalling, the infalling gas in front of the protostar has a redshifted velocity with respect to the cloud systemic velocity ($V_{sys} = 5.1 \sim 5.2 \text{ km s}^{-1}$ from the C¹⁸O dip velocity). If the excitation temperature of the outer region is lower than that of the inner region, the lines of moderately optically thickness such as CS and H₂CO produce an absorption dip at the velocity of infalling gas in front of the protostar. The second scenario is the extended dense region with different velocity from V_{sys} (Figure 4.10 (b)) If the dense region is specially extended, the CS and H₂CO flux from the specially extended component (i. e. $V_{lsr} = 5.5 \sim 5.6 \text{ km s}^{-1}$) could not be recovered. The C¹⁸O does not show a dip at this velocity, probably because the C¹⁸O line in the lower frequency (230 GHz) can recover the large scale structure as expanded to the CS and H₂CO in the high frequencies of 345 GHz.

Figure 4.9 shows that the dips in CS and H₂CO lines also appear in the position of L1448C(S). It is unlikely that the envelopes of both L1448C(N) and L1448C(S) are infalling in the same velocity. Therefore, the second scenario of specially extended dense gas with different velocity is more likely in this case.

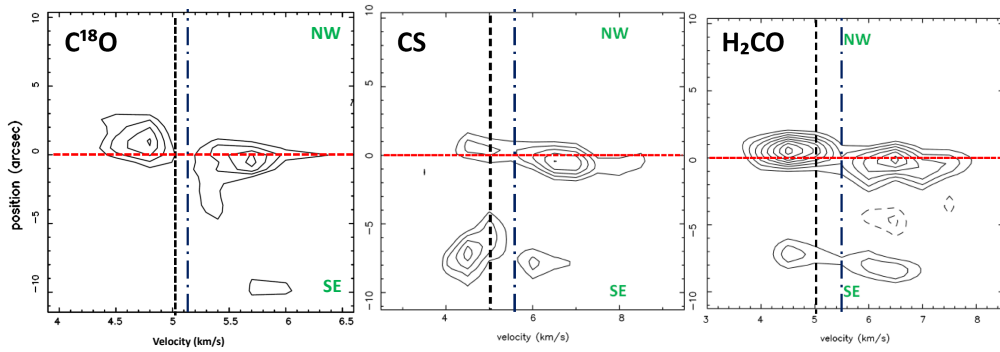
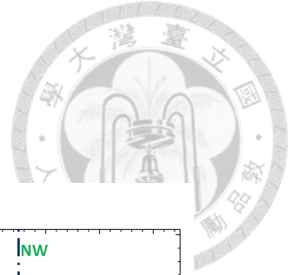


Figure 4.9: P-V diagrams of the $C^{18}O$, CS and H_2CO emission along the outflow axis (same as Figure 4.7) with the blue dot-dashed lines indicate the dip velocities

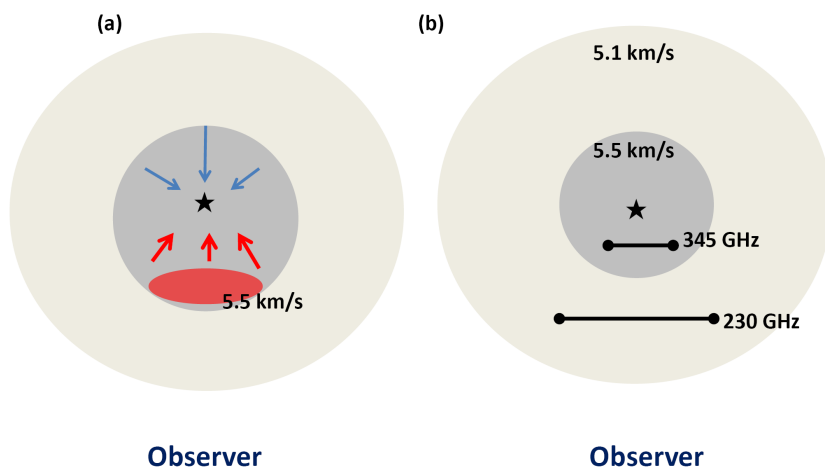


Figure 4.10: Schematic diagrams of two possible envelope structures. (a) an infalling envelope scenario; (b) an extended dense gas scenario.

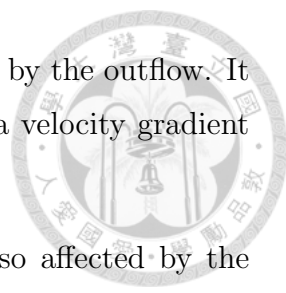


Chapter 5

Summary

We summarize the results and discussions in the following:

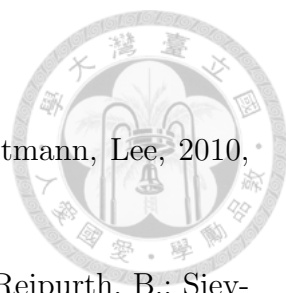
1. In dust continuum, L1157 and L1448C show two components in 345 GHz. One is specially extended, and the other is compact around the central protostar. The sizes of the compact components are $\sim 620 \pm 80$ AU in L1157; $\sim 190 \pm 40$ AU in L1448C. It is likely that these compact components are the circumstellar disks.
2. The ^{12}CO emission of two sources in lower velocity ranges ($\delta V \leq \pm 6$ km s $^{-1}$ in L1157, and $\leq \pm 20$ km s $^{-1}$ in L1448C) show V-shaped conical outflow lobes. The morphologies and kinematics of the low velocity shells are reproduced by the model of wide-opening angle wind.
3. The high velocity component ($\Delta V \sim \pm 10$ km s $^{-1}$) in L1157 shows jet-like feature with a position angle $\sim 140^\circ$, which coincides with the eastern wall of the blue lobe and the western wall of the red lobe. The position angle of this recent ejection event is explained by the precession model with a precession angle of 15° .
4. The EHV component ($\sim \pm 50$ km s $^{-1}$) appears in ^{12}CO , SiO and SO molecular lines along the main outflow axis of L1448C. The appearance of this EHV jet in SiO and SO suggests that there are shocks in the jet beam, representing the internal working surfaces.
5. The L1157 outflow does not show the jet-like component along its axis, this is probably because large precession angle prevent the fast-moving material plunging into the slow-moving material ejected in the past event.

- 
6. The dense gas envelope around L1448C is strongly affected by the outflow. It shows an elongated structure along the outflow axis, and a velocity gradient with the same sense of ^{12}CO outflow.
 7. The dense gas envelope around the L1157 protostar is also affected by the outflow. The C^{18}O shows the same velocity gradient as the outflow, while the CS and H_2CO exhibit the opposite velocity gradient. The kinematic structure of the L1157 envelope is explained if the envelope had cavities with wide opening angles at their bases.
 8. The velocity gradient of C^{18}O lines along the minor axis in L1157 and L1448C show possible rotation of the envelope. The estimated specific angular momenta are $2.17 \times 10^{-4} \text{ km s}^{-1} \text{ pc}$ and $5.5 \times 10^{-3} \text{ km s}^{-1} \text{ pc}$ for L1157 and L1448C, respectively.
 9. The C^{18}O , CS and H_2CO lines observed in the L1448C have dips in their line profiles. The dip velocity in the CS and H_2CO is $\sim 0.4 \text{ km s}^{-1}$ redshifted with respect to the dip in the C^{18}O line. Since the dips in CS and H_2CO are also seen at the positions of both L1448C(N) and L1448C(S), the different dips velocity is unlikely to be attributed to the infall motion. It is more natural to consider that the dense gas in this region has a different velocity from the large scale cloud.



Bibliography

- [1] André, P., Ward-Thompson, D., & Barsony, M. 1993, ApJ, 406, 122
- [2] André, P. & Motte, F., 2000, ESASP, 445, 219A
- [3] Arce, Héctor G.; Sargent, Anneila I., 2006, ApJ, 646, 1070
- [4] Avery, L. W., & Chiao, M., 1996, ApJ, 463, 642
- [5] Bachiller, R., Martin-Pintado, J., Tafalla, M., Cernicharo, J., Lazareff, B., 1990, A&A, 231, 174
- [6] Bachiller, R., Martin-Pintado, J., Fuente, A., 1991, A&A, 243, 21
- [7] Bachiller, R., Martín-Pintado, J., & Fuente, A., 1993, ApJ, 417, L45
- [8] Bachiller, R., Liechti, S., Walmsley, C. M., Colomer, F., 1995, A&A, 295, L51
- [9] Bachiller, R., Guilloteau, S., Dutrey, A., Planesas, P., Martin-Pintado, J., 1995, A&A, 299, 857
- [10] Bachiller, R., Perez, G. M., 1997, ApJ, 487L, 93B
- [11] Bachiller, R.; Pérez Gutiérrez, M.; Kumar, M. S. N.; Tafalla, M., 2001, A&A, 372, 899
- [12] Barsony, Mary; Ward-Thompson, Derek; André, Philippe; O'Linger, Joann, 1998, ApJ, 509, 733
- [13] Beichman, C. A., Neugebauer, G., Habing, H. J. et al. 1988, NASAR, 1190, 1
- [14] Beltrán, M. T., Gueth, F., Guilloteau, S., Dutrey, A., 2004, A&A, 416, 631
- [15] Chandler, Claire J., Brogan, Crystal L., Shirley, Yancy L., 2005, ApJ, 632, 371
- [16] Chen, H., Myers, P. C., 1995, ApJ, 445, 377

- 
- [17] Chen, H., Grenfell, T. G., 1997, ApJ, 478, 295
- [18] Chiang, Hsin-Fang, Looney, Leslie W., Tobin, John J., Hartmann, Lee, 2010, ApJ, 709, 470
- [19] Chini, R.; Ward-Thompson, D.; Kirk, J. M.; Nielbock, M.; Reipurth, B.; Sievers, A., 2001, A&A, 369, 155
- [20] Choi, Minho; Panis, Jean-François; Evans, Neal J., II, 1999, ApJS, 122, 519
- [21] Davis, C. J., & Eisloffel, J., 1995, A&A, 330, 851
- [22] Dutrey, A., Guilloteau, S., Bachiller, R., 1997, A&A, 325, 758
- [23] Frerking, M. A.; Langer, W. D.; Wilson, R. W., 1982, ApJ, 262, 590
- [24] Froebrich, D., Smith, M. D., Hodapp, K.-W., Eisloffel, J., 2003, MNRAS, 346, 163
- [25] Girart, José M.; Acord, Jerry M. P., 2001, ApJ, 552, 63
- [26] Goldsmith, Paul F., Langer, William D., Velusamy, T., 1999, ApJ, 519, 173
- [27] Gueth, F., Guilloteau, S., Bachiller, R., 1996, A&A, 307, 891
- [28] Gueth, F., Guilloteau, S., Dutrey, A., & Bachiller, R., 1997, A&A, 323, 943
- [29] Gueth, F., Guilloteau, S., Bachiller, R., 1998, A&A, 333, 287
- [30] Gueth, F.; Bachiller, R.; Tafalla, M., 2003, A&A, 401, 5
- [31] Guilloteau, S.; Bachiller, R.; Fuente, A.; Lucas, R., 1992, A&A, 265, 49
- [32] Hatchell, J.; Fuller, G. A.; Richer, J. S.; Harries, T. J.; Ladd, E. F., 2007, A&A, 468, 1009
- [33] Hirano, Naomi, Taniguchi, Yoshiaki, 2001, ApJ, 550, 219
- [34] Hirano, Naomi, Ho, Paul P. T., Liu, Sheng-Yuan, Shang, Hsien, Lee, Chin-Fei, Bourke, Tyler L., 2010, ApJ, 717, 58
- [35] Ho, Paul T. P., Moran, James M., Lo, Kwok Yung, 2004, ApJ, 616, 1
- [36] Hodapp, Klaus-Werner, 1994, ApJS, 94, 615

- 
- [37] Jørgensen, J. K., Schöier, F. L., van Dishoeck, E. F., 2002, A&A, 389, 908
- [38] Jørgensen, J. K. et al. 2006, ApJ, 645, 1246
- [39] Jørgensen J. K., Bourke, T. L., Myers, P. C. et al., 2007, ApJ, 659, 479
- [40] Kirk, J. M. et al., 2009, ApJS, 185, 198
- [41] Konigl, A., Pudritz, R. E., 2000, prpl.conf, 759
- [42] Lada, C. J., 1985, ARA&A, 23, 267
- [43] Lada, C.J., 1987, in Star Formation Region, ed. M.Peimbert, J. Jugaku, and P. W. J. L. Brand (Dordrecht: Reidel), IAU Symp., 115, 1
- [44] Lee, Chin-Fei; Mundy, Lee G.; Reipurth, Bo; Ostriker, Eve C.; Stone, James M., 2000, ApJ, 542, 925
- [45] Li, Zhi-Yun, Shu, Frank H., 1996, ApJ, 472, 211
- [46] Masson, Colin R., Chernin, Lawrence M., 1993, ApJ, 414, 230
- [47] Maury, A. J., André, P., Hennebelle, P., Motte, F. et al. 2010, A&A, 512, 40
- [48] Motte, F., André, P. 2001, A&A, 365, 440
- [49] Myers, P. C., et al. 1987, ApJ, 319, 340
- [50] Myers, P. C., Ladd, E. F., 1993, ApJ, 413, 47
- [51] Myers, P. C., Adams, F. C., Chen, H., Schaff, E., 1998, 492, 703
- [52] Neufeld, D. A., Nisini, B., Giannini, T., 2009, ApJ, 706, 170
- [53] Nisini, B.; Codella, C.; Giannini, T.; Santiago Garcia, J.; Richer, J. S.; Bachiller, R.; Tafalla, M., 2007, A&A, 462, 163
- [54] Ohashi, Nagayoshi; Hayashi, Masahiko; Ho, Paul T. P.; Momose, Munetake; Tamura, Motohide; Hirano, Naomi; Sargent, Anneila I., 1997, ApJ, 488, 317
- [55] Ohashi, Nagayoshi; Hayashi, Masahiko; Ho, Paul T. P.; Momose, Munetake, 1997, ApJ, 475, 211
- [56] O'Linger, JoAnn C.; Cole, David M.; Ressler, Michael E.; Wolf-Chase, Grace, 2006, AJ, 131, 2601

- 
- [57] Palau, A.; Ho, P. T. P.; Zhang, Q.; Estalella, R.; Hirano, N.; Shang, H.; Lee, C.-F.; Bourke, T. L.; Beuther, H.; Kuan, Y.-J., 2006, *ApJ*, 636, 137
- [58] Raga, A. C.; Barnes, P. J.; Mateo, M., 1990, *AJ*, 99, 1912
- [59] Raga, A., Cabrit, S., 1993, *A&A*, 278, 267
- [60] Reipurth, Bo; Bally, John, 2001, *ARA&A*, 39, 403
- [61] Reipurth, Bo; Rodríguez, Luis F.; Anglada, Guillem; Bally, John, 2002, *AJ*, 124, 1045
- [62] Rodríguez, L. F, Ho, P. T. P., Moran, J. M., 1980, *ApJ*, 240: L149-52
- [63] Santiago-García, J., Tafalla, M., Johnstone, D., Bachiller, R., 2009, *A&A*, 495, 169
- [64] Schöier, F. L., Jørgensen, J. k., et al. 2004, *A&A*, 418, 185
- [65] Shang, Hsien, Allen, Anthony, Li, Zhi-Yun, Liu, Chun-Fan, Chou, Mei-Yin, Anderson, Jeffrey, 2006, *ApJ*, 649, 845
- [66] Shirley, Yancy L.; Evans, Neal J., II; Rawlings, Jonathan M. C.; Gregersen, Erik M., 2000, *ApJS*, 131, 249
- [67] Shu, Frank H., Adams, Fred C. 1987, *IAUS*, 122, 7s
- [68] Shu, F. H., Ruden, S. P., Lada, C. J., Lizano, S., 1991, *ApJ*, 370, L31
- [69] Shu, F. H., Najita, J. R., Shang, H., Li, Z.-Y., 2000, *prpl.conf*, 789
- [70] Snell, R. L., Loren, R. B., Plambeck, R. L., 1980, *ApJ*, 239: L17-20
- [71] Tafalla, M., & Bachiller, R., 1995, *ApJ*, 443, L37
- [72] Takakuwa, Shigehisa; Kamazaki, Takeshi; Saito, Masao, 2007, *PASJ*, 59, 1
- [73] Takakuwa, Shigehisa; Kamazaki, Takeshi, 2011, *PASJ*, 63, 921
- [74] Terebey, S., Shu, F. H., Cassen, P., 1984, *ApJ*, 286, 529
- [75] Tsujimoto, M.; Kobayashi, N.; Tsuboi, Y., 2005, *AJ*, 130, 2212
- [76] Umemoto, T., Iwata, T., Fukui, Y., Mikami, H., Yamamoto, S., Kameya, O., Hirano, N., 1992, *ApJ*, 392,83

- 
- [77] Umemoto, Tomofumi; Mikami, Hitomi; Yamamoto, Satoshi; Hirano, Naomi, 1999, ApJ, 525, 105
- [78] Velusamy, T., Langer, William D., Goldsmith, Paul F., 2002, ApJ, 565, 43
- [79] Viotti N. R., 1969, MmSAI, 40, 75V
- [80] Wilking B. A., 1989, PASP, 101, 229W
- [81] Young, Chadwick H., Bourke, Tyler L. et al. 2006, AJ, 132, 1998
- [82] Zhang, Q., Ho, P. T. P., Wright, M. C. H., & Wilner, D. J., 1995, ApJ, 451, L71
- [83] Zhang, Q., Ho, P. T. P., & Wright, M. C. H., 2000, AJ, 119, 1345